Internal Report
DESY F35D-96-05
March 1996

Hard Diffractive Scattering in Photoproduction at HERA

by

L. E. Sinclair

Hard Diffractive Scattering in Photoproduction at HERA

Laurel E. Sinclair

Department of Physics
McGill University, Montreal
November, 1995

A thesis submitted to the Faculty of Graduate Studies and Research
in partial fulfilment of the requirements of the degree of
Doctor of Philosophy

Preface

Abstract

Photoproduction events which have two or more jets have been studied in the $W_{\gamma p}$ range 135 GeV < $W_{\gamma p}$ < 280 GeV with the ZEUS detector at HERA. A class of events is observed with little hadronic activity between the jets. The jets are separated by pseudorapidity intervals ($\Delta\eta$) of up to four units and have transverse energies greater than 6 GeV. A gap is defined as the absence between the jets of particles with transverse energy greater than 300 MeV. The fraction of events containing a gap is measured as a function of $\Delta\eta$. It decreases exponentially as expected for processes in which colour is exchanged between the jets, up to a value of $\Delta\eta \sim 3$, then reaches a constant value of about 0.1. The excess above the exponential fall-off can be interpreted as evidence for hard scattering via a strongly interacting colour singlet object.

Résumé

Des événements de photoproduction ayant deux jets ou plus ont été étudiés dans l'intervalle de la variable $W_{\gamma p}$, 135 GeV < $W_{\gamma p}$ < 280 GeV, avec le détecteur ZEUS à HERA. On observe une classe d'événements ayant peu d'activité hadronique entre les jets. Les jets sont séparés par des intervalles jusqu'à quatres unités de pseudorapidité ($\Delta\eta$) et ont des énergies transverses de plus de 6 GeV. Un gap est défini comme une absence de particles ayant des énergies transverses supérieures a 300 MeV entre les jets. La fraction

d'événements possèdant un gap est mesurée en fonction de $\Delta\eta$. Elle décroit de façon exponentielle telle que prévue pour les processus où à lieu l'échange de couleur entre les jets, jusqu'à une valeur de $\Delta\eta \sim 3$, pour ensuite prendre une valeur constante d'environ 0,1. L'excès au-delà de la chute exponentielle peut être interprété comme une indication d'un processus d'échange diffractif dur de singulet de couleur.

Outline

The aim of this dissertation is to describe in detail the analysis of rapidity gaps between jets which led to the preparation of the preprint, DESY 95 191, which has been accepted for publication by Physics Letters B. In fact several passages of the thesis, most notably the abstract and the concluding paragraphs, are taken directly from this preprint. In the first chapter a brief review of the literature on the subject of QCD in general, and on the subject of hard diffractive scattering in particular, is provided. In the next chapter the experimental apparatus, ZEUS and HERA, are briefly described paying particular attention to the main components used in this analysis. In Chapter 3 the procedure followed to isolate a sample of hard photoproduction events is described in detail. Monte Carlo methods will be used in the analysis of the ZEUS data and therefore Chapter 4 provides a description of the generator which was used in the analysis and of the simulation of the ZEUS detector. In Chapter 4 the description by the Monte Carlo events of the global event characteristics of the data is also shown. Interesting results can be obtained from the data simply by comparing the measurements to Monte Carlo generated events which have been subjected to a full simulation of the ZEUS detector resolution and acceptance. These are presented in the first section of Chapter 5. We have also corrected the measured gap-fraction for the effects of the ZEUS detector and made a full determination of the systematic uncertainties affecting the measurement. These results are described in the second section of Chapter 5. Finally, Chapter 6 is devoted

to the interpretation of the results.

Acknowledgements

I am grateful to all of the members of the ZEUS collaboration who have provided advice and constructive criticism during my stay at DESY in particular, Francois Corriveau, Maria Roco, Sampa Bhadra, Katsuo Tokushuku, Chris Youngman, Vivien O'Dell, Rosario Nania, Juan Terron, Claudia Glasman, Klaus Desch, Jim Whitmore, Aharon Levy, Robert Klanner and Malcolm Derrick. I am grateful to my supervisor, Prof. P. M. Patel, for his encouragement, advice and support throughout each of my projects. I am grateful to Jonathan and Susanna Butterworth and to Greg Feild for their friendship and advice. I am grateful to my colleagues and old friends, the Canadians who have shared my life in Hamburg and made it easier, Ken Mclean, Frédéric Bénard, Richard Teuscher, Marc St. Laurent, Cortney Sampson, Miloš Brkič, Rainer Ullman, Ling Wai Hung and Dave Gilkinson. I am also grateful to those at home, Mom, Dad, Heather, Andrew, Dianne, Terry, Jolien, Teviet, Olga, Earl, thank you for being there. I will be back soon. Pat, to you my deepest gratitude. You were right about it being beautiful.

Laurel E. Sinclair
Hamburg, 1995.

Contents

Preface iii

1 Introduction 1
- 1.1 Coupling Strengths . . . 1
- 1.2 Running Couplings . . . 3
- 1.3 Hard Photoproduction . . . 7
- 1.4 Diffractive Scattering . . . 11

2 Experimental Apparatus 20
- 2.1 The HERA accelerator . . . 20
- 2.2 The ZEUS detector . . . 22
  - 2.2.1 The Calorimeter . . . 22
  - 2.2.2 Charged Particle Detection . . . 25
  - 2.2.3 Luminosity Measurement . . . 26
  - 2.2.4 Background Veto . . . 26

3 Data Selection 28
- 3.1 Online Triggers . . . 30
- 3.2 Offline Selection . . . 33

4 Data Simulation and Description 39
- 4.1 The Monte Carlo Event Samples . . . 39
  - 4.1.1 Event Generation . . . 39

1.1.2 Detector Simulation 11
1.2 Monte Carlo Description of Data 13
1.2.1 Selection Criteria 13
1.2.2 Jet Profiles 19
1.2.3 Jet Angle and Energy 51
1.2.4 Island Angle and Energy 56
1.3 Efficiency and Resolution 60

5 Results **66**
5.1 Results from Uncorrected Data 66
5.1.1 Multiplicity 66
5.1.2 Gap-Fraction 68
5.1.3 Summary of Uncorrected Results 73
5.2 Results from Corrected Data 75
5.2.1 Correction Method 75
5.2.2 Systematic Uncertainty 81
5.2.3 Summary of Corrected Results 87

6 Interpretation **91**
6.1 Comparison to Model Predictions 91
6.2 Exponential Fit 97
6.3 Survival Probability 99
6.4 Summary and Conclusions 101

A Kinematics **103**
A.1 Photon beam 104
A.2 Parton momentum fractions 105
A.3 Energy scale 106

B Jet Finding **108**
B.1 The Snowmass Standard 108
B.2 Main Jet Finding Algorithm 109

B.3 TLT Jet Finding Algorithm 111

C Three Jet events **112**

D Bayesian Unfolding **116**
D.1 Procedure 116
D.2 Application 119

E Glossary **124**

List of Tables

5.1 The differential cross section, $d\sigma/d\Delta\eta$. 89
5.2 The cross section for rapidity gap production, $d\sigma^{gap}/d\Delta\eta$. . . . 89
5.3 The gap-fraction, $f(\Delta\eta)$. 90

E.1 Glossary of commonly used expressions 127

List of Figures

1.1 $d\sigma/dQ^2$ for neutral and charged current interactions. 4
1.2 $\alpha_s(Q)$ as measured by ZEUS. 5
1.3 The F_2 structure function as measured by ZEUS. 7
1.4 Diagrams for photoproduction at leading order and at next to leading order. 8
1.5 The ZEUS 1993 measurement of x_γ^{obs}. 11
1.6 A comparison of the diagrams for hard diffractive scattering and diffractive hard scattering. 13
1.7 The plane of the variables Σ_P (sum of momenta of partons in the pomeron) and c_g (relative contribution of hard gluons in the pomeron). 14

1.8 Diagrams showing the difference between colour non-singlet exchange and colour singlet exchange, at HERA. 15
1.9 Signature for hard diffractive scattering at HERA. 16
1.10 Naive expectation for the behaviour of the gap-fraction. 18

2.1 The layout of the HERA accelerator complex. 21
2.2 The ZEUS detector 23

3.1 A dijet photoproduction event in the ZEUS detector. 28
3.2 FCAL and RCAL timing distributions. 32
3.3 t_{FCAL} versus z. 33
3.4 y cuts to suppress p beam-gas and DIS contamination. 35
3.5 Tracking cuts to suppress beam-gas and cosmic contamination. 36
3.6 z of the vertex and the charged current rejection. 37

4.1 Global calorimetric energy sums. 44
4.2 y_{JB}. 46
4.3 Cleaning quantities. 47
4.4 Vertex z position. 48
4.5 Vertex x and y positions. 48
4.6 Jet profile geometry for the trailing jet. 49
4.7 Jet profiles (all $\Delta\eta$). 51
4.8 Jet profiles just for the $\Delta\eta > 3.5$ subsample. 52
4.9 Jet profiles for the gap candidate events with $\Delta\eta > 3.5$. 53
4.10 η^{jet} and E_T^{jet} distributions of the leading and trailing jets. . . . 54
4.11 E_T^{jet} in four bins of $\Delta\eta$. 55
4.12 The distributions of $\bar{\eta}$ and $\Delta\eta$. 56
4.13 $\delta\eta^{island}$ and $\delta\varphi^{island}$ with respect to the jet centres. 57
4.14 E_T^{island} of the maximum E_T^{island} island between the jets. 58
4.15 p_T^{track} of the maximum p_T^{track} track between the jets. 60
4.16 FLT efficiency and the cumulative trigger efficiency. 61

4.17 Cumulative efficiency up to the definition of the reconstructed jets. 62
4.18 Resolutions of the kinematic variables. 63
4.19 The η^{hadron} resolution and the E_T^{hadron} resolution. 64
4.20 The η^{hadron} resolution and the E_T^{hadron} resolution for $\Delta\eta > 3.5$ events. 65

5.1 The island multiplicity distributions in bins of $\Delta\eta$. 67
5.2 The charged multiplicity distributions in bins of $\Delta\eta$. 69
5.3 Uncorrected $\Delta\eta$ distribution for gap candidates, and the gap-fraction. 70
5.4 The $\Delta\eta$ distribution of gap events and gap-fraction made by defining a gap as no tracks with $p_T^{track} > 250$ MeV. 72
5.5 The $\Delta\eta$ distribution of gap events and the corresponding gap-fraction made by defining a gap as ≤ 1 island with $E_T^{island} > 200$ MeV. 72
5.6 The $\Delta\eta$ distribution of gap events and the gap-fraction made by defining a gap as ≤ 1 track with $p_T^{track} > 200$ MeV. 73
5.7 Gap-fractions at the detector and hadron levels. 74
5.8 Correction factors. 76
5.9 Bin efficiencies and purities. 77
5.10 Gap incremental bin-efficiency and bin-purity. 78
5.11 Gap efficiency and purity for a "loose" gap definition. 79
5.12 Gap efficiency and purity for a "tight" gap definition. 80
5.13 Resolution versus $\Delta\eta$. 81
5.14 Inclusive cross section computed in seventeen different ways. . 82
5.15 Gap cross section computed in seventeen different ways. 83
5.16 Gap-fraction computed in seventeen different ways. 84
5.17 Comparison of corrected results from the first and second analyses. 87

5.18 The cross sections, $d\sigma/d\Delta\eta$ and $d/sigma^{gap}/d\Delta\eta$ and the gap-fraction $f(\Delta\eta)$. 88

6.1 Comparison of the cross sections and gap-fraction with the prediction of the PYTHIA non-singlet sample. 92
6.2 The cross sections and the gap-fraction compared with several different model predictions. 93
6.3 Hadron-level jet profiles for the non-singlet model and for the low σ_{p_T} model. 95
6.1 The cross sections and the gap-fraction compared with HERWIG model predictions. 96
6.5 Gap-fraction fit to an exponential form. 97
6.6 Contour plot of the χ^2 function. 98
6.7 x_γ^{OBS}, and the raw $\Delta\eta$ distributions and the gap-fraction in two bins of x_γ^{OBS}. 100

A.1 Diagrams of the hard diffractive scattering process. 103

C.1 Relative azimuth of the two highest E_T^{jet} jets. 113
C.2 $\Delta\eta$ distributions and the gap-fraction using the jets at highest and lowest η^{jet}. 114

D.1 Cause versus effect Example of an unfolding problem. 118
D.2 Cause versus effect according to the mixed Monte Carlo sample. 120
D.3 Unfolding of the mixed Monte Carlo $\Delta\eta$ distributions using the mixed Monte Carlo sample inputs. 121
D.1 Unfolding of the $\Delta\eta$ distributions of a pure resolved Monte Carlo sample using the mixed Monte Carlo sample inputs. . . 122
D.5 Unfolding of the measured $\Delta\eta$ distributions of the data using the mixed Monte Carlo sample inputs. 123

Chapter 1

Introduction

The theoretical motivation for the study of hard diffractive scattering at HERA is presented in this first chapter. An overview of the theoretical framework is developed which concentrates on the issues relevant to hard photoproduction and diffraction.

1.1 Coupling Strengths

The forces which govern all interactions of matter fall naturally into four classes.

The gravitational force, while very much apparent in everyday life, nevertheless is the weakest of the four. For instance, with the combined mass of every particle of the earth acting to pull a needle to the ground, it is still possible for a small magnet to lift the needle. Everything massive or energetic is subject to the gravitational force.

The interactions which come next in strength are called the weak interactions. These are mediated by exchange of the heavy $W^{\pm}$ and Z^0 bosons and are responsible, for instance, for the radioactive decay of neutrons. The constituents of matter, the fermions, can interact via the weak force. In that sense they are said to carry "weak charge". The strength of the weak coupling is here denoted α_W.

A stronger force is the more familiar electromagnetic force. It is responsible, for instance, for the binding of atoms into molecules by exchange of photons between the valence electrons. All particles which carry electric charge can experience the electromagnetic force by exchange of photons, γ. The coupling strength of the electromagnetic force is represented by the dimensionless quantity α. α is proportional to the square of the electric charge of the electron.

The strengths of the electromagnetic and weak interactions can be compared by considering the lifetimes of particles which decay electromagnetically and the lifetimes of particles which have only a weak decay channel. In general, particles which can decay via the strongest interactions will have the shortest lifetimes. For instance the π^0, which decays electromagnetically to two photons, lives on average for only about 10^{-16} s whereas the π^+, which can only decay via the weak interaction, lives much longer, for about 10^{-8} s.

The strongest force (called simply, the strong force) is responsible for the binding of protons and neutrons into the nuclei of atoms. Particles which can decay via the strong interaction have lifetimes of order 10^{-23} s.

Historically a quantum number called colour was postulated to explain the existence of the Δ^{++} particle which is composed of three fermions. The three fermions have identical flavour and spin. However fermi statistics says that no two fermions can occupy exactly the same state. Therefore the three fermions were each assigned a different colour. It is now known that this colour is the charge of the strong force and the theory which describes the strong interactions is called quantum chromodynamics (QCD). Quarks and gluons experience the strong force because they are coloured. However they are confined into colourless states consisting either of a quark anti-quark pair (the mesons) or three quarks (the baryons). Mesons and baryons collectively are known as hadrons. This confinement may be understood in terms of the dependence of the strong interaction coupling constant, $\alpha_s(Q^2)$, on the energy scale of the interaction, Q^2.

This energy scale is related to a distance scale through the uncertainty principle. That is, a large Q^2 process can be considered to proceed via either an exchange of a particle of large virtuality or via exchange of a particle which violates energy conservation by a large amount, ΔE. This particle can only live for a time $\Delta t \leq \hbar/\Delta E$ and propagate at most a distance $\Delta x = c\Delta t$. Thus interactions with a large energy scale occur at short distances. Henceforth, the high energy physics convention of using a system of units in which $\hbar$ and c have the numerical value of unity will be adopted. Factors of $\hbar$ and c are then not written explicitly so mass and momentum have the same dimensions as energy, and time and distance both have the dimensions of inverse energy.

1.2 Running Couplings

The situation is more complicated than outlined thus far. Coupling *constant* is a misnomer as each of the couplings has a distinct dependence on the energy scale of the interaction. For instance $\alpha_W(Q^2)$ rises with Q^2 such that at the energy scales achievable at modern particle accelerators such as HERA, $\alpha_W(Q^2)$ approximately equals $\alpha(Q^2)$ This is nicely illustrated by a recent ZEUS result [1], shown in figure 1.1. Here, the cross sections as a function of energy scale, $d\sigma/dQ^2$, are compared for neutral current (NC) and charged current (CC) interactions. The energy scale, Q^2, in these interactions is equivalent to the invariant mass of the exchanged particle, predominantly the photon for NC interactions and a $W^{\pm}$ boson for the CC interactions. At low energies the neutral current interactions which are primarily electromagnetic lead to far more events than the charged current, or weak interactions. However the weak coupling strength increases with energy with respect to the electromagnetic coupling strength and when the interaction energy reaches the mass of the $W^{\pm}$ bosons, $M_{W^{\pm}} \sim 80$ GeV, the neutral and charged current cross-sections become equal. This equality suggests that the weak interaction actually has a similar coupling strength to the electromagnetic interaction,

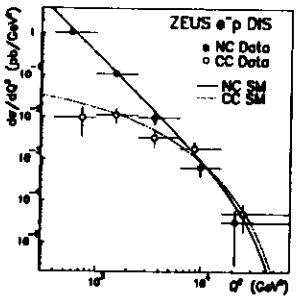

Figure 1.1: ZEUS measurement of $d\sigma/dQ^2$ for neutral current interactions (black dots) and charged current interactions (open circles). The data are plotted at the average Q^2 of the events in each bin. The curves are the standard electroweak model cross sections.

but appears weak because $M^2_{W^{\pm}}$ is large.

The apparent complication of an energy dependent coupling constant actually leads to a great simplification. It is possible to unify the theories of weak and electromagnetic interactions into one theory of electroweak interactions.

The strong interaction coupling constant α_s also depends upon the energy scale. Figure 1.2 shows the recent ZEUS measurement [2] of $\alpha_s(Q)$. $\alpha_s(Q)$ at $Q \sim 20$ GeV is only about 0.15. Thus the strong coupling at high energies is actually weak enough for perturbative methods to be applied in QCD calculations.

The ZEUS measurement is consistent with QCD predictions for the running of $\alpha_s(Q)$ (dashed lines). It is expected that $\alpha_s(Q)$ will continue to fall with Q and that at very high Q values $\alpha_s(Q)$ will be of the order of the electroweak coupling. In fact, grand unified theories exist, in which the strong, electromagnetic and weak interactions are all described with a single coupling.

In the theory of QCD $\alpha_s(Q)$ rises dramatically as $Q \to 0$ or as the distance

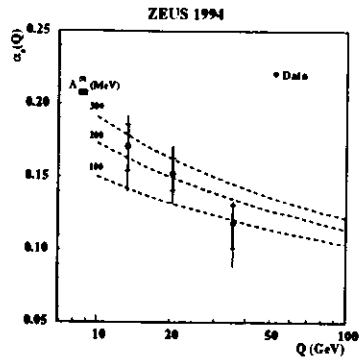

Figure 1.2: ZEUS measured values of $\alpha_s(Q)$ for three different Q^2 regions. The statistical error corresponds to the inner bar and the thin bar shows the statistical and systematic uncertainties added in quadrature. The dashed curves show QCD predictions for the running of $\alpha_s(Q)$.

scale of the interaction increases. (See the dashed curves of Figure 1.2.) This leads to the very strong non-perturbative processes which are presumably responsible for the confinement of the coloured quarks forever in colourless hadrons. If, for instance, one of the constituent quarks of a meson is struck by a high Q^2 probe, it will move away from the other constituent quark with a large relative momentum, for a distance of about 1 fm. At around this distance, however, $\alpha_s(Q) \to 1$. That is, the potential energy stored in the colour field of the two quarks becomes so high that it is favourable to create a quark anti-quark pair out of the vacuum. The escaping quark continues on its way but with less kinetic energy due to the cost of creating the quark anti-quark pair. The process continues until all quarks are associated into mesons or baryons with a small relative momentum. The relative momentum sets the energy scale, Q^2. Therefore $\alpha_s(Q^2)$ is large and the quarks are once

again confined.

Of course, given the large size of $\alpha_s(Q^2)$ at low momentum transfer, confinement processes are not directly calculable in perturbative QCD. However all process which involve a large momentum transfer have a high energy scale Q^2. These are called "hard" processes and they are calculable in perturbative QCD. Thus radiation of hard gluons from the escaping quark of the previous example is calculable. The non-calculable processes which produce the hadrons of the final state come from only "soft", or low Q^2 gluon radiation. This means that the final state hadrons cannot have a large transverse momentum with respect to the parent quark momentum. This property is known as local parton hadron duality [3]. Thus perturbative QCD predictions for final state quark or gluon differential distributions may be tested against measurements of the jets of hadrons they give rise to.

QCD makes other predictions about the distributions of the observable hadrons through the principle of colour coherence [4]. This will be further discussed in subsection 1.1.

The cross section for the interaction $AB \to cdX$ of two hadrons A and B, by the hard scattering of their partonic constituents a and b producing parton jets c and d and two remnant jets X in the final state may be written,

$$\frac{d\sigma^{AB\to cd}}{dQ^2} = C \int dx_A \int dx_B f_{aA}(x_A, Q^2) f_{bB}(x_B, Q^2) \frac{d\hat{\sigma}^{ab\to cd}}{dQ^2}. \qquad (1.1)$$

where the hard subprocess cross section $d\hat{\sigma}^{ab\to cd}/dQ^2$ involves short distance interactions only, is calculable in perturbative QCD, and is independent of the parent hadrons A and B. This reveals an important property of QCD. All of the soft, or long-distance phenomena can be factorized into universal parton distribution functions of the form $f_{aA}(x_A, Q^2)$.

The evolution of the parton distribution functions with Q^2 is predicted by QCD and is known as GLAP evolution [5 7]. For instance, Figure 1.3 shows recent measurements of the proton structure function F_2 by the ZEUS collaboration [8]. Linear fits of F_2 with respect to $\ln Q^2$ are shown as the

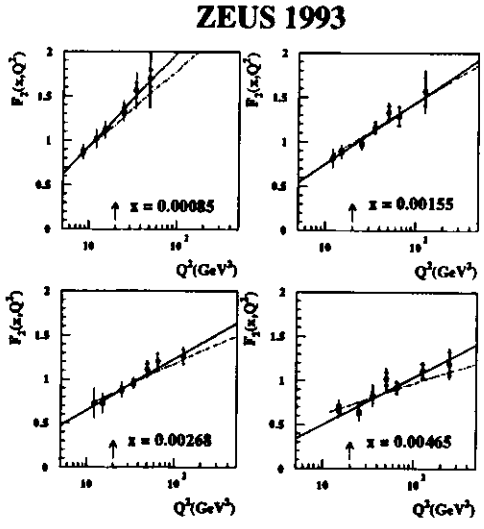

Figure 1.3: The F_2 structure function measurements of ZEUS together with linear fits (solid lines) and the results of a GLAP QCD fit (dashed-dotted lines). The inner error bars show the statistical error and the outer error bars show the systematic uncertainty added in quadrature.

solid lines. The dashed-dotted lines show the results of a GLAP QCD fit using all ZEUS 1993 F_2 data as well as fixed target data at higher x and lower Q^2 from the NMC collaboration [9, 10]. The dashed-dotted lines are in agreement with the data and thus the ZEUS data support the validity of the GLAP evolution.

1.3 Hard Photoproduction

e^+p collisions with a hard scale, Q^2, due to a large invariant mass of the exchanged photon, are called deep inelastic scattering (DIS) events. In general, cross sections $d\sigma/dQ^2$ are highest when the momentum transfer Q^2 is small. This means that most events produced in the e^+p collisions delivered by HERA are mediated by almost real photons, $Q^2 \sim 0$. Thus it is possible to think of HERA, not as an e^+p collider but as a γp collider, where the incoming photon beam has a range of energies from essentially 0, up to the energy of the positron beam, 27.5 GeV. The class of events mediated by almost real photons is referred to as "photoproduction" and for these events it is appropriate to denote the photon invariant mass by P^2 rather than Q^2. This is because it is possible to have a large energy scale in a photoproduction event mediated by exchange of a quark or gluon and Q^2 is reserved to denote this energy scale.

Hard photoproduction events at HERA may be classified into two groups at leading order (LO) [11, 12], shown in Figures 1.4(a) and (c). An example of LO "direct" photoproduction is shown in Figure 1.4(a). Making use of the factorization property of QCD the photon proton collision is broken down into two parts. The hard subprocess consists of the hard collision of the photon with a gluon from the proton. The emission of the photon from the electron, and of the gluon from the proton, with the subsequent production of a proton remnant jet, form the soft part. The hard energy scale, Q^2, of this process comes from the invariant mass of the quark propagator and

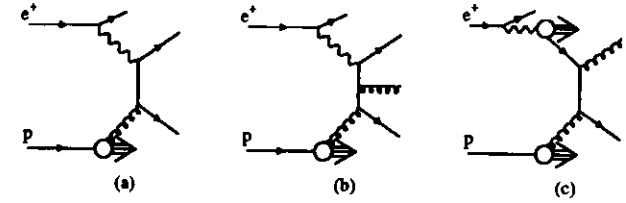

Figure 1.4: Diagrams for photoproduction at HERA. An example of a direct photoproduction process at leading order is shown in (a) while (b) shows a higher order direct photoproduction diagram. An example of a leading order resolved photoproduction process is shown in (c).

is high when the two outgoing quarks have high transverse momentum, p_T, with respect to the incoming photon and proton directions. (Some details of the kinematics of hard photoproduction at HERA are collected in Appendix A.) The magnitude of the hard subprocess cross section is of order $\alpha\alpha_s$ as indicated by the presence of one electromagnetic coupling and one strong coupling in the hard subprocess.

There are two LO direct processes, the one diagrammed in Figure 1.4(a) is called boson gluon fusion. When a quark from the proton scatters with the photon giving rise to a quark jet, a gluon jet and a proton remnant jet in the final state the process is called QCD compton scattering (not shown).

Figure 1.4(b) shows a higher order process in which a gluon is emitted from the quark propagator of Figure 1.4(a). In order for this process to be calculable in perturbative QCD the momentum transfer must be high at each vertex. Then the cross section is of order $\alpha\alpha_s^2$. That is, this process is suppressed by a factor of α_s with respect to the leading order process of Figure 1.4(a).

However, suppose that the momentum transfer at the photon quark vertex of Figure 1.4(b) is small. This process will not be directly calculable in perturbation theory and yet we know that the cross section for such a low Q^2 coupling will be high. The factorization property of QCD holds also for photoproduction events. That is, when the momentum transfer at the photon quark vertex is small the process of Figure 1.4(b) can be calculated according to the illustration in Figure 1.4(c). There is a hard subprocess which consists of the scattering of a quark from the photon with a gluon from the proton and the subprocess cross section is of order α_s^2. The soft photon quark vertex is described by a universal quark distribution function of the photon and there is a photon remnant jet in the final state. Such processes are called LO "resolved" photon events. Note in particular that the presence of both a photon and a proton remnant jet in these events allows for the possibility of a second interaction between the constituents of

the photon and proton [13–17].

As with the proton, the parton distribution functions of the photon may be determined by experiment at some input scale Q_0^2 and then they are specified at all values of Q^2 through the GLAP evolution equations [18–20]. In an alternate approach, the γ structure is decomposed into two components. The large x_γ component is described by the point-like coupling of the γ to a $q\bar{q}$ pair. The low x_γ component is described by the fluctuation of the γ into a vector meson state, with the subsequent hard interaction involving a partonic constituent of this vector meson [21,22]. The parton distributions of the photon are of order α/α_s [23] and therefore LO resolved photon processes are of order $\alpha\alpha_s$. That is, LO resolved and LO direct processes are of the same order. In fact, in the kinematic regime of the present study, LO resolved processes dominate [21,25].

Direct and resolved photoproduction events are distinguished by the momentum fraction of the photon which is carried by its parton into the hard interaction, x_γ. For LO direct events $x_\gamma = 1$ and for LO resolved events $x_\gamma < 1$. However x_γ is an experimentally inaccessible quantity as it is only clearly defined at leading order. An important result of the 1993 ZEUS hard photoproduction analysis was the introduction of the observable x_γ^{OBS} which is clearly defined to all orders of perturbation theory and which therefore may be measured, and compared to theoretical predictions [26,27].

$$x_\gamma^{OBS} = \frac{\sum_{jets} E_T^{jet} e^{-\eta^{jet}}}{2E_\gamma} \tag{1.2}$$

where E_γ is the incident photon energy, E_T^{jet} and η^{jet} are the transverse energy and pseudorapidity respectively of the jets and the sum runs over the two jets of highest energy. Replacing the sum over jets by a sum over the two hard partons reduces x_γ^{OBS} to the leading order x_γ (see Appendix A).

The ZEUS measurement of x_γ^{OBS} using the 1993 dijet sample is shown[1]

[1]The superscript OBS is here replaced by *cal* to signify that the result has not been corrected for detector effects.

in Figure 1.5 by black dots. A clear two component structure consisting of

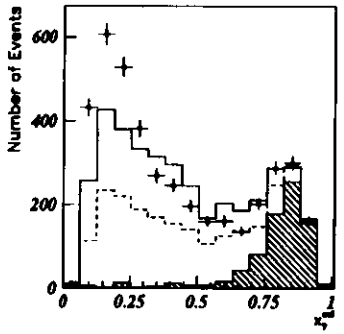

Figure 1.5: The ZEUS 1993 measurement of x_γ^{obs}. The black dots show uncorrected ZEUS data. The solid and dashed lines show the predictions of two different Monte Carlo simulation routines. The LO direct contribution to the distribution shown by the dashed line. is represented by the hashed histogram. The Monte Carlo curves have been normalized to fit the direct peak in the data.

a narrow peak at high x_γ^{OBS} and a wider peak toward low values of x_γ^{OBS} is apparent. Some model predictions are overlaid. In particular the hashed histogram shows the predicted x_γ^{OBS} distribution for LO direct events. The peak at high x_γ^{OBS} is clearly associated with LO direct processes leaving the peak at low x_γ^{OBS} to be explained by LO resolved processes. (The failure of the model predictions to reproduce this peak is understandable given the large uncertainty in the parton distributions of the photon at low x_γ.)

1.4 Diffractive Scattering

The word "diffraction" was introduced to high energy physics to describe a phenomenon which was observed in the cross section for hadron-hadron elastic scattering. It was observed that the cross section differential in the

momentum transfer looks very similar to the pattern produced in the diffractive scattering of light by an opaque object. Today the study of diffractive processes is much more inclusive. An increasingly accepted definition of diffractive processes is the following [28],

> *A process is diffractive if and only if there is a large rapidity gap in the produced-particle phase space which is not exponentially suppressed.*

where a rapidity gap is a rapidity[2] interval which contains no final state particles.

Hard diffraction then refers to those diffractive processes which have high transverse energy jets in the final state phase space. Hard diffraction may be further distinguished [28].

1. *Diffractive hard processes have jets on only one side of the rapidity gap.*
2. *Hard diffractive processes have jets on both sides of the rapidity gap.*

If we define t to be the momentum transfer across the exchanged colour singlet object then in hard diffractive scattering processes $|t|$ corresponds to the energy scale Q^2 of the hard scatter. However in diffractive hard scattering the magnitude of the invariant mass of the exchanged colour singlet particle, $|t|$, is much smaller than the hard scale, Q^2, which comes from the exchanged quark or gluon. These two complementary kinematic regimes are represented in Figure 1.6. (A detailed presentation of the kinematics of hard diffractive scattering may be found in Appendix A.)

Diffractive hard scattering is being extensively studied at HERA by both the ZEUS and H1 collaborations [29–33]. These events can be interpreted as

[2]Rapidity is approximated by pseudorapidity. Pseudorapidity is given by $\eta = -\ln\tan\vartheta/2$ where ϑ represents the polar angle with respect to the proton direction.

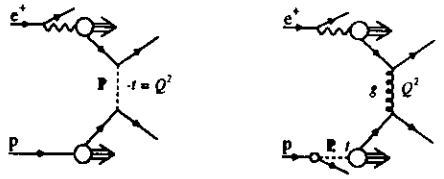

Figure 1.6: In (a) a hard diffractive scattering process is shown which proceeds via exchange of a colour singlet object, labelled $I\!P$, of virtuality $t = -Q^2$. The complementary diffractive hard process is shown in (b). The colour singlet object, $I\!P$, has a small virtuality t, while the hard energy scale Q^2 comes from the virtuality of the exchanged gluon, g.

the scattering of the incoming positron or photon from a colour-singlet object emitted by the proton, which has been called a pomeron. It is possible to measure the parton content of this pomeron, analogously to the measurement of the proton's parton content. The pomeron is drawn in Figure 1.6(b) as a dashed line. A quark from the pomeron is shown participating in the hard interaction leaving behind a pomeron remnant jet. Note that the sum of all of the momentum fractions of the partons in the pomeron, $\Sigma_{I\!P}$, is not constrained to equal unity as it is for the proton.

Figure 1.7 shows the results of a comparison of diffractive hard scattering in photoproduction and in deep inelastic scattering [31]. c_g represents the relative contribution of hard gluons in the pomeron. The two analyses constrain $\Sigma_{I\!P}$ and c_g in different ways and therefore the combined information constrains each of $\Sigma_{I\!P}$ and c_g separately. The data indicate that between 30% and 80% of the momentum of the pomeron carried by partons is due to hard gluons.

To understand the signature for hard diffractive scattering we compare the hadron radiation pattern in a colour non-singlet exchange process shown in Figure 1.8(a), with the hadron radiation pattern in a colour singlet exchange process shown in Figure 1.8(b). In the example of Figure 1.8(a) a red u quark

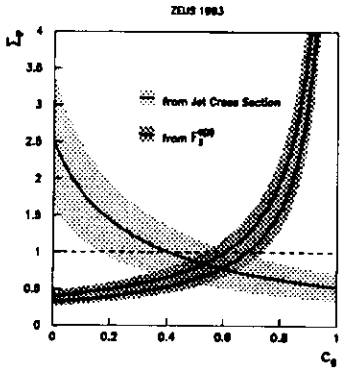

Figure 1.7: The plane of the variables $\Sigma_{I\!P}$ (sum of momenta of partons in the pomeron) and c_g (relative contribution of hard gluons in the pomeron). The solid line is obtained from a χ^2 fit to the inclusive jet cross section of Monte Carlo predictions for the pomeron structure. The dashed dotted lines show the constraint imposed by the measurement of the diffractive structure function in DIS.

from the photon scatters with a green d quark from the proton via exchange of an $\bar{r}g$ (or $r\bar{g}$) gluon. The centre of mass view of just the scattering partons is shown below the full diagram. The highest cross section occurs for a glancing collision, i.e. when the scattering angle, ϑ, is small. However notice that because of the exchange of colour via the di-coloured gluon the colour charge has actually been accelerated through the large angle $\pi - \vartheta$. An accelerated colour charge will radiate gluons tangentially to its direction of travel in the same way that an accelerated electric charge radiates photons. Thus final state particles, the fragmentation products of this soft radiation, are expected throughout most of the central rapidity region.

An example of a hard photoproduction event which is propagated by a colour singlet particle is shown in Figure 1.8(b). The dashed line could represent, for instance, a photon. Again, the cross section is highest for low values of ϑ, but in this case the colour scattering angle is equal to ϑ. Thus

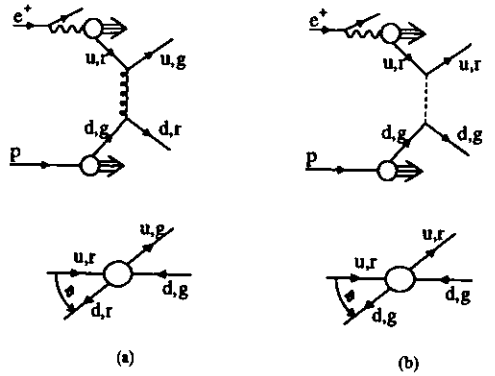

Figure 1.8: Two examples of the colour flow in hard photoproduction events at HERA. In the top view the full schematic diagram of the process is shown and in the bottom view just the hard subprocess is shown, in its centre-of-mass frame. An example of a colour non-singlet exchange event is shown in (a) and an example of a colour singlet exchange event is shown in (b).

the bremsstrahlung gluon radiation from the scattered quarks is confined to the narrow forward and rear rapidity regions, and particle production in the central rapidity region between the two quark jets is suppressed.

Such soft hadron phenomena are generally known as colour coherence phenomena [1]. It has been proposed [31], for example, to use the distinctive radiation pattern in colour singlet exchange events to search for Higgs boson production via W^+W^- fusion at the future large hadron collider (the LHC). However it has also been recognized [35] that a significant background to the Higgs signal could come from processes involving the exchange of a strongly interacting colour singlet object. For instance a simple calculation of two gluon exchange in a colour singlet state yields a rate of colour singlet exchange processes of 10% with respect to gluon exchange [35].

Hard QCD colour singlet exchange processes are themselves of great theoretical interest [28, 35–40]. For instance in processes where the final state

partons are produced with a large relative rapidity, the BFKL resummation technique [36, 37, 11] may be applied. This amounts to a description of the exchanged colour singlet object in terms of a ladder of interacting gluons, called the BFKL pomeron. However the validity of the BFKL approach has not yet been clearly established by experiment [12, 13].

QCD colour singlet exchange proceeds at lowest order via exchange of a composite object. Thus one may reasonably ask whether gluon radiation from the constituents of the colour singlet object might destroy the rapidity gap signature. A next to leading order calculation has been made of the radiation pattern of soft gluons in colour singlet exchange [11]. It was found that the radiation pattern of soft gluons is suppressed in the central rapidity region for two gluon colour singlet exchange in the same way as it is for photon exchange.

The phase space of the final state particles may be measured in terms of the "lego" variables of pseudorapidity, η, and azimuthal angle, φ. Figure 1.9 is an illustration of the lego space for a hard diffractive scattering event measured in the ZEUS detector. The black dots show the final state hadrons. There are two high transverse energy jets which are shown as circles. The

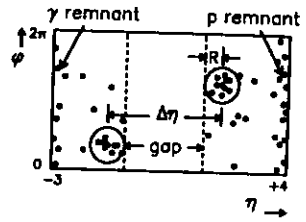

Figure 1.9: The signature of a hard diffractive scattering event at HERA. The final state particles are shown as black dots. The two high transverse energy jets are drawn as circles of radius R. The p and γ remnant jets occupy the regions of high η and low η respectively. The jets are back to back in φ and separated by a pseudorapidity interval $\Delta\eta$. There is a gap in the hadron distribution which occurs between the two jets and has a width of $\Delta\eta - 2R$.

jets have a cone radius of $R \equiv \sqrt{(\delta\eta)^2 + (\delta\varphi)^2} \leq 1$ where $\delta\eta$ ($\delta\varphi$) is the difference in pseudorapidity (azimuth) between a hadron and the centre of the jet cone. (Jet finding will be discussed in more detail in Appendix B.) The jets are separated by a pseudorapidity interval $\Delta\eta$ and are back to back in φ. There are no hadrons produced between the jet cones in the region of width $\Delta\eta - 2R$ labelled "gap". The proton remnant jet fragmentation products are found at high η and the photon remnant jet is at low η.

The signature of Figure 1.9 is expected to be produced by electroweak exchange events as well as by strong colour singlet exchange events. In addition such events can be produced in non-singlet exchange processes due to multiplicity fluctuations. In order to distinguish between these contributions an experimental observable has been defined, called the gap-fraction, $f(\Delta\eta)$.

The gap-fraction is defined as the ratio of the dijet gap cross section to the inclusive dijet cross section,

$$f(\Delta\eta) \equiv \frac{d\sigma_{gap}/d\Delta\eta}{d\sigma/d\Delta\eta}. \tag{1.3}$$

The gap-fraction is expected to exhibit two components of behaviour due to the two contributions to σ_{gap},

$$\sigma_{gap} = \sigma_{gap}^{non-singlet} + \sigma_{gap}^{singlet}. \tag{1.1}$$

It is expected that for low values of $\Delta\eta$, $\sigma_{gap}^{non-singlet}$ will be the dominant component of σ_{gap} due to random fluctuations in multiplicity. This component would be exponentially suppressed as $\Delta\eta$ increased, leading to the dominance of the $\sigma_{gap}^{singlet}$ component at large $\Delta\eta$ as illustrated schematically in Figure 1.10.

The height of the plateau region produced by the dominance of $\sigma_{gap}^{singlet}$ can discriminate between strong and electroweak processes since electroweak process only occur a fraction $\alpha^2/\alpha_s^2 \sim 0.1\%$ of the time while strong colour singlet exchange could occur in as many as 10% of events (as previously mentioned).

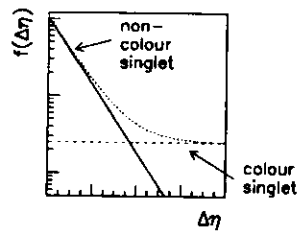

Figure 1.10: Illustration of the expected two component behaviour of the gap-fraction. Gaps produced by multiplicity fluctuations in colour non-singlet exchange events give rise to a gap-fraction which is exponentially suppressed as $\Delta\eta$ increases. The gap-fraction component due to colour singlet exchange processes does not have a strong $\Delta\eta$ dependence.

Both D0 [15, 16] and CDF [17] have reported the results of searches for dijet events containing a rapidity gap between the two highest transverse energy jets in $p\bar{p}$ collisions at $\sqrt{s} = 1.8$ TeV. Both collaborations see an excess of gap events over the expectations from colour exchange processes. D0 report an excess of $1.07 \pm 0.10(stat.)^{+0.25}_{-0.13}(sys.)\%$, whereas CDF measure the fraction to be $0.86 \pm 0.12\%$. It is very interesting to compare these results from a vastly different kinematic regime, with those of the HERA study. (This will be discussed more in Sect. 6.3.)

In this study we have measured the gap-fraction for dijet photoproduction, $ep \to e\gamma p \to eX$, where X contains at least two jets of final state hadrons[3]. The two highest transverse energy[4] jets have transverse energies of $E_T^{jet} > 6$ GeV and a relative pseudorapidity of $\Delta\eta > 2$. These two jets in addition have pseudorapidities satisfying $\eta^{jet} < 2.5$ and the average pseudorapidity of the two jets satisfies $|\bar{\eta}| < 0.75$. The gap-fraction is measured for γp centre-of-mass energies in the range 134 GeV $< W_{\gamma p} <$ 277 GeV, or equiv-

[3]We use the generic term "hadrons" to refer to all of the final state particles except the scattered positron.

[4]One of the theoretical predictions for the gap fraction [37] uses instead the two jets at highest and lowest pseudorapidity. The uncorrected gap-fraction with this definition is discussed in Appendix C.

alently for values of y in the range $0.2 < y < 0.85$. The photon virtualities satisfy $P^2 < 1$ GeV^2.

Gap events are defined as having *no* final state particles between the jet cones of transverse energy $E_T^{hadron} > 300$ MeV. The particle transverse energy threshold will be convenient experimentally as it makes the definition of a gap less sensitive to detector noise or inefficiency. It also has a theoretical interpretation as the scale below which soft gluon radiation is allowed into the gap [36, 37] and the theoretical advantage that it tends to restrict to particles with pseudorapidities which are close to the true rapidities [18]. There are even proposals to define gap events at the LHC using a jet transverse energy threshold of 20 GeV [19].

Chapter 2

Experimental Apparatus

The ZEUS detector has been used to study photoproduction events from e^+p collisions delivered by the HERA (hadron elektron ring anlage) accelerator in 1991. This experimental apparatus is described in the following.

2.1 The HERA accelerator

HERA is the world's only positron proton collider [50 52]. It consists of separate positron and proton accelerators in a 6.3 km circumference. The positron and proton beams can be brought into head-on collision at four locations evenly spaced around the HERA ring as shown in Figure 2.1.

HERA was designed to make use of the machines which already existed at DESY (Deutsches elektronen synchrotron). Positrons are obtained from a 500 MeV linear accelerator (labelled e on Figure 2.1) and injected into a small synchrotron. There they are accelerated to 7 GeV and injected into PETRA. PETRA accelerates the positrons to 11 GeV before they are injected into HERA. Then they are accelerated to 27.5 GeV. The protons are obtained from a 50 MeV H^- linear accelerator. The H^- ions are stripped of their electrons when injected into the small proton synchrotron. There the protons are accelerated to 7.5 GeV for injection into PETRA. The HERA injection energy for protons is 40 GeV and HERA accelerates the protons to

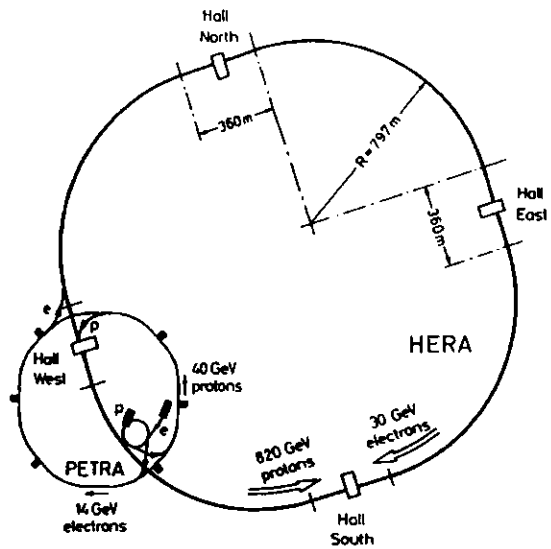

Figure 2.1: The layout of the HERA accelerator complex, showing the p and e^+ linacs, the sequence of preaccelerators, and the HERA ring, with the four experimental halls.

820 GeV.

The design instantaneous luminosity for HERA is $1.6 \cdot 10^{31}$ cm^{-2} s^{-1}. The average luminosity achieved in 1994 was much lower, $2.3 \cdot 10^{30}$ cm^{-2} s^{-1}, while still constituting an improvement over the 1993 value, $1 \cdot 10^{30}$ cm^{-2} s^{-1}. The luminosity is limited by the e^+ and p bunch currents. In fact, HERA originally supplied an electron beam rather than a positron beam but early in 1991 it was discovered that the electron current was limited by electron interactions with ionized dust in the imperfect vacuum of the beam pipe.

Therefore it was decided to switch to positron operation.

In 1994 HERA provided 820 GeV protons and 27.5 GeV positrons colliding in 153 bunches. 15 unpaired positron bunches and 17 unpaired proton bunches were also circulated. These allow monitoring of background from beam-gas interactions. In addition 21 empty bunches were used to monitor contamination from cosmic ray interactions.

2.2 The ZEUS detector

The ZEUS detector occupies the south hall shown in Figure 2.1. The layout of the ZEUS detector is shown in Figure 2.2. The primary components used in this analysis are the forward, barrel and rear calorimeters (FCAL, BCAL and RCAL), the central tracking detector (CTD) and the vertex detector (VXD). In addition the luminosity monitor (LUMI) was used. Three minor components, the C5 counter, the vetowall and the small angle rear tracking detector (SRTD), are used in the event selection. These components are described in the following. Further details about these and the other components of the ZEUS detector may be obtained elsewhere [53]. In the ZEUS coordinate system the nominal interaction point is at $(x, y, z) = (0, 0, 0)$ and the positive z axis points in the direction of the proton beam, i.e. towards FCAL.

2.2.1 The Calorimeter

The study of processes involving the formation of high transverse energy jets in the final state relies primarily upon the signals produced in the calorimeter. The essential function of a calorimeter is to absorb an incident particle and to convert its energy into a measurable quantity such as electric charge [51]. Calorimeters measure the energies and positions of both charged and neutral particles with a fast time response and an energy resolution which improves with energy.

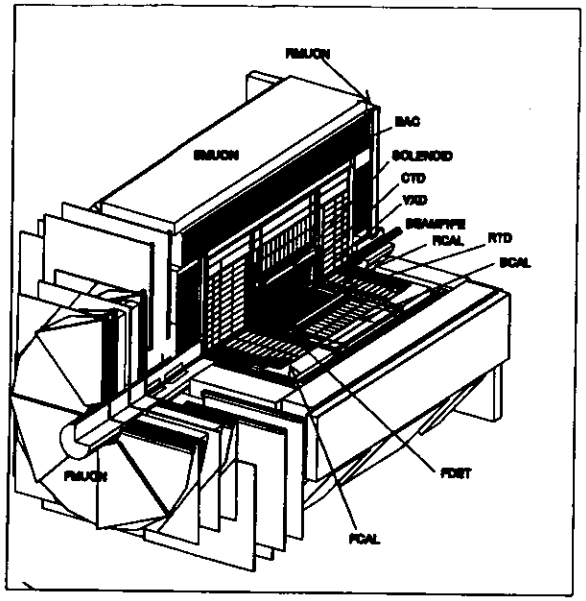

Figure 2.2: The components of the ZEUS detector, showing in particular the vertex detector (VXD) next to the beam pipe, the central tracking detector (CTD) which surrounds the VXD and is encased in a solenoidal magnet (SOLENOID) which provides a 1.43 T magnetic field. Surrounding the CTD are the forward, barrel and rear calorimeters (FCAL, BCAL and RCAL respectively).

For instance, an energetic electron impinging upon a block of dense material will radiate photons in a bremsstrahlung process in the electromagnetic field of the atomic electrons and nuclei. The radiated γ's will in turn pair produce e^+'s and e^-'s which will radiate more γ's and so an electromagnetic "shower" is developed. The characteristic distance of this shower is the radiation length, X_0, over which an electron's energy drops by a factor

of $1/e$. When the energy of the shower particles becomes too low for the bremsstrahlung and pair production processes, the remaining energy is lost primarily through ionization and compton scattering. An electromagnetic shower characterises the response of the calorimeter to incident γ's, e^-'s and e^+'s and also to incident π^0's (which convert quickly to $\gamma\gamma$). It is the charged particles produced in the electromagnetic shower which ultimately give rise to the signal measured by the calorimeter.

The process of particle absorption proceeds quite differently for hadrons. These interact with the nuclei of the absorber to produce more hadrons or induce a nuclear decay. The produced hadrons interact further with nuclei and thus a hadronic shower is developed. Some fraction of the time a π^0 will be produced which will give rise to an electromagnetic shower component. One major difference between hadronic and electromagnetic shower development is that some energy may be lost in a hadronic shower to nuclear binding energy. Thus the ratio of the electron signal to the hadron signal, e/h is generally greater than one.

It is easy to imagine difficulties which can arise with an instrument that has $e/h > 1$. For instance, selecting events according to the energy deposited by an incident hadron would introduce a bias toward hadron showers which produced a π^0 early in their development and thus had a large electromagnetic component. A sampling calorimeter has different absorbing and active materials. Using a sampling calorimeter and varying the relative volume of absorbing and active materials it is possible to make a compensating calorimeter which has $e/h = 1$.

The ZEUS calorimeter [55 58] is a sampling calorimeter which uses plates of depleted uranium as the absorbing material interleaved with SCSN-38 scintillator tiles as the active material in layers of about 8 mm total thickness (or $1X_0$). It is longitudinally segmented into an electromagnetic section (EMC) followed by two hadronic sections (HAC) in the forward and barrel regions or one hadronic section in the rear region. The total depth is 1.52 m in FCAL,

1.08 m in BCAL and 0.9 m in RCAL. Typical lateral EMC cell dimensions range from 5×20 cm^2 in the forward direction to 10×20 cm^2 in the rear direction. The typical lateral HAC cell dimension is 20×20 cm^2. The scintillation light is collected by wavelength shifting plates and transmitted by total internal reflection onto a light guide which directs it into a photomultiplier tube.

Compensation is achieved at the level $e/h = 1.00 \pm 0.02$ over the energy range of 2 to 100 GeV. The depth ensures containment in excess of 95% for 90% of the particle jets in all parts of the calorimeter. The calorimeter covers 99.7% of the total solid angle. The pseudorapidity coverage by FCAL, BCAL and RCAL is $4.3 \geq \eta \geq 1.1$, $1.1 \geq \eta \geq -0.75$ and $-0.75 \geq \eta \geq -3.8$ respectively. The calorimeter energy resolution achieved in test beams, in terms of the energy E in GeV, is $\sigma_E/E = 18\%/\sqrt{E}$ for electrons. For hadrons of energy above 10 GeV the energy resolution is $\sigma_E/E = 35\%/\sqrt{E}$. It improves to $\sigma_E/E = 26\%/\sqrt{E}$ for hadrons of energy 0.5 GeV. The timing resolution of a calorimeter cell is better than[1] $\sigma_t = 1.5/\sqrt{E} \oplus 0.5$ ns.

2.2.2 Charged Particle Detection

The first ZEUS component encountered by charged particles leaving the interaction region is the VXD [59], a cylindrical drift chamber which consists of 120 radial cells, each with 12 sense wires. Surrounding the VXD is the CTD [60] which consists of 72 cylindrical drift chamber layers, organized into nine "superlayers". Five of these superlayers have wires parallel to the beam axis and four have wires inclined at a small angle to provide a stereo view. The tracking chambers are filled with gas mixtures which are ionized by the charged particle as it passes through. The ionization electrons drift in the electric fields of the cells and the avalanche of ionization which occurs near the sense wires causes an electric pulse which registers that the wire has been hit. The pattern of hits and the associated drift times are then used to reconstruct

[1] The symbol $\oplus$ is used to indicate addition in quadrature.

the path traversed by the charged particle. The charged particle experiences a transverse force due to a 1.43 T solenoidal magnetic field which causes it to curve and allows its momentum to be reconstructed. The resolution in transverse momentum for full length tracks is $\sigma_{p_T}/p_T = 0.005 p_T \oplus 0.016$ (for p_T in GeV). For events with several charged tracks the interaction vertex may be measured with a resolution along (transverse to) the beam direction of 0.4 (0.1) cm.

2.2.3 Luminosity Measurement

The luminosity, $\mathcal{L}$, is determined by measuring the rate, R, of the bremsstrahlung process, $e^+p \to e^+\gamma p$. The bremsstrahlung events are detected by tagging of the outgoing photon in a lead-scintillator calorimeter [61] which is installed at a distance of 104 m from the nominal interaction point in the positron beam direction. The acceptance of this detector $\mathcal{A}_{LUMI}$ may be determined by Monte Carlo methods and bremsstrahlung has a known cross section, σ_B. Thus $\mathcal{L}$ may be simply calculated from[2] $\mathcal{L} = R/(\mathcal{A}_{LUMI} \otimes \sigma_B)$.

In addition there is an electron lead-scintillator calorimeter [61] situated at 35 m from the nominal interaction point. This is used in the calibration of the γ calorimeter and also to tag a subsample of the photoproduction events where the positron is scattered through an angle of less than 6 mrad.

2.2.4 Background Veto

Two auxiliary detectors are installed just upstream (with respect to the proton beam) of the main detector which are very useful in vetoing background interactions. The C5 beam monitor is a small lead-scintillator counter installed 3.2 m from the nominal interaction point (i.e. just behind the RCAL). It is used to detect upstream proton beam interactions and to measure the timing of the proton and positron bunches. The vetowall detector consists of

[2] The symbol $\otimes$ is used to indicate a convolution over the relevant range of γ four-momenta.

two layers of scintillator on either side of an 87 cm thick iron wall 7.3 m from the nominal interaction point. It absorbs most beam halo particles accompanying the proton bunches, and provides trigger veto information for those which pass through. The SRTD is a set of scintillator strip planes attached to the front face of the RCAL. Its primary purpose is to improve the detection of positrons scattered close to the positron beam direction. However for this analysis it was used to improve the rejection of upstream proton beam interactions based on timing.

Chapter 3

Data Selection

An example of a dijet photoproduction event registered in the ZEUS detector is shown in Figure 3.1. Here the energy and position measurements of the

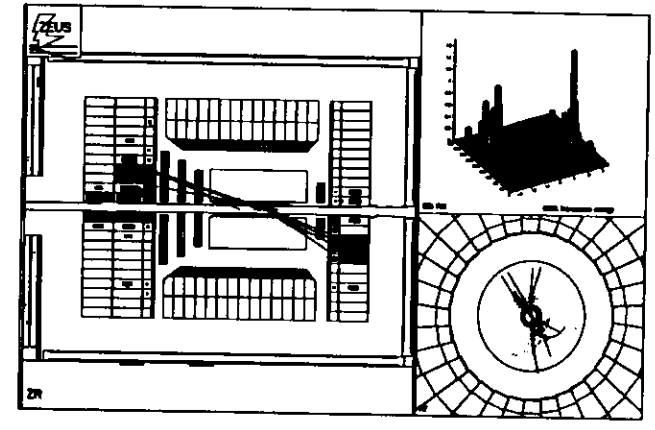

Figure 3.1: A dijet photoproduction event as seen by the ZEUS detector. The left side shows the rz view of the reconstructed tracks and the energy deposits in the calorimeter. The upper right view shows the energy deposits in the calorimeter in the η, φ plane and the lower right picture shows the xy view of the reconstructed tracks.

calorimeter and central tracking detector for a single event are displayed in three different views.

The upper right view shows the transverse energy deposits in the calorimeter, according to their position in η, φ space. It is the experimentalists view of the schematic lego signature for hard diffractive scattering shown in Figure 1.9. There are two well collimated jets in the lego plot, of $E_T^{jet} \sim 5$ GeV at $\eta^{jet} \sim -1.5$ and $\eta^{jet} \sim 2.5$ and back to back in φ.

The rz view is shown on the left side. The shaded area in each CAL cell is proportional to the energy deposited in the cell. The hit wires of the CTD are shown with the tracks which have been reconstructed from them. There are large energy deposits in the forward and rear calorimeter sections which are associated with the jets. There is a well defined vertex of tracks close to the nominal intersection point. Several tracks point from the vertex to each jet. There is also a large energy deposit around the forward beam pipe, associated with the proton remnant jet. Near the rear beam pipe is a small energy deposit which can be associated with the photon remnant.

The xy view of the event is shown in the lower right picture. One can see the back to back spray of charged particles associated with the two jets, and the good resolution in the xy position of the vertex.

We make use of the properties of high transverse energy in the calorimeter, a well defined vertex and several tracks in the CTD in order to select a sample of dijet photoproduction events. In addition to keeping the hard photoproduction events of interest our selection criteria must reject the large backgrounds due to interactions of the proton beam with the beam gas (p beam gas interactions), collisions between the proton beam and the beam wall (beam scraping), beam halo particles and cosmic ray events.

3.1 Online Triggers

The most difficult background comes from the p beam gas interactions which occur at a rate of about 50 kHz while the rate at which ZEUS can write events to tape is a few Hz. The bunch crossing time of 96 ns (or rate of 10 MHz) poses additional problems in that no component is able to read out its data and provide a trigger decision in such a short time. The ZEUS solution is a deadtimeless three-level pipelined trigger system [53].

For every bunch crossing all data are stored in a pipeline clocked at 96 ns. The job of the first level trigger (FLT) is to reduce this 10 MHz rate to an output rate of 1 kHz, taking no more than 16 bunch crossings to make its decision on each event. The calorimeter is able to provide global energy sums within a few μs of the bunch crossing. The calorimeter information used at the FLT for this analysis is itemized in the following.

- E_{EMC}^{FLT} is the sum of all energies of all EMC cells.
- E_{BEMC}^{FLT} is the sum of all energies of all BCAL EMC cells.
- E_T^{FLT} is the sum of the magnitudes of all cell transverse energies (using the nominal vertex position to obtain the cell angle).
- E^{FLT} is the summed energy of all cells, and
- E_{REMC}^{FLT} is the sum of all energies of all RCAL EMC cells.

We require a large energy deposit in the calorimeter at the FLT. That is, ($E_{EMC}^{FLT} > 10$ GeV or $E_{BEMC}^{FLT} > 3.1$ GeV or $E_T^{FLT} > 12$ GeV or $E^{FLT} > 15$ GeV or $E_{REMC}^{FLT} > 2$ GeV). The CTD is able to provide preliminary tracking information to the FLT and we have required at least one track pointing toward the nominal vertex. Finally we have used timing information from the vetowall, the C5 counter and the SRTD, at the FLT, to reject p beam gas and beam scraping events which occur upstream of the detector, and to reject triggers due to beam halo particles.

At the second level trigger (SLT) the full data for the event is available and the rate must be reduced from 1 kHz to 100 Hz. The calorimetric energy sums used are,

- E, the total energy of all calorimeter cells,
- E_T, the sum of the magnitudes of the transverse energies of all calorimeter cells,
- E_T^{FB}, the sum of the magnitudes of the transverse energies of the calorimeter cells adjacent to the FCAL beam pipe, and
- p_z, the summed longitudinal energies of all cells.

Vertex information was not available at the SLT in 1991 so E_T, E_T^{FB} and p_z were calculated assuming the nominal interaction point. We required $E_T - E_T^{FB} > 8$ GeV in order to select high transverse energy events (where the high transverse energy is not entirely due to the proton remnant). p beam gas events are enormously boosted in the p direction and are therefore characterized by $p_z \sim E$. We have required $E - p_z > 8$ GeV and ($E - p_z >$ 12 GeV or $p_z/E < 0.95$) in order to suppress p beam gas events.

The third level trigger (TLT) reduces the event rate from 100 Hz to about 3 Hz. The data are processed through the offline reconstruction code. Detailed iterative algorithms may be applied to perform an online analysis of the data. We have required a good reconstructed vertex at the TLT level. We have also run a jet finding algorithm at the TLT. (Further details may be found in Appendix B.) We then require that two or more jets be found with ($(E_T^{jet} > 4$ GeV and $2.0 \leq \eta^{jet} < 2.5)$ or $(E_T^{jet} > 3.5$ GeV and $\eta^{jet} < 2.0)$).

The calorimeter timing measurements provide crucial information for further background rejection at the SLT and TLT levels. The difference between the average time of energy deposits in the upper half of the BCAL and the average time of energy deposits in the lower half of the BCAL is used to reject cosmic ray events at the SLT and TLT. The average time of FCAL energy

deposits, t_{FCAL}, and the average time of RCAL energy deposits, t_{RCAL} are used to reject p beam gas. These distributions are shown in Figure 3.2 for a clean sample of dijet events[1]. The FCAL and RCAL timing distributions

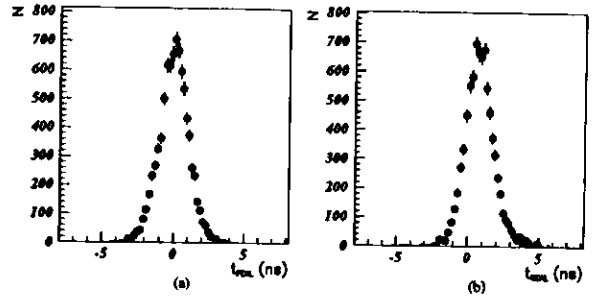

Figure 3.2: The distribution of the average time of FCAL energy deposits is shown in (a) and the distribution of the average time of RCAL energy deposits is shown in (b).

are narrowly distributed about the nominal value. In contrast, p beam gas events which occur upstream of the main detector give rise to RCAL times of $t_{RCAL} \sim -10$ ns. These events are rejected with the cuts, $t_{RCAL} > -6$ ns and $t_{FCAL} - t_{RCAL} > 6$ ns. These cuts are clearly safe for the hard photoproduction events as shown by Figure 3.2.

In fact the timing resolution is somewhat better than that suggested by Figure 3.2. The tails of the t_{FCAL} distribution are due to e^+p interactions with a vertex z position away from the nominal interaction point. Figure 3.3 shows the t_{FCAL} vs z distribution for the clean sample of dijet events. e^+p collisions at positive z arrive early at the FCAL giving rise to negative t_{FCAL} signals and vice versa.

In addition there are global vetoes at the SLT and TLT to reject events which are triggered by a photomultiplier tube spark events based on the number of hit cells and on the imbalance of energy read out from the two

[1]The label N on the vertical axis refers to the number of events per bin, throughout.

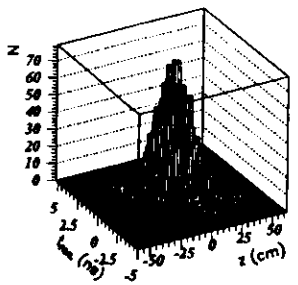

Figure 3.3: The average time of the FCAL energy deposits versus the z-position of the vertex as determined by the tracking detectors.

photomultiplier tubes of a cell. The characteristic pattern of hit cells for cosmic muons and for muons which travel in the p beam halo is used to reject these backgrounds at the SLT and TLT levels.

3.2 Offline Selection

We find jets offline from the calorimeter cell energies and angles using a cone jet finding algorithm (described in detail in Appendix B). We require that there be at least two jets and that the two highest transverse energy jets satisfy[3] $E_T^{jet} > 5$ GeV, $\eta^{jet} < 2.5$, $|\bar{\eta}| < 0.75$ and $\Delta\eta > 2$. The cut $\eta^{jet} < 2.5$ is necessary to select jets which lie entirely within the acceptance of the calorimeter. The average jet pseudorapidity, $|\bar{\eta}|$, is to leading order the boost of the hard subsystem. The restriction $|\bar{\eta}| < 0.75$ selects events where at least one of the jets goes in the rear direction. The online triggers are more efficient for these events. In addition it selects events where a large fraction of the photon's energy participates in the hard interaction. (The

[3]The reader may notice that the E_T^{jet} threshold used in the offline selection is lower than the E_T^{jet} threshold of the measured cross sections as detailed in Sect. 1.4. This is due to the E_T^{jet} resolution and will be discussed in Sect. 4.3.

mean value of x_γ^{OBS} is 0.7. This is discussed further in Sect. 6.3.) These events are better simulated by the Monte Carlo generators because there is less uncertainty in the photon parton distribution function and because there is a lower likelihood of a secondary interaction taking place between the photon and proton constituents. We are not interested in events where the jet cones are overlapping in η and that is the reason for the cut $\Delta\eta > 2$.

Additional offline cleaning criteria are applied to further suppress p beam gas and cosmic ray events. There are also now considerable backgrounds from non-photoproduction e^+p collisions which must be suppressed.

The following figures show the effects of each successive cleaning cut on the selected dijet event sample (dashed line) where the cut value is shown as a vertical line. As an illustration of the background to be rejected the solid line shows a loose dijet sample ($E_T^{jet} > 4$ GeV). The dotted line shows the subsample of the selected dijet sample which has an energy deposit in the e^+ LUMI calorimeter of more than 5 GeV (and no corresponding energy deposit in the γ LUMI calorimeter). This sample has very low backgrounds.

Two important cuts are based on measurements of the dimensionless y variable (see Appendix A) which in photoproduction events is equivalent to the momentum fraction of the positron which is carried by the photon. One estimate of y, y_{JB} [62], is based on the hadronic energy deposits in the calorimeter. $y_{JB} = (E - p_z)/(2E_e)$, where E is the summed energies of all calorimeter cells, p_z is the summed longitudinal energies of all calorimeter cells and E_e is the incident positron energy, 27.5 GeV. The y_{JB} distribution is shown in Figure 3.4(a). Clearly, a fully hermetic calorimeter will always have $y_{JB} = 1$ and in fact in DIS events where the scattered e^+ is scattered at a large angle and contained in the calorimeter, $y_{JB} \sim 1$. The contribution of DIS events can be seen as a peak to high values of y_{JB} in Figure 3.4(a). We reject this DIS background with the requirement $y_{JB} < 0.7$. Recall that the requirement $E - p_z > 8$ GeV has been made at the SLT. Therefore the allowed y_{JB} range is given by $0.15 < y_{JB} < 0.7$.

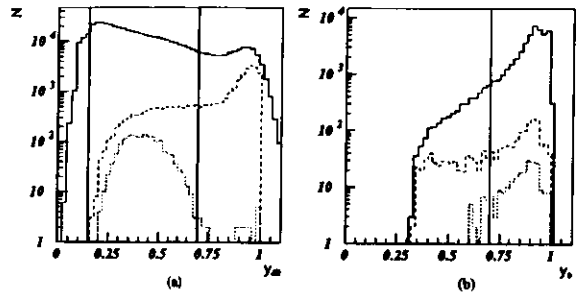

Figure 3.4: Distribution of the y estimators. The solid line shows a loose sample of dijet events. The dashed line shows the sample of dijet events which will be used in this analysis and the dotted line shows a clean sample of photoproduction events where the scattered e^+ is measured in the e^+ LUMI detector. y_{JB}, which is estimated using the hadronic energy deposits in the calorimeter, is shown in (a) and y_e, which is estimated using the energy deposits of a scattered e^+ candidate, is shown in (b).

Some events remain which have a scattered e^+ candidate measured in the calorimeter. For these events y can be measured using $y_e = 1 - E'_e(1 - \cos\vartheta'_e)/(2E_e)$ where E'_e and ϑ'_e are the energy and angle of the scattered e^+ candidate, respectively. The y_e distribution is shown in Figure 3.4(b). The LUMI tagged photoproduction events have high values of y_e (dotted line). These are due to electromagnetic showers from π^0 and η mesons. Low values of y_e are due to DIS events [63]. Therefore, for those events which have a scattered e^+ candidate, we make the cut $y_e > 0.7$.

Reconstructed track distributions are used to further suppress p beam gas and cosmic ray contamination. Figure 3.5(a) shows the distribution of $N_{bad\,track}$, the number of tracks which intersect the beam axis at $z < -75$ cm. p beam gas events have high values of $N_{bad\,track}$ and the p beam gas contribution to the loose dijet sample is clearly apparent in Figure 3.5(a). We have made the requirement $N_{bad\,track} < 3$ in order to suppress beam gas events.

Cosmic ray events tend to give rise to exactly two reconstructed tracks

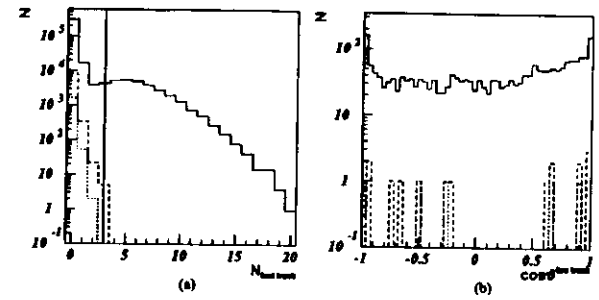

Figure 3.5: Tracking cuts to suppress beam-gas and cosmic contamination. The solid line shows a loose sample of dijet events. The dashed line shows the sample of dijet events which will be used in this analysis and the dotted line shows a clean sample of photoproduction events where the scattered e^+ is measured in the e^+ LUMI detector. The distribution of the number of tracks which point to a vertex in the rear is shown (a). The distribution of the opening angle between the two tracks for events which have only two tracks is shown in (b).

which are back to back. The opening angle between the two tracks, $\vartheta^{two\,track}$ satisfies $\cos\vartheta^{two\,track} \sim -1$. Figure 3.5(b) shows the distribution of $\cos\vartheta^{two\,track}$. We have made the requirement $\cos\vartheta^{two\,track} > -0.996$ in order to reject cosmic ray events.

The z distribution of the reconstructed vertex is shown in Figure 3.6(a). We have selected the events with -50 cm< z <50 cm which are within the detector acceptance. This cut also rejects some non-e^+p collision backgrounds.

The last significant background which remains in the sample is due to charged current events. In these events the final state hadrons are balanced in transverse momentum by an outgoing neutrino. The neutrino escapes undetected and so the energy deposits in the calorimeter exhibit a large momentum imbalance, $|\vec{p_T}|$. Of course, photoproduction events with large transverse energy jets in the final state could also have a large value of $|\vec{p_T}|$ due to statistical fluctuations. Therefore the relative missing transverse momentum, $|\vec{p_T}|/\sqrt{E_T}$, is used to reject charged current events. Figure 3.6(b)

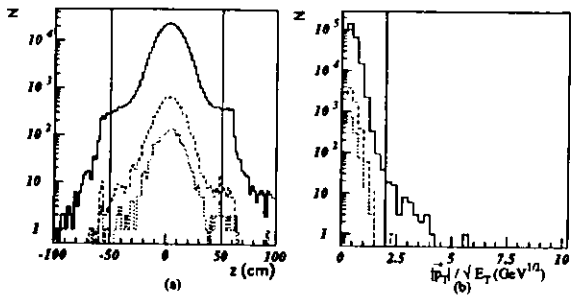

Figure 3.6: The distribution of the z-position of the reconstructed vertex is shown in (a). The distribution of the relative missing transverse momentum in the calorimeter, $|\vec{p_T}|/\sqrt{E_T}$, is shown in (b). The solid line shows a loose sample of dijet events. The dashed line shows the sample of dijet events which will be used in this analysis and the dotted line shows a clean sample of photoproduction events where the scattered e^+ is measured in the e^+ LUMI detector.

shows the distribution of $|\vec{p_T}|/\sqrt{E_T}$. The cut $|\vec{p_T}|/\sqrt{E_T} < 2$ GeV$^{1/2}$ has been applied to reject the charged current events.

The last step which must be taken to define the sample of events for the study is to measure the particle multiplicity in order to select gap events. The particle multiplicity is determined by grouping calorimeter cells into "islands" [61]. This is done by assigning to every cell a pointer to its highest energy neighbour. A cell which has no highest energy neighbour is a local maximum. An island is formed for each local maximum which includes all of the cells that point to it. The events with *no* islands of transverse energy $E_T^{island} > 250$ MeV, and pseudorapidity, η^{island}, between the edges of the jet cones (as defined by the cone radius R) are called gap events.

From 2.6 pb^{-1} of e^+p collisions delivered by HERA in 1994 the number of events remaining in the data after this selection is 8393. The non-e^+p collision background was estimated using the number of events associated with unpaired bunch crossings. The p beam gas background was found to

be less than 0.1%. The cosmic ray contamination is estimated to be about 0.1%. The 13 gap events which have $\Delta\eta > 3.5$ were also scanned visually to search for contamination from events where the energy deposits of the scattered positron or a hard final state photon might mimic a jet. No such events were found.

Chapter 4

Data Simulation and Description

In this chapter a description is provided of how the Monte Carlo event samples are obtained. Then the general characteristics of the Monte Carlo events are compared with those of the ZEUS data.

4.1 The Monte Carlo Event Samples

When one chooses a random number n, which lies between say 1 and m, according to a probability distribution $\mathcal{P}(n)$ one essentially throws a weighted, m-sided, die. For this reason, computer programs which rely on random number generation have come to be known as Monte Carlo programs. In order to simulate high energy physics data these dice must be thrown many times in many subroutines but it is possible to group these routines into two main programs; the event generator, and the detector simulator.

4.1.1 Event Generation

As shown in Figures 1.4(a) and (c) hard photoproduction in the LO QCD picture has exactly two hard partons in the final state. However we know that gluons are radiated from the quark and gluon lines and that in addition

photon radiation can occur from the lepton and quark lines. This parton shower process ends with the transformation of the coloured partons into colourless hadrons which can then decay, producing even more particles. In fact, at HERA energies around 50 final state particles are produced per hard photoproduction event. How then, is one to make a confrontation with the LO theory which predicts exactly two hard partons in the final state?

Owing to the large probability that interactions occur at low momentum transfer, the global event characteristics will actually closely follow those of the parent partons. However, any detailed study of the final state requires some understanding of the parton showering, hadronization and decay processes. The parton showering processes can in principle be calculated perturbatively where the branchings are of sufficiently hard scale. However in practice, few calculations are available beyond order α_s^3 while typical hard photoproduction events contain around 10 of such parton branchings. The hadronization process which occurs at large values of α_s cannot, even in principle, be calculated in perturbative QCD.

The solution to this problem lies in the factorization property of QCD. It is possible to calculate separately just the hard subprocess cross section using perturbative QCD. Then the probability distribution for the initial and final state parton showers can be evolved between the hard scattering scale and the hadronization scale according to the GLAP evolution (see Sect. 1.2). The probability distributions for the final state particles with respect to their parent partons must be obtained from a phenomenological model. In the Lund string model [65], for instance, the colour field between two coloured partons is thought of as a string which extends as the partons move apart until its tensile energy is high enough to provide masses for two (or more) new partons. Eventually all of the coloured partons are associated by strings into colour singlet states which do not have sufficient invariant mass to break apart. These are the final state hadrons. The Lund string model has proven very successful in describing experimental data [66].

A computer program is ideally suited to generate separate events by choosing a "random" final state configuration weighted by the hard cross section probability distribution, the parton showering probability distributions and the hadronization probability distributions.

We have used the PYTHIA [67, 68] Monte Carlo program to generate hard photoproduction events. The minimum scale of the hard subprocess is set by restricting the transverse momentum, $|\vec{p}_T|$, of the two outgoing partons to $|\vec{p}_T| > 2.5$ GeV. The parton distributions of the proton are generated according to the MRSA [69] parametrizations. LO resolved photon events are generated using the GRV [21] parton distributions for the photon. LO direct events are generated separately and combined with the LO resolved processes. We shall refer to three PYTHIA samples in the following. The "non-singlet" sample contains the standard QCD processes which proceed via quark or gluon propagators. The "singlet" sample contains only the LO resolved process of quark-quark scattering via γ/Z^0 or $W^{\pm}$ (electroweak) exchange. There is finally a "mixed" sample which consists of 90% of the non-singlet sample with 10% of the singlet sample. Thus the mixed sample contains electroweak exchange processes at two orders of magnitude higher cross section than they are expected to occur from the estimation $(\alpha/\alpha_s)^2 \sim 0.001$. This is done in order to simulate a possible strong colour singlet exchange process which is not implemented in PYTHIA.

4.1.2 Detector Simulation

The responsibility of the PYTHIA program ends when the generated event consists of leptons and hadrons including the relatively short-lived $K^0_s, \eta, \Lambda^0, \ldots$ particles. The lifetimes of these particles is such that they may decay within the volume of the ZEUS detector. Therefore their interaction in the apparatus must be taken into consideration. This is the responsibility of the detector simulation program MOZART (Monte Carlo for ZEUS analysis reconstruction and trigger).

MOZART is an extensive software program which uses the GEANT [70] package of detector description and simulation tools. MOZART contains a detailed description of all of the detector component materials and positions. In fact, Figure 2.2 of the ZEUS detector was generated using MOZART. MOZART simulates the passage of generated particles through the ZEUS detector including the ionization energy loss in the tracking chamber, the random chance of energy loss into dead material and the smearing of the energy resolution as a particle showers in the calorimeter. These processes are all statistical in nature and handled with random number generation on a probability distribution. Thus detector simulation code is also referred to as a Monte Carlo program.

The output of MOZART consists of the tables of information of what wires were hit, which calorimeter cells contained what energy, etcetera. These tables are formatted in exactly the same way as the information read out by the ZEUS detector from an actual HERA event. Thus the reconstruction programs which find tracks from the hit pattern, or jets from the pattern of energy deposits in the calorimeter, do not know whether an analyzed event is simulated or data. Thus it is possible to do a complete analysis in parallel on Monte Carlo and on HERA data. In this way theoretical predictions as implemented in the event generation code may be compared directly to measured data.

There is a second way to use the generated events which have been passed through the detector simulation. The relationship between the Monte Carlo detector-level distributions and the Monte Carlo hadron-level distributions can be used to correct the data for the detector effects and to produce what is called a hadron-level measurement. This measurement may then be compared with different theoretical models (which may not have been implemented into a Monte Carlo event generator).

4.2 Monte Carlo Description of Data

The measured gap-fraction will be interpreted through comparison with the gap-fractions of the Monte Carlo event samples described in the previous section. In addition the non-singlet and the mixed samples will be used to determine the efficiency of the selection criteria and the acceptance and smearing of the detector on the reconstructed quantities. Therefore an adequate description of the event properties must be provided by these two samples. The singlet sample has very different event characteristics from the data and will not be used in determining the detector acceptance. In the following figures the data are compared to the non-singlet sample and the singlet sample. The mixed sample is very similar to the non-singlet sample except at large $\Delta\eta$ and low multiplicity. Therefore this sample is not shown in general. A black dot indicates ZEUS data. The non-singlet PYTHIA sample is shown as an open circle and the singlet sample is shown as stars. Unless otherwise noted, the Monte Carlo samples are normalized to the (inclusive) number of events in the data and N on the vertical axis shows the number of events per bin.

4.2.1 Selection Criteria

Global calorimetric energy sums are shown in Figure 4.1. The energy deposited in the FCAL, E_{FCAL}, is shown in Figure 4.1(a). The data exhibit a tail to very high values of E_{FCAL} which is not reproduced by either Monte Carlo sample. This forward energy discrepancy has previously been observed by both the H1 [71] and the ZEUS [72] collaborations. It is thought to be related to multiple interactions of the photon and proton, which are not simulated in the PYTHIA samples used here. (A small sample of PYTHIA events with multiple interactions is used in comparisons with the corrected data in Sect. 6.1.) However the FCAL energy discrepancy does not pose a critical problem for this analysis as it is concentrated in a narrow cone

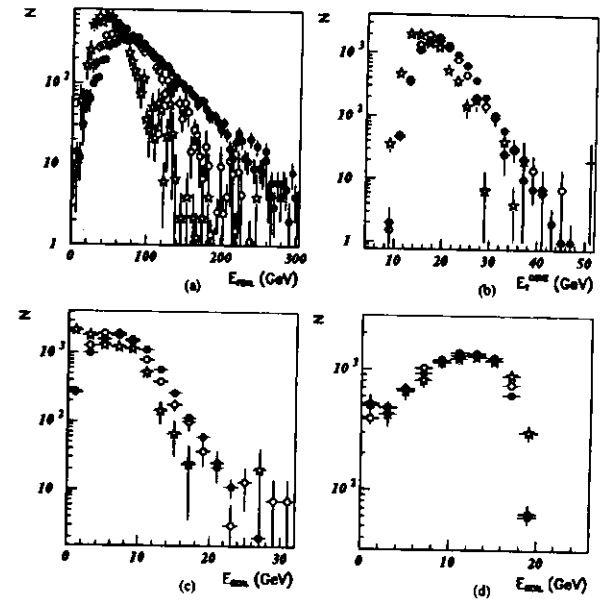

Figure 4.1: Global energy sums. The ZEUS data are shown by black dots. The prediction by the PYTHIA sample with no colour singlet exchange events (the non-singlet sample) is shown by the open circles and the prediction by the PYTHIA sample with only electroweak quark-quark scattering (the singlet sample) is shown by the stars. In (a) the distribution of the total energy deposited in the FCAL is shown. In (b) the distribution of the transverse energy outside a cone of 10° is shown. In (c) one sees the distribution of the energy deposited in the BCAL and in (d) one sees the distribution of the energy deposited in the RCAL.

about the forward direction. Figure 4.1(b) shows the summed cell transverse energies for cells which have an angle of more than 10° from the z-axis, E_T^{CONE}. The selection criteria choose events with $E_T^{CONE} > 8$ GeV and the data exhibit a tail out to $E_T^{CONE} \sim 50$ GeV. The E_T^{CONE} distribution is well

described by the non-singlet sample. The BCAL energy, E_{BCAL}, is shown in Figure 4.1(c). In the data and the non-singlet sample the average event deposits about 8 GeV of energy in the BCAL, however in the singlet sample a large fraction of events deposit < 2 GeV of energy in the BCAL. The RCAL energy distribution is shown in Figure 4.1(d). E_{RCAL} is well described by the non-singlet sample. Global energy sums are used at the first and second level triggers to accept hard photoproduction events. The good description of the global energy sums by the non-singlet (and mixed) samples means that we can use these samples to determine the efficiencies of these triggers.

Another important quantity which is used in selecting the sample at both the SLT and TLT levels is y_{JB}. The y_{JB} distribution is shown in Figure 4.2(a). The y_{JB} distribution shows that the selection cuts favour events where half or more of the momentum of the e^+ is transferred to the almost real γ. The y_{JB} distribution is also well described by the non-singlet sample.

For events in which the e^+ is detected in the e^+ LUMI detector one may estimate y directly using the scattered positron energy E'_e and the incoming positron energy E_e according to, $y_{LUMI} = (E_e - E'_e)/E_e$. The correlation between y_{JB} and y_{LUMI} is shown in Figures 4.2(b), (c) and (d) for the data, the non-singlet sample, and the singlet sample respectively. That y_{JB} is well correlated with y_{LUMI} in the data, and that the simulations describe this correlation, increase our confidence that there is little background in the data.

The other quantities which are used in the offline cleaning cuts (see Sect. 3.2) are shown in Figure 4.3. The distribution of y_e for events with a scattered e^+ candidate in the calorimeter and the distribution of the number of rear pointing tracks are well described by the non-singlet Monte Carlo sample as can be seen in Figures 4.3(a) and (b). Likewise one can see from Figures 4.3(c) and (d) that the distribution of the opening angle between two tracks in events with only two tracks and the distribution of the relative missing transverse momentum are also well described by the non-singlet sample.

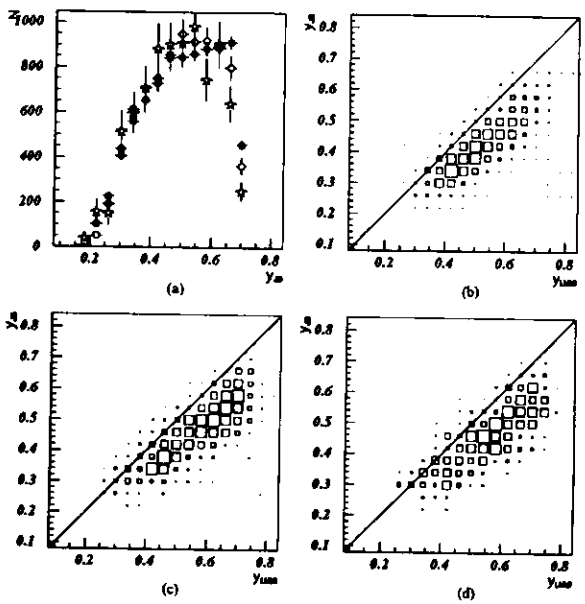

Figure 4.2: y_{JB} and y_{JB} versus y_{LUMI}. The ZEUS data are shown by black dots. The prediction by the PYTHIA non-singlet sample is shown by the open circles and the prediction by the PYTHIA singlet sample is shown by the stars. In (a) the distribution of y_{JB} is shown. One sees the correlation between y_{JB} and y_{LUMI} for the subsample of events in which the scattered e^+ is detected in the e^+ LUMI detector in (b). (c) and (d) for the data, the non-singlet sample and the singlet sample respectively.

Therefore it is appropriate to use the non-singlet sample in understanding the effect of the cleaning cuts on the data.

The vertex distributions are shown in Figures 4.1 and 4.5. The Monte Carlo programs have been tuned to describe these distributions but there is a slight overestimation of the tail to large z values. Also the data are shifted slightly from the nominal x and y values, and this is not described by the

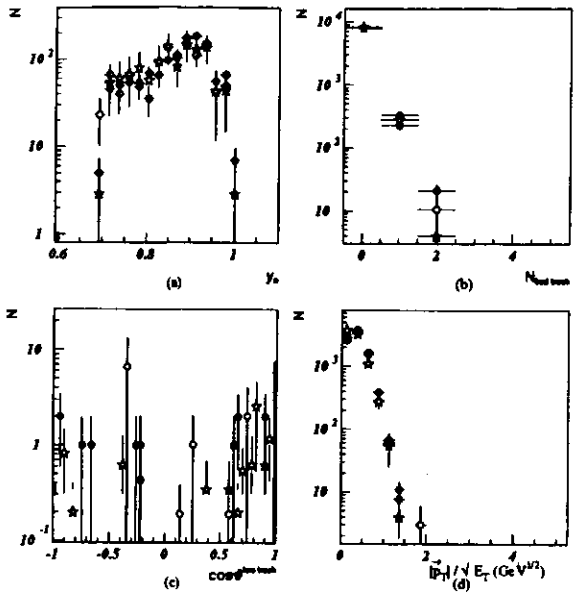

Figure 4.3: Cleaning quantities. The ZEUS data are shown by black dots. The prediction by the PYTHIA non-singlet sample is shown by the open circles and the prediction by the PYTHIA singlet sample is shown by the stars. The distribution of y_e for events with a scattered e^+ candidate in the calorimeter is shown in (a). In (b) one sees the number of rear pointing tracks. In (c) one sees the distribution of the cosine of the opening angle between the two tracks for events which have only two tracks and (d) shows the relative missing transverse momentum, $|\vec{p}_T|/\sqrt{E_T}$.

Monte Carlo samples. These shifts however, do not result in a poor description of the angular distributions of the jets as will be shown in Sect. 4.2.3.

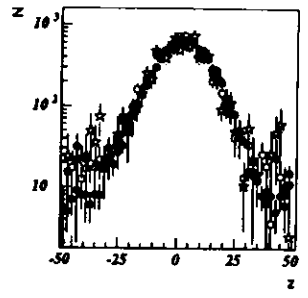

Figure 4.1: The z position of the vertex. The ZEUS data are shown by black dots. The prediction by the PYTHIA non-singlet sample is shown by the open circles and the prediction by the PYTHIA singlet sample is shown by the stars.

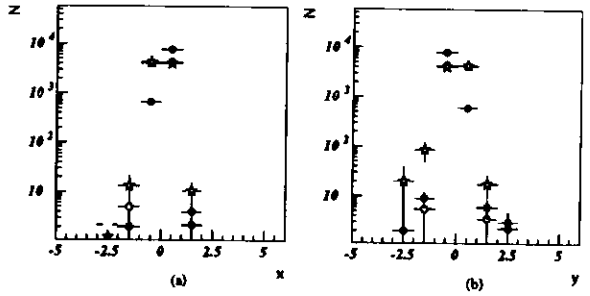

Figure 4.5: The x position of the vertex is shown in (a) and the y position of the vertex is shown in (b). The ZEUS data are shown by black dots. The prediction by the PYTHIA non-singlet sample is shown by the open circles and the prediction by the PYTHIA singlet sample is shown by the stars.

4.2.2 Jet Profiles

The differences between the two Monte Carlo samples and the data are easily visualized with jet profiles. We select the two highest E_T^{jet} jets and the jet at higher η^{jet} is referred to as the leading jet while the jet at lower η^{jet} is called the trailing jet. The jet profile geometry for the trailing jet is illustrated in Figure 4.6. The η profile is made by plotting $\delta\eta^{cell} = \eta^{cell} - \eta^{jet}$, weighted

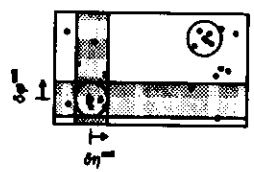

Figure 4.6: Jet profile geometry for the trailing jet. Black dots show the final state particles. The two jets are shown as circles. The vertical and horizontal shaded bands show the regions of the phase space included in the jet profile with respect to $\delta\varphi^{cell}$ and with respect to $\delta\eta^{cell}$ respectively.

by the cell transverse energy, E_T^{cell}, for cells within one radian in φ of the jet centre. Similarly the φ profile is made by plotting $\delta\varphi^{cell} = \varphi^{cell} - \varphi^{jet}$, weighted by the cell transverse energy, for cells within one unit of η of the jet centre.

Figure 4.7 shows the jet profiles for the data in black dots. The jets are highly collimated and the jet pedestal is slowly rising with η. The PYTHIA predictions according to the non-singlet and singlet samples are shown as the solid and dashed histograms respectively. The non-singlet sample describes the data well. There is, however a small discrepancy in the forward direction of $< .5$ GeV per unit $\delta\eta$. This is the aforementioned forward energy discrepancy (we refer to the discussion of Figure 4.1). The jets of the singlet sample are more collimated than the data jets, and they have a lower jet pedestal.

The high degree of collimation of the colour singlet jets is to be expected of course, and there are two reasons for it.

First of all colour singlet exchange events are expected in general to have less radiation into the central rapidity region. This was argued in a general way in terms of gluon bremsstrahlung from accelerated colour charges in Sect. 1.4. With Monte Carlo events it is possible to describe this phenomena precisely, in terms of the Lund string model[1] (in the hard scattering centre of mass frame for simplicity). In colour singlet exchange events each outgoing parton is associated via a Lund string with the remnant jet closest to it in rapidity. Therefore the colour field in the central rapidity region contains little energy for the production of hadrons. However in non-singlet exchange either each parton is connected via a Lund string to the remnant jet which is moving in the opposite direction, or the two partons are connected to each other, and the two remnant jets which are moving opposite to each other in rapidity are connected together. Either way a lot of energy is contained in the colour field in the central rapidity region and there will be considerable radiation of hadrons there.

The second reason that the jets of the singlet sample are expected to be more collimated, is that the singlet sample contains only quark jets in the final state. Gluon jets, which we know at least to be present in the non-singlet sample, give rise to less collimated jets [73].

In Figure 4.8 the profiles are shown just for the $\Delta\eta > 3.5$ subsample of events. The agreement by the non-singlet sample is still good at large $\Delta\eta$. The high degree of collimation of the singlet jets is still apparent.

In Figure 4.9 the profiles are shown for the $\Delta\eta > 3.5$ gap candidate events. By comparing with Figure 4.8 one can clearly see the suppression of energy flow into the rapidity region between the leading and trailing jets. This is well reproduced by the gap-candidates of both the non-singlet and singlet samples.

[1]The argument relies of course, on the dominance of low angle scattering in the t-channel.

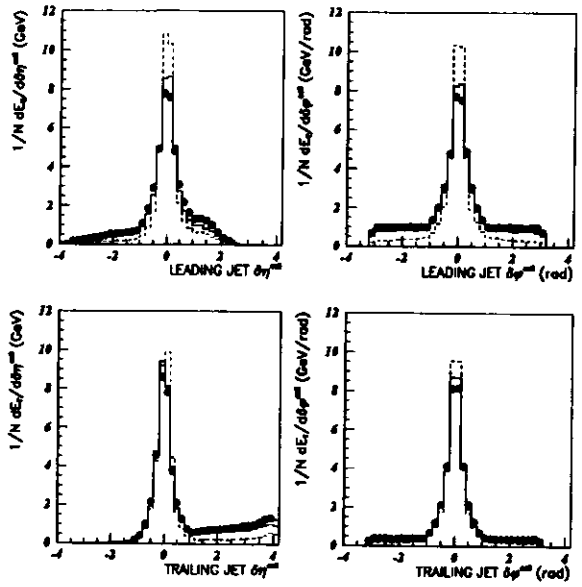

Figure 1.7: Jet profiles for the leading and trailing jets. The data are shown as black dots. The prediction of the PYTHIA sample with no colour singlet exchange (the non-singlet sample) is shown by the solid line. The prediction by the PYTHIA sample with only electroweak quark-quark scattering (the singlet sample) is shown by the dashed line.

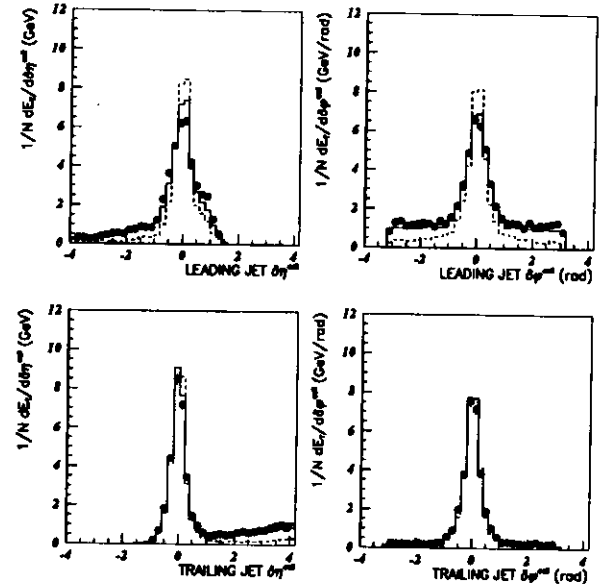

Figure 1.8: Jet profiles for the leading and trailing jets, for the subsample of events with $\Delta\eta > 3.5$. The data are shown as black dots. The predictions of the PYTHIA singlet and non-singlet samples are shown by the solid and dashed lines respectively.

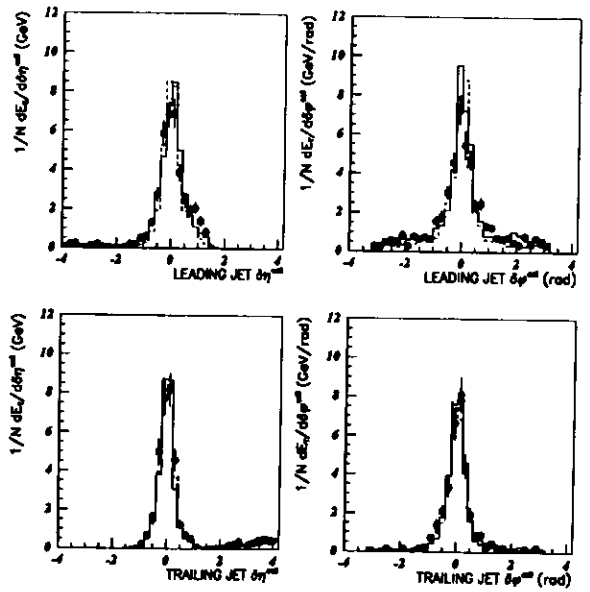

Figure 4.9: Jet profiles for the leading and trailing jets, for the gap candidate events with $\Delta\eta > 3.5$. The data are shown as black dots. The predictions of the PYTHIA singlet and non-singlet samples are shown by the solid and dashed lines respectively.

4.2.3 Jet Angle and Energy

Figure 4.10 shows the η^{jet} and E_T^{jet} distributions of the leading and trailing jets. The leading jet η^{jet} distribution is peaked in the FCAL at $\eta \sim 1.75$ and the trailing jet η^{jet} near the BCAL / RCAL interface at $\eta \sim -0.8$. The non-singlet and singlet samples both have η^{jet} distributions which are

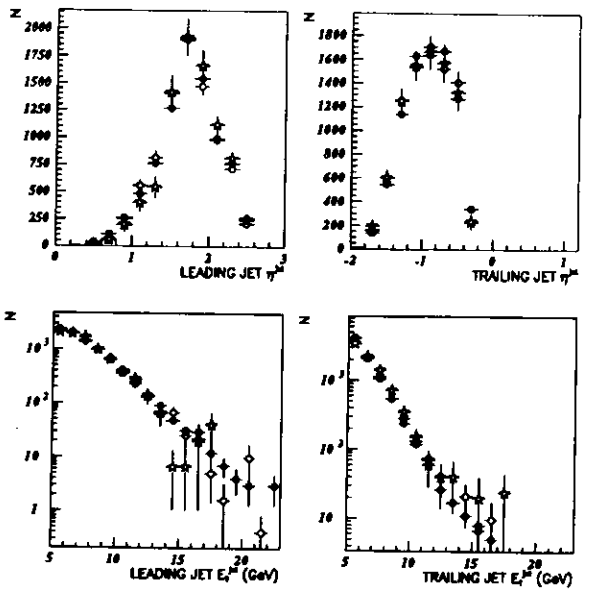

Figure 4.10: The distributions of η^{jet} and E_T^{jet} for the leading and trailing jets. The ZEUS data are shown by black dots. The prediction by the PYTHIA sample with no colour singlet exchange events (the non-singlet sample) is shown by the open circles and the prediction by the PYTHIA sample with only electroweak quark-quark scattering (the singlet sample) is shown by the stars.

very similar to the data. The transverse energy distributions of the leading

and trailing jets fall approximately exponentially from the threshold value. The leading jet E_T^{jet} distribution extends to higher values than the trailing E_T^{jet} distribution. This is due to the higher forward jet pedestal. Both E_T^{jet} distributions are well described by the non-singlet sample. The singlet sample does not agree with the data in the E_T^{jet} distribution. It has relatively higher E_T^{jet} jets.

The E_T^{jet} distributions are shown in four bins of $\Delta\eta$ in Figure 1.11. Particularly for the trailing jet, the E_T^{jet} distribution gets softer as $\Delta\eta$ in-

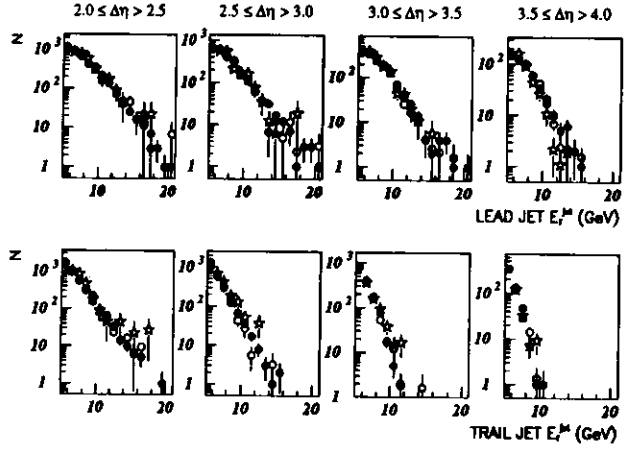

Figure 1.11: The E_T^{jet} distribution of the leading and trailing jets in four bins of $\Delta\eta$. The ZEUS data are shown by black dots. The prediction by the PYTHIA non-singlet sample is shown by the open circles and the prediction by the PYTHIA singlet sample is shown by the stars.

creases. This would enhance the migrations across the $E_T^{jet} > 6$ GeV boundary. Nevertheless this E_T^{jet} behaviour is well described by the non-singlet Monte Carlo sample, so these migrations should be properly accounted for in the corrected distributions.

The boost, or average jet pseudorapidity, $\bar{\eta}$, is shown in Figure 1.12(a). The data are strongly boosted in the proton direction so $\bar{\eta}$ peaks at the kine-

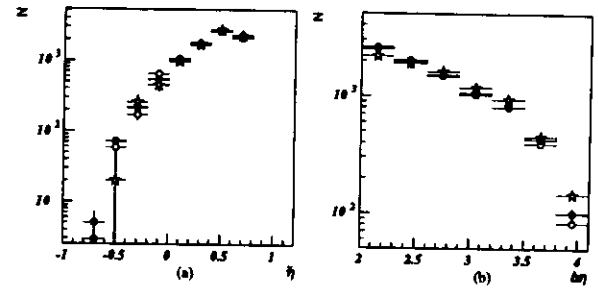

Figure 1.12: The distribution of $\bar{\eta}$ is shown in (a) and the distribution of $\Delta\eta$ is shown in (b). The ZEUS data are shown by black dots. The prediction by the PYTHIA non-singlet sample is shown by the open circles and the prediction by the PYTHIA singlet sample is shown by the stars.

matic limit, $\bar{\eta} = 0.75$. Both Monte Carlo samples describe this distribution.

The $\Delta\eta$ distribution is described by the non-singlet sample as shown in Figure 1.12(b), although there are somewhat too few events at large $\Delta\eta$. (This is partly due to a lack of gap events at large $\Delta\eta$ which is to be discussed in Sect. 5.1.1.) The singlet sample does not provide a good description of the data.

The global event properties are well simulated by the non-singlet Monte Carlo sample. We reiterate that the mixed sample has essentially the same distributions of the global event properties as the non-singlet sample. The narrower jets of the singlet sample show up as significantly different global energy distributions for this sample.

4.2.4 Island Angle and Energy

We have measured the multiplicity of $E_T^{island} > 250$ MeV islands between the jet cones in order to select gap events. We must therefore understand the

E_T^{island} and η^{island} distributions in order to correct for the migrations across the gap definition.

The distribution of the island position with respect to the jet centre for islands with $E_T^{island} > 250$ MeV is shown in Figure 1.13. This is a multiplicity jet profile in contrast to the transverse energy weighted profiles discussed in Section 1.2.2. The multiplicity profiles show the same gradual rise in the

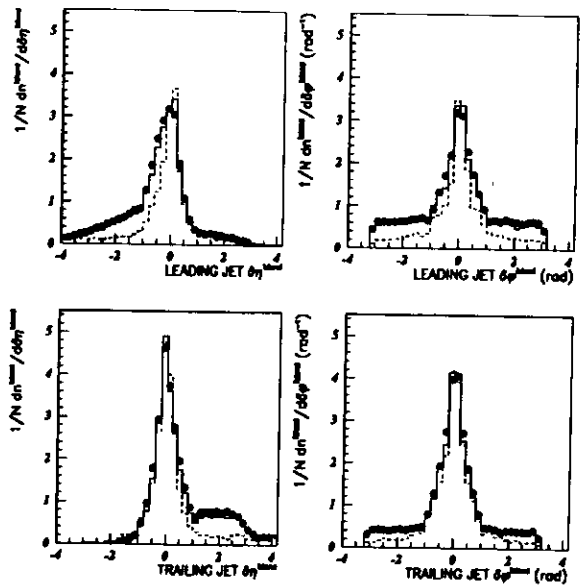

Figure 1.13: The distributions of $\delta\eta^{island}$ and $\delta\varphi^{island}$ with respect to the centres of the leading and trailing jets. The data are shown as black dots. The prediction of the PYTHIA sample with no colour singlet exchange (the non-singlet sample) is shown by the solid line. The prediction by the PYTHIA sample with only electroweak quark-quark scattering (the singlet sample) is shown by the dashed line.

plateau of the jet going from the rear of the detector to the forward region.

Again the non-singlet sample describes the data well although it is slightly more collimated and slightly underestimates the plateau region and again the singlet sample is much more collimated than the data and significantly underestimates the island multiplicity in the plateau region.

The E_T^{island} distribution for the maximum E_T^{island} between the jets is shown in Figure 1.14(a). The PYTHIA sample which contains 10% of colour singlet exchange processes (the mixed sample) is introduced for the first time. It is represented here (and in the following) as the solid line. The data are

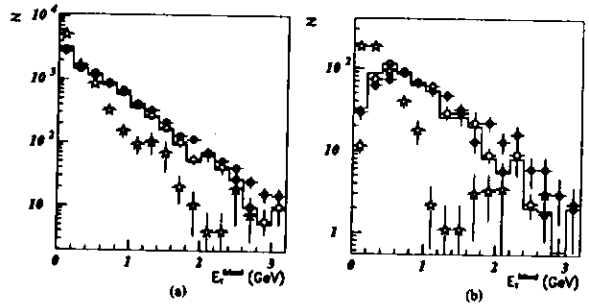

Figure 1.14: The E_T^{island} distribution of the maximum E_T^{island} island between the jets. The ZEUS data are shown by black dots. The prediction by the PYTHIA sample with no colour singlet exchange events (the non-singlet sample) is shown by the open circles and the prediction by the PYTHIA sample with only electroweak quark quark scattering (the singlet sample) is shown by the stars. The prediction by the PYTHIA sample with 10% of electroweak exchange processes (the mixed sample) is shown by the solid line. In (a) the distribution is shown for all events and in (b) the distribution is shown just for the subsample with $\Delta\eta > 3.5$.

exponentially peaked toward[2] $E_T^{island} = 0$ GeV with a tail which extends to $E_T^{island} \sim 1$ GeV. This distribution is well described by the non-singlet sample. The low hadronic activity between the jets of the singlet sample gives rise here to an E_T^{island} distribution which is even more soft.

[2]The noise in the calorimeter can have energies of up to 100 MeV so islands with $E_T^{island} < 100$ MeV can effectively be ignored.

Figure 1.14(b) shows the E_T^{island} distribution for the $\Delta\eta > 3.5$ subsample. Here the agreement between the data and the non-singlet sample at last breaks down. The data have more events at $E_T^{island} \sim 0$ GeV than can be described by the non-singlet sample. The non-singlet E_T^{island} distribution is concentrated at low values of E_T^{island}. This is the first hint we have that there are some colour singlet exchange events in the data. In fact the mixed sample which contains 10% colour singlet exchange events provides the best description of the data at low E_T^{island}.

Of course, another possibility to explain the discrepancy between the non-singlet sample and the data is that the E_T^{island} resolution is incorrectly modelled in MOZART. If, for instance, MOZART underestimates the fluctuations of $E_T^{hadron} > 300$ MeV hadrons into $E_T^{island} < 300$ MeV islands we could obtain the discrepancy shown, with disastrous implications for our understanding of the fluctuations across the gap definition. However, given the good agreement between the non-singlet sample and the data in Figure 1.14(a) this would somehow have to happen preferentially at large $\Delta\eta$.

The CTD provides another indication that the discrepancy in the E_T^{island} distribution is related to a difference in the underlying E_T^{hadron} distributions and not an artifact of the detector. Figures 1.15(a) and (b) show the p_T^{track} distribution over all $\Delta\eta$'s and for $\Delta\eta > 3.5$ respectively. The same general features are observed. In particular, at large $\Delta\eta$ the data have more events at $p_T^{track} \sim 0$ GeV than are modelled in the non-singlet sample. The mixed sample provides a better description there.

In summary, a satisfactory description of the data by the non-singlet and mixed samples has been achieved. The discrepancies occur only in regimes where new physics is expected to appear. We therefore proceed in the next section to estimate efficiencies and resolutions using these samples.

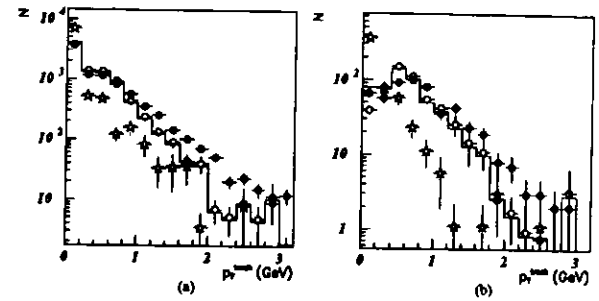

Figure 1.15: The p_T^{track} distribution of the maximum p_T^{track} track between the jets. The ZEUS data are shown by black dots. The prediction by the PYTHIA non-singlet sample is shown by the open circles and the prediction by the PYTHIA singlet sample is shown by the stars. The prediction by the PYTHIA mixed sample is shown by the solid line. In (a) the distribution is shown for all events and in (b) the distribution is shown just for the subsample with $\Delta\eta > 3.5$.

4.3 Efficiency and Resolution

Efficiency is defined here to mean the fraction of the hadron-level events which are reconstructed and accepted as detector-level events. The efficiency of each stage of selection is shown in Figures 1.16 and 1.17 in four bins of the hadron-level $\Delta\eta$. The efficiency according to the mixed sample is shown as black dots and according to the non-singlet sample as open circles. The first column of the figures shows the efficiency for gap events, the second column the efficiency for the inclusive sample. The efficiency of the FLT does not depend on whether or not there is a gap in the event and is better than 85% over the full range of $\Delta\eta$ as shown in the first row of Figure 1.16. The efficiency of the SLT is 100% according to the simulation (not shown). The TLT efficiency is about 85% leading to a cumulative efficiency for the three online triggers which is around 80% as shown in the third row of Figure 1.16. This efficiency is independent of whether or not there is a gap in the final state, and is the same for the mixed and non-singlet samples.

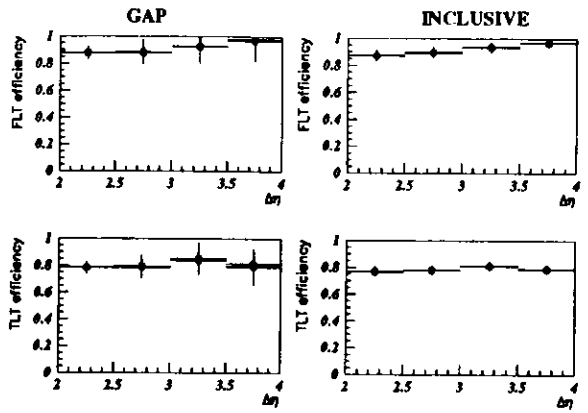

Figure 4.16: The FLT efficiency is shown in the first row and the cumulative trigger efficiency (up to the TLT) is shown in the second row. The efficiency for hadron-level gap events is shown in the left column and the inclusive efficiency is shown in the right column. The efficiencies according to the standard PYTHIA sample (the non-singlet sample) are shown as open circles and the efficiencies according to the PYTHIA sample with 10% colour singlet exchange processes (the mixed sample) are shown as black dots.

The cumulative efficiency up to the offline cleaning cuts is shown in the first row of Figure 4.17. The offline cleaning criteria are greater than 95% efficient and the cumulative efficiency is 75% or better over the range of $\Delta\eta$.

The selection of the calorimeter jets represents the least efficient stage of the selection. It is only about 70% efficient and therefore the cumulative efficiency after the jet-finding is about 40% as shown in the second row of Figure 4.17. This is largely due to the resolution of E_T^{jet} which (as will be shown in Figure 4.18(a)) is 12%. The E_T^{jet} distribution is steeply falling, so there are large migrations both into and out of the selected sample across the E_T^{jet} cut. The cumulative efficiency predictions from the mixed and non-singlet samples are consistent.

Figure 4.18 shows the kinematic resolutions according to the mixed Monte

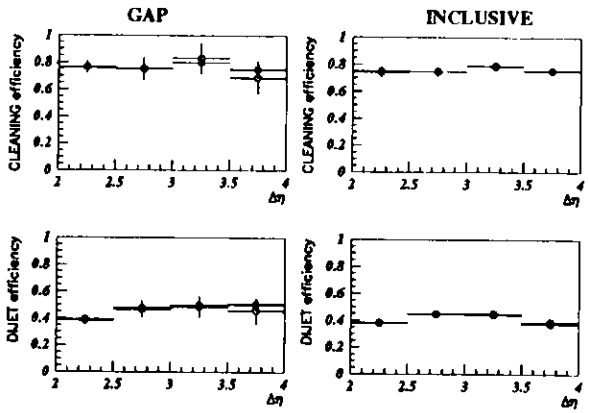

Figure 4.17: The first row shows the cumulative efficiency up to the offline cleaning criteria and the second row shows the cumulative efficiency up to the definition of the reconstructed jets. The efficiency for gap events is shown on the left and the efficiency for the inclusive sample is shown on the right. The non-singlet sample efficiencies are shown as open circles and the mixed sample efficiencies are shown as black dots.

Carlo sample compared with the results of gaussian fits. The resolutions from the non-singlet sample are the same (within the displayed errors). It is because of the shift of -16% in the reconstructed E_T^{jet} value (shown in Figure 4.18(a)) that the minimum E_T^{jet} value is 5 GeV in the selection of events at the detector level as described in Sect. 3.2, as compared to $E_T^{jet} >$ 6 GeV which is the kinematic regime of the cross sections (described at the end of Sect. 1.4 and again in Sect. 5.2). The y resolution is shown in Figure 4.18(b). There is a shift of -20% and therefore the cross-sections are calculated in the range $0.2 < y < 0.85$ while the cut applied to y_{JB} is $0.15 < y_{JB} < 0.7$.

The hadronic energy losses which affect the E_T^{jet} and y_{JB} measurements by the calorimeter occur for several reasons. For instance low p_T charged par-

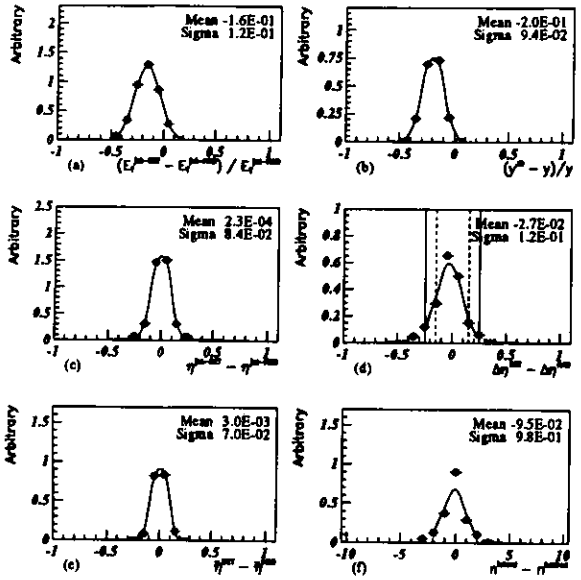

Figure 4.18: Resolutions of the kinematic variables, according to the PYTHIA sample which contains 10% of colour singlet exchange processes (the mixed sample). The resolution of E_T^{jet} is shown in (a), the resolution of y is shown in (b), the resolution of η^{jet} is shown in (c), the resolution of $\Delta\eta$ is shown in (d), the resolution of $\bar{\eta}$ is shown in (e) and the multiplicity resolution is shown in (f). The dashed (solid) vertical lines in (d) show the bin width chosen for the uncorrected (corrected) $\Delta\eta$ distributions.

ticles in a jet of hadrons may be bent by the magnetic field such that they do not reach the calorimeter. Energy losses also occur in uninstrumented material in front of the calorimeter. The energy losses observed in this analysis are consistent with those found in previous studies of hard photoproduction events at HERA [26, 71]

There is negligible shift in the measurement of the jet angular variables,

as shown in Figures 4.18(c),(d) and (e)), so the cut values are the same at the hadronic and calorimeter levels. The bin-widths chosen for the uncorrected and corrected $\Delta\eta$ distributions are shown by the inner and outer vertical lines in Figure 4.18(d) respectively.

The multiplicity resolution is shown in Figure 4.18(f). The number of islands between the jets is well correlated with the number of hadrons, however there will be migrations into and out of the gap sample due to the width of this distribution.

In Figure 4.19(a) we show the resolution of η^{hadron} for the highest transverse energy hadron in the rapidity interval between the jets. (Only events which have a particle between the jets of $E_T^{hadron} > 150$ MeV at both the hadron and detector levels are shown.) This distribution is fit to the sum of

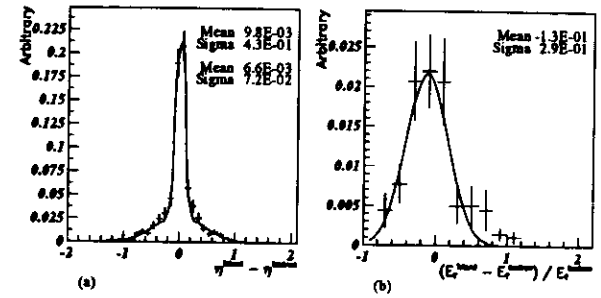

Figure 4.19: The resolution of η^{hadron} according to the PYTHIA mixed sample is shown in (a) and the resolution of E_T^{hadron} according to the PYTHIA mixed sample is shown in (b).

a wide and a narrow gaussian distribution. We assume that the wide gaussian reflects incorrect island-hadron associations and that the true position resolution is given by the width of the narrow gaussian which is about 0.01. For the subsample of these events which have a hadron associated with an island with a position resolution of 0.01 or better the E_T^{hadron} resolution is

shown in Figure 4.19(b). The E_T^{island} threshold is set lower than the E_T^{hadron} threshold to account for the shift in this distribution.

Figure 4.20 shows the η^{hadron} and E_T^{hadron} resolutions for the critical high $\Delta\eta > 3.5$ subsample. These are consistent with the resolutions obtained for the inclusive sample.

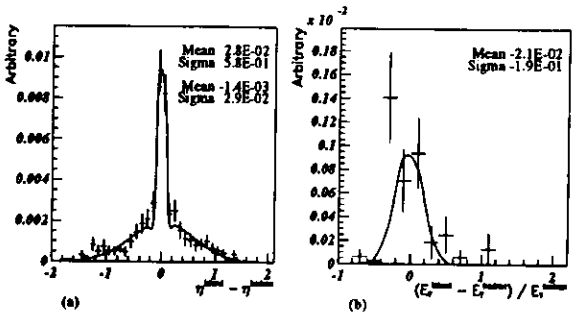

Figure 4.20: Resolution of the island angle and energy according to the mixed Monte Carlo sample for the subsample of events with $\Delta\eta > 3.5$. The η^{hadron} resolution is shown in (a) and the E_T^{hadron} resolution is shown in (b).

In summary the trigger efficiencies are quite high. The worst loss of efficiency occurs in the jet-finding stage of the event selection. However this can be understood in terms of the resolution of the jet angular and energy distributions. All of the measured detector-level quantities are reasonably well correlated with their associated hadron-level quantities.

Chapter 5

Results

Results are obtained in the first section of this chapter by direct comparison of the measured gap-fraction with the detector-level Monte Carlo gap-fraction. In the second section of this chapter the Monte Carlo samples are used to correct the measured gap-fraction for detector effects to obtain a hadron-level measurement.

5.1 Results from Uncorrected Data

The results from the uncorrected data distributions can be obtained from the gap-fraction or directly from the multiplicity distributions.

5.1.1 Multiplicity

We first examine the island multiplicity which is used to define the gap events. The number of islands in the rapidity interval between the jet cones which have $E_T^{island} > 250$ MeV is shown in Figure 5.1 in four bins of $\Delta\eta$. The data are shown as black dots, the open circles represent the non-singlet sample, and the stars show the singlet sample, as in previous chapters. The mixed Monte Carlo sample is shown as the line histogram.

The average multiplicity increases with $\Delta\eta$ but there is still a large number of events in the data with zero multiplicity at $\Delta\eta > 3.5$. The Monte

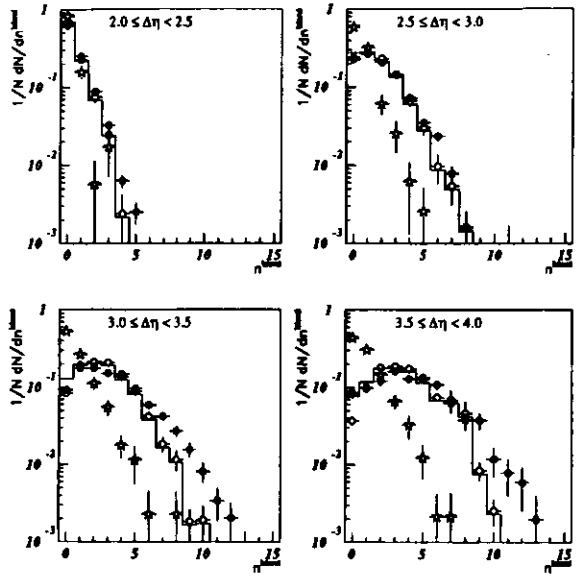

Figure 5.1: The island multiplicity distributions in four bins of $\Delta\eta$. The data are shown as black dots. The prediction by the PYTHIA events with no colour singlet exchange (the non-singlet sample) is shown by open circles and the prediction by the PYTHIA sample which contains only electroweak quark quark scattering (the singlet sample) is shown by stars. The solid line shows the prediction of the PYTHIA events with 10% of colour singlet exchange processes (the mixed sample).

Carlo samples fail to describe the data. No model can reproduce the tail to large multiplicity. This effect might be accounted for by radiation from the propagator which is not simulated in the Monte Carlo [41, 75, 76], or by the aforementioned multiple interaction processes which are also not simulated in these samples.

In addition, the non-singlet sample shows too few $n^{island} = 0$ events at

$\Delta\eta > 3.5$. An addition of 10% colour singlet events is able to describe this low end of the multiplicity distribution as shown by the mixed sample[1]. However the mixed sample overestimates the number of $n^{island} = 0$ events with $3.0 \leq \Delta\eta < 3.5$. These electroweak exchange quark quark scattering processes with no simulation of multiple interactions are clearly not the perfect model for the colour singlet processes of the data. This mixed sample will therefore only be used to get a rough estimate of the percentage of colour singlet exchange processes in the data. Its most important use is in estimating the effects of detector smearing to be discussed in Sect. 5.2.2.

We check the observation from the island multiplicity that about 10% of colour singlet exchange processes occur in the data by looking at the charged particle multiplicity. Figure 5.2 shows the multiplicity of CTD tracks with $p_T > 250$ MeV. These distributions also indicate the need for some colour singlet process in order to describe the number of low multiplicity events at large $\Delta\eta$ in the data.

In summary the multiplicity distributions can be interpreted as indicating that the data contain colour singlet exchange processes at a rate of about 10%.

5.1.2 Gap-Fraction

The distribution of the number of gap events as a function of $\Delta\eta$ is shown in Figure 5.3(a). Here as throughout the solid dots represent ZEUS data, the open circles the non-singlet Monte Carlo sample, the stars represent the singlet Monte Carlo sample and the line shows the mixed sample. The Monte Carlo distributions are normalized to the total number of events (independent of whether there is a gap or not) in the data. The number of events in the data exhibiting a gap falls steeply with $\Delta\eta$. However the expectation

[1] This observation is of course related to the data having more events where the E_T^{island} of the maximum E_T^{island} island is low. It is worth reiterating that the threshold of $E_T^{island} > 250$ MeV which is used in determining the island multiplicity is well motivated theoretically [36, 37, 48, 49].

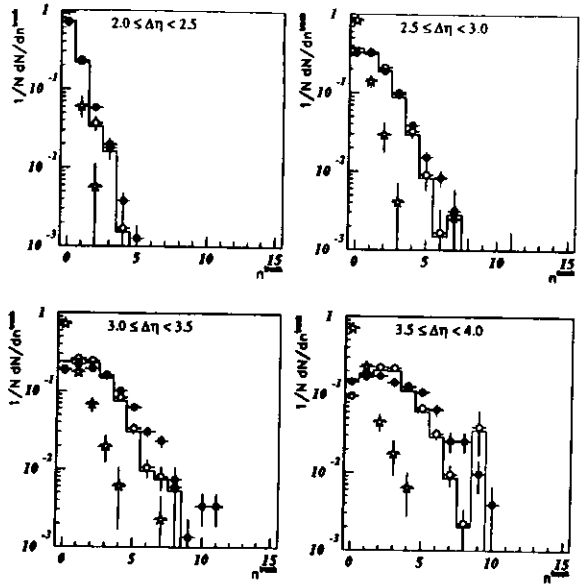

Figure 5.2: The charged multiplicity distributions in four bins of $\Delta\eta$. The data are shown as black dots. The prediction by the PYTHIA non-singlet sample is shown by open circles and the prediction by the PYTHIA singlet sample is shown by stars. The solid line shows the prediction of the PYTHIA mixed sample.

from the PYTHIA non-singlet sample falls more steeply than the data, significantly underestimating the number of gap events at large $\Delta\eta$. The PYTHIA sample with a mixture of 10% of electroweak boson exchange can account for the number of gap events in the data at large $\Delta\eta$. However this sample significantly overestimates the number of gap events at low $\Delta\eta$. These are essentially the same observations which have been made from the n^{island} and E_T^{island} distributions.

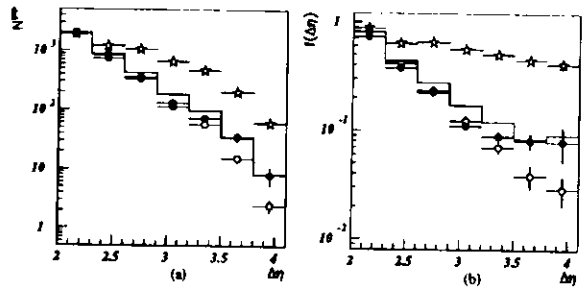

Figure 5.3: The uncorrected $\Delta\eta$ distribution for gap candidates is shown in (a) and (b) shows the uncorrected gap-fraction. The data are shown as black dots. The prediction by the PYTHIA non-singlet sample is shown by open circles and the prediction by the PYTHIA singlet sample is shown by stars. The solid line shows the prediction of the PYTHIA mixed sample.

By taking the ratio of Figure 5.3(a) to Figure 4.12(b), the gap-fraction shown in Figure 5.3(b) is obtained. The gap-fraction falls exponentially out to $\Delta\eta \sim 3.2$. Thereafter it levels off at a value of roughly 0.08. Thus the uncorrected gap-fraction exhibits the two component behaviour which is expected to indicate the presence of colour singlet exchange processes as described in Sect. 1.4. In the region of the exponential fall, $2 \leq \Delta\eta < 3.2$, the data are quite well described by the non-singlet sample. It is expected that at low $\Delta\eta$ the dominant contribution to the gap-fraction is from multiplicity fluctuations in non-singlet events and this expectation is supported by the reasonably good description of the gap-fraction for $\Delta\eta < 2.6$ by the non-singlet sample. However the non-singlet sample does slightly overestimate the fraction of gap events here. It is expected that some addition of multiple interaction events into the non-singlet simulation would account for this discrepancy. In the plateau region of the gap-fraction, $\Delta\eta > 3.2$, it is expected that the dominant mechanism for gap production is from colour singlet exchange processes. This expectation is borne out by the behaviour

of the singlet sample, which exhibits a relatively flat gap-fraction, and by the mixed sample, which can describe the plateau of the data. In contrast the non-singlet sample fails to describe the flat region in the data, falling approximately exponentially over the whole measured range of $\Delta\eta$.

The mixed sample overestimates the gap-fraction particularly in the intermediate region $2.6 \leq \Delta\eta < 3.2$. Recall that we are aware of two possible shortcomings of this simulation. The first is the absence of multiple interactions and the second is the absence of any gluon jets. Either of these effects could explain the discrepancy at intermediate $\Delta\eta$.

The observation of an excess in the uncorrected gap-fraction, over the predicted gap-fraction in the non-singlet sample, is important as it suggests that gaps are being produced in the data by mechanisms other than what is simulated by the standard Monte Carlo events. It is imperative to assure that this distribution has not arisen due to some unexpected behaviour of the detector. In the following, three uncorrected gap-fractions (measured in four $\Delta\eta$ bins) are shown which have increased our confidence in the observed excess.

Figures 5.4(a) and (b) show the N^{ev} distribution and the gap-fraction (respectively) resulting from using the charged multiplicity to define a gap. A gap event is then defined has having *no* tracks of $p_T^{track} > 250$ MeV in the rapidity interval between the jets. The gap-fraction does also show a deviation from an exponential fall although it is more difficult to see this here since the gap-fraction obtained when one ignores neutral particles between the jets is quite high over the entire $\Delta\eta$ range. One also sees the excess of gaps in the data at large $\Delta\eta$ over the expectation from standard PYTHIA processes.

As previously shown in Figure 1.18(f), smearing of the multiplicity reconstruction can allow fluctuations of about one particle into and out of the rapidity interval. We present in Figure 5.5 the raw results where a gap has been defined as ≤ 1 island. There is very little smearing across this gap definition. (We have lowered the E_T^{island} threshold to 200 MeV because otherwise the number of gap events is too high to see any structure in the gap-fraction.) The gap-fractions are quite high throughout the $\Delta\eta$ range, but one can still see an excess in the data over the expectation from the standard PYTHIA

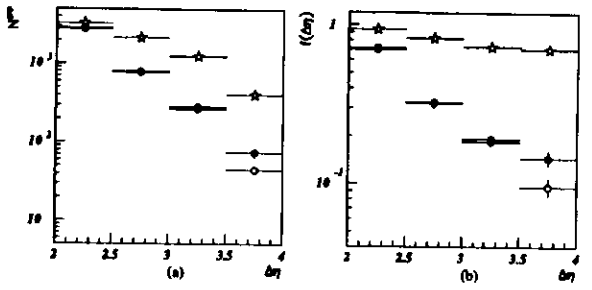

Figure 5.4: The $\Delta\eta$ distribution for gap events where a gap is defined as no tracks with $p_T^{track} > 250$ MeV is shown in (a). The corresponding gap-fraction is shown in (b). The data are shown as black dots. The prediction by the PYTHIA non-singlet sample is shown by open circles and the prediction by the PYTHIA singlet sample is shown by stars.

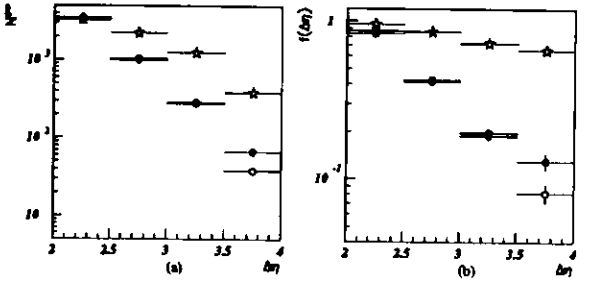

Figure 5.5: The $\Delta\eta$ distribution for gap events where a gap is defined as ≤ 1 island with $E_T^{island} > 200$ MeV is shown in (a). The corresponding gap-fraction is shown in (b). The data are shown as black dots. The prediction by the PYTHIA non-singlet sample is shown by open circles and the prediction by the PYTHIA singlet sample is shown by stars.

non-singlet sample.

The corresponding results from defining a gap as ≤ 1 charged track are shown in Figure 5.6. Here one also sees that standard PYTHIA events underestimate the fraction of gap events at large $\Delta\eta$.

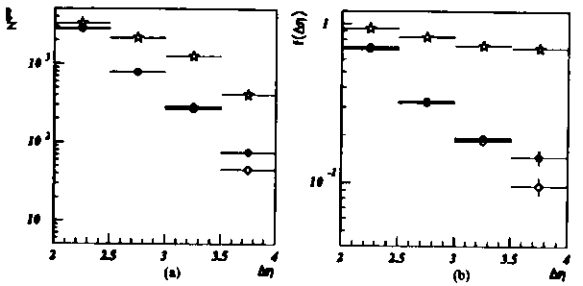

Figure 5.6: The $\Delta\eta$ distribution for gap events where a gap is defined as ≤ 1 track with $E_T^{track} > 200$ MeV is shown in (a). The corresponding gap-fraction is shown in (b). The data are shown as black dots. The prediction by the PYTHIA non-singlet sample is shown by open circles and the prediction by the PYTHIA singlet sample is shown by stars.

These distributions confirm that the excess of gap events at large $\Delta\eta$ in the data as compared to the Monte Carlo events is not due to a misunderstanding of the calorimeter performance.

5.1.3 Summary of Uncorrected Results

The uncorrected gap-fraction exhibits a two component behaviour, an exponential fall at low $\Delta\eta$ and a plateau at high $\Delta\eta$. It also indicates that there is an excess fraction of gap events at $\Delta\eta > 3.2$ over the prediction from standard QCD processes. These two observations indicate a need for colour singlet exchange processes in the data at a level of about 10%. We wish to also make some interpretation of the data without reference to a particular Monte Carlo model. Also, we wish to ascertain whether the two

component behaviour of the gap-fraction could be an artifact of the detector smearing and acceptance. Therefore we must correct the data for the detector response.

Figure 5.7 gives an idea of the size of the detector corrections. In Figure 5.7 asterixes are used to show the gap-fraction in the Monte Carlo simulations at the hadron-level, before any detector smearing. Figure 5.7(a)

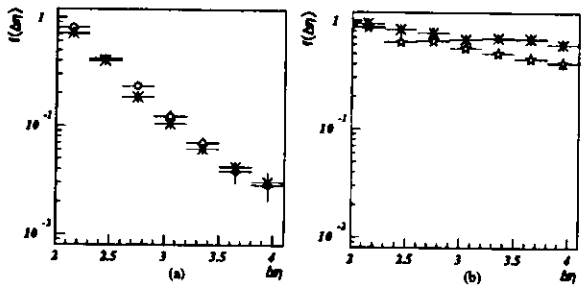

Figure 5.7: Gap-fractions at the detector and hadron levels. In (a) the gap-fraction of the non-singlet sample is shown at the detector-level by open circles and at the hadron-level by asterixes. In (b) the gap-fraction of the singlet sample is shown. The detector-level gap-fraction is shown by stars and the hadron-level gap-fraction is shown by asterixes.

shows the gap-fraction in the non-singlet model. Here no significant detector effect is apparent, since the hadron-level and detector-level gap-fractions are in agreement (within the statistical errors). We therefore feel that the plateau in the uncorrected gap-fraction can not arise as a detector effect on an original hadron-level exponential distribution. Figure 5.7(a) shows that the detector does not have a large effect on an exponentially suppressed gap-fraction. However Figure 5.7(b) shows that the gap-fraction for the pure singlet sample is affected by the detector. Overall the detector tends to lower the fraction of gap events. Therefore, in order to make a quantitative interpretation of the plateau in the gap-fraction, corrections for the detector response must be made. This is undertaken in the following section.

5.2 Results from Corrected Data

The mixed and non-singlet Monte Carlo samples have been used to correct the data for all detector effects, including acceptance, smearing and the shift in the measurement of energies, in order to obtain a quantitative estimate of the amount of colour singlet exchange processes in the data. Cross sections are determined and a gap-fraction is measured in four bins of $\Delta\eta$ in the range $2 \leq \Delta\eta < 4$.

The cross section $d\sigma/d\Delta\eta$ for dijet photoproduction, $ep \to e\gamma p \to eX$, where X contains at least two jets of final state particles is measured in the range $0.2 < y < 0.85$ for photon virtualities $P^2 < 1$ GeV^2. The two jets are defined by a cone algorithm with a cone radius of 1.0 in $\eta - \varphi$ and satisfy $E_T^{jet} > 6$ GeV and $\eta^{jet} < 2.5$. The two jets of highest E_T^{jet} satisfy $\Delta\eta > 2$ and $|\bar{\eta}| < 0.75$. The gap cross section, $d\sigma_{gap}/d\Delta\eta$, is measured in the same kinematic range, where a gap event has *no* final state particles with transverse energy $E_T^{hadron} > 300$ MeV between the jet cones. The corrected gap-fraction $f(\Delta\eta)$ is then obtained from the ratio of $d\sigma_{gap}/d\Delta\eta$ to $d\sigma/d\Delta\eta$.

5.2.1 Correction Method

The corrected cross sections have been obtained by a bin-by-bin correction method according to,

$$d\sigma/d\Delta\eta = N(\Delta\eta) \cdot C(\Delta\eta) \cdot \mathcal{L}^{INT} \cdot 2 \qquad (5.1)$$

where $N(\Delta\eta)$ is the number of events measured in a $\Delta\eta$ bin, $C(\Delta\eta)$ is the correction factor, the ratio of the hadron-level to detector-level Monte Carlo cross section in the $\Delta\eta$ bin, $\mathcal{L}^{INT}$ is the integrated luminosity used and the factor of 2 comes from dividing by the bin-width.

The correction factors determined from the mixed (non-singlet) sample are shown in Figure 5.8 as black dots (open circles). The correction factors vary smoothly between 1.6 and 1.3 and are not different for the two Monte

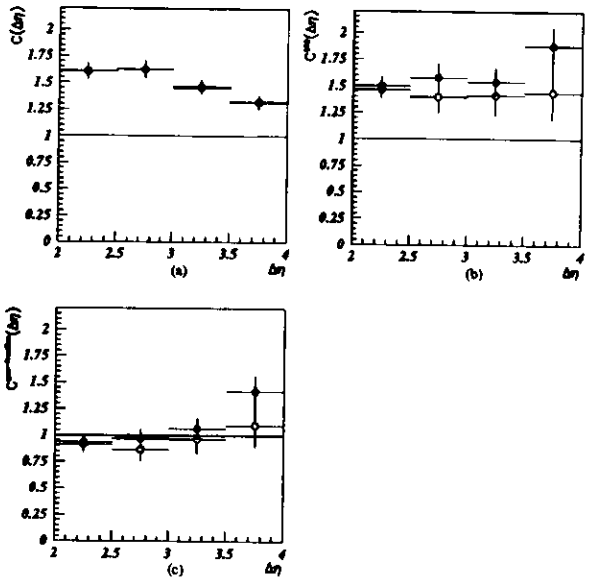

Figure 5.8: The correction factors for the inclusive cross section are shown in (a) and the correction factors for the gap cross section are shown in (b). (c) shows the effective correction factors for the gap-fraction. The correction factors according to the standard PYTHIA sample (the non-singlet sample) are shown as open circles and the correction factors according to the PYTHIA sample with 10% colour singlet exchange processes (the mixed sample) are shown as black dots.

Carlo samples. The correction factors for the gap distribution are shown in Figure 5.8(b) and are around 1.5. Here some difference between the two samples can be seen with the mixed sample yielding higher correction factors than the non-singlet sample. (This will be further discussed in the following.) Effective correction factors for the gap-fraction are shown in Figure 5.8(c). The corrections largely cancel in this ratio. This suggests that they are

primarily due to the selection and reconstruction of the jets and that the jets are similar in gap and non-gap events.

The correction factors are equivalently, the ratio of the bin-purity to the bin-efficiency. The bin-purity is defined as the fraction of detector-level events in a bin which are also hadron-level events in that bin. The bin-efficiency is the fraction of hadron-level events in a bin which are also detector-level events in that bin. Figure 5.9 shows the bin-efficiency and bin-purity as obtained from the mixed sample in black dots and from the non-singlet sample in open circles. The bin-efficiencies for the inclusive sample are 21% or higher

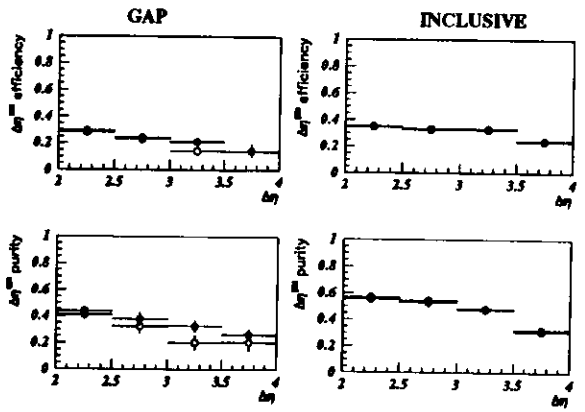

Figure 5.9: The bin-efficiencies are shown in the first row and the bin-purities are shown in the second row. The first column shows the subsample of events which are hadron-level gap events and the second column shows the inclusive sample of events. The non-singlet PYTHIA sample is shown by the open circles and the mixed PYTHIA sample is shown by the black dots.

according to both the mixed and non-singlet samples. The bin-efficiencies for the gap events are 15% or higher according to both the mixed and non-singlet samples. The bin-purities are 31% or higher for the inclusive events

according to both the mixed and non-singlet Monte Carlo samples. The bin-purities for the gap events are 26% or higher according to the mixed sample, and 21% or higher according to the non-singlet sample.

The bin-purities and bin-efficiencies for the inclusive events are the same whether the mixed or non-singlet sample is used to obtain them. However the bin-purities and bin-efficiencies of the gap events are somewhat different depending upon which sample is used. This gives rise to the difference in the correction factors we saw in Figures 5.8(b) and (c). The bin-purities and bin-efficiencies of the gap events are also lower than the corresponding bin-purities and bin-efficiencies of the inclusive sample of events. This arises due to migrations across the gap definition. These are investigated further in the following.

By restricting to events which are accepted at both the hadron-level and the detector-level, and by considering only those events which in addition are reconstructed with a detector-level $\Delta\eta$ which lies in the same bin as the hadron-level $\Delta\eta$, one can study the bin-efficiency and bin-purity which is due to migrations across the gap definition alone. These are called the gap incremental bin-efficiency and bin-purity and are shown in Figure 5.10. The gap incremental bin-efficiency is 15% or better and the bin-purity is

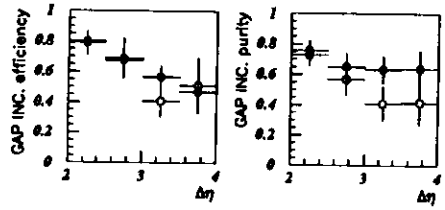

Figure 5.10: The gap incremental bin-efficiency is shown on the left and the gap incremental bin-purity is shown in the right. The non-singlet PYTHIA sample is shown by the open circles and the mixed PYTHIA sample is shown by the black dots.

better than 60% according to the mixed Monte Carlo sample. The non-

singlet sample gives consistent efficiencies, but somewhat lower purities at large $\Delta\eta$. This reduction of bin-efficiency and bin-purity for gap events is due to the finite resolution[2] of E_T^{hadron} for events which have a low transverse energy particle between the jet cones and to the finite resolution of η^{hadron} for events which have a particle near the edge of one of the jet cones. This may be illustrated by varying the cuts on E_T^{island} and η^{island}.

For instance, Figure 5.11 shows the gap incremental bin-efficiencies and bin-purities for a "loose" gap definition. Here the detector-level gap definition has been changed to *no* islands of $E_T^{island} > 300$ MeV in a rapidity interval which begins 0.1 units of η from the jet cones (i.e. in a smaller rapidity interval than that defined by the jet cones). For the "loose" gap definition

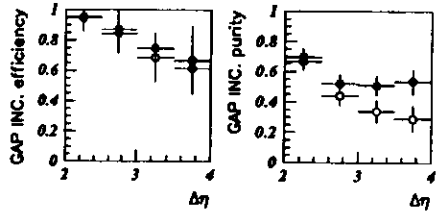

Figure 5.11: Gap efficiency and purity for a "loose" gap definition. The incremental bin-efficiency is shown on the left and the incremental bin-purity is shown in the right. The non-singlet PYTHIA sample is shown by the open circles and the mixed PYTHIA sample is shown by the black dots.

the efficiency is high, as one would expect, but there is a corresponding loss of purity.

Figure 5.12 shows the gap efficiency and purity for a "tight" gap definition. Here the gap requirement is *no* islands of $E_T^{island} > 200$ MeV in a rapidity interval which begins 0.1 units of η within the jet cones. As expected, the purity is high for this gap definition although there is a loss of efficiency.

[2]These resolutions were shown in Sect. 4.3.

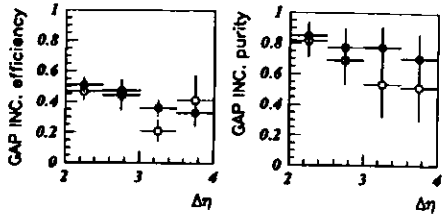

Figure 5.12: Gap efficiency and purity for a "tight" gap definition. The incremental bin-efficiency is shown on the left and the incremental bin-purity is shown in the right. The non-singlet PYTHIA sample is shown by the open circles and the mixed PYTHIA sample is shown by the black dots.

We assign a systematic uncertainty to the gap-fraction associated with the E_T^{island} and η^{island} resolutions by varying the E_T^{island} and η^{island} cuts which define a gap and by correcting with both the mixed and non-singlet samples (see Sect. 5.2.2). This systematic uncertainty is of the order of the statistical error. In future measurements with better statistics at large $\Delta\eta$ it will be important to improve these resolutions.

Another feature of Figure 5.9 is that the bin-efficiency and bin-purity of the inclusive sample degrade with increasing $\Delta\eta$ due to smearing across the $\Delta\eta$ bins. This can be seen from Figure 5.13 which shows the resolutions of the kinematic variables as a function of $\Delta\eta$. The dot shows the shift of the centre of a gaussian fit to the resolution and the error bar shows the width of the gaussian. (Here the mixed sample is shown but the non-singlet sample yields almost identical resolutions.) None of the resolutions show a strong dependence on $\Delta\eta$. However the small shift in the resolution of $\Delta\eta$ which increases with $\Delta\eta$ can cause particular problems since we wish to correct a cross section which is differential in $\Delta\eta$. The bin widths for the raw and corrected $\Delta\eta$ distributions are indicated on Figure 5.13(d) by the dashed and solid lines respectively. We have corrected for this $\Delta\eta$ smearing using an unfolding algorithm based on Bayes' theorem [77]. The details of

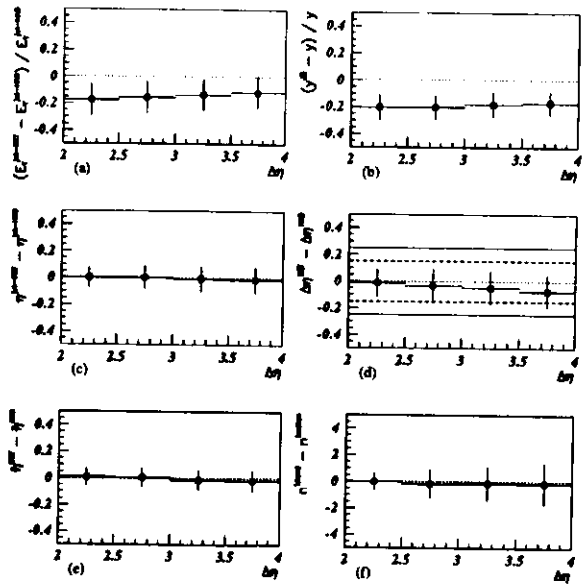

Figure 5.13: Resolution versus $\Delta\eta$. The black dot shows the shift and the error bars show the width.

this correction method are described in Appendix D. The results are not significantly different, as will be shown in Sect. 5.2.2.

5.2.2 Systematic Uncertainty

To investigate the systematic uncertainty of the measurement we have corrected the data in seventeen different ways. The corrected data points are the averaged results of these seventeen methods. The inclusive cross section, the gap cross section and the gap-fraction computed in the seventeen different ways are shown in Figures 5.11, 5.15 and 5.16 respectively.

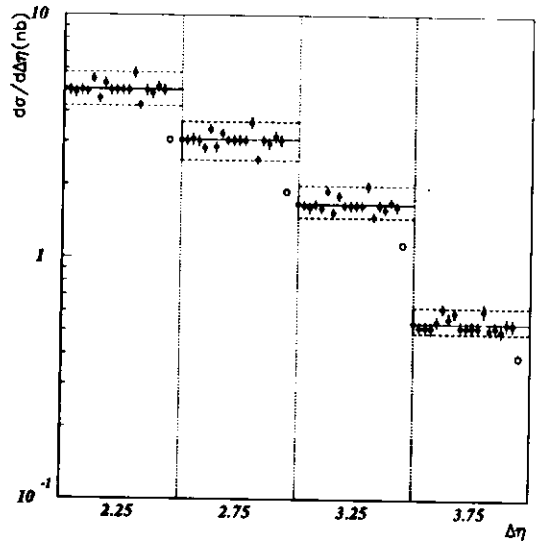

Figure 5.14: The inclusive cross section computed in seventeen different ways (see text) is shown by the black dots and the white dots show the distribution before the detector corrections for comparison.

The left-most set of points (and the solid line horizontally across each bin) shows the mean of all of the systematic variations. The next point shows the "central" correction which is made using the selection exactly as described in Chapter 3 and the mixed Monte Carlo sample. The mixed Monte Carlo sample is chosen for the central correction because it is the best description that we have of the large $\Delta\eta$ multiplicity distribution. The error bars on this point (and the rest of the black dots too) come from the propagation of data and Monte Carlo statistical errors. This is the statistical error of the final result. The outer error bars of the final result are obtained by adding the statistical errors in quadrature with the largest systematic

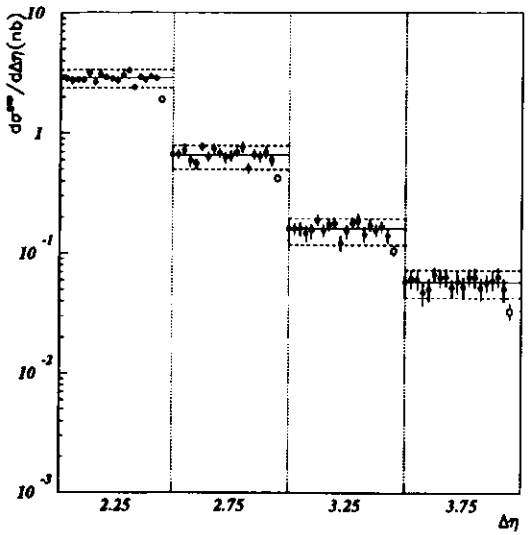

Figure 5.15: The gap cross section computed in seventeen different ways (see text) is shown by the black dots and the white dots show the distribution before the detector corrections for comparison.

deviation (separately for the upward and downward uncertainties) in each bin. They are illustrated here by the dashed horizontal lines. The next sixteen points show the systematic variations.

That is, from left to right the black dots represent:

1. The mean of all the systematic variations.

2. The central correction.

3. Leaving out the LO direct events from the non-singlet PYTHIA sample.

   The fraction of LO direct processes is not well known and LO direct events do have somewhat different resolutions from LO resolved events. We estimate

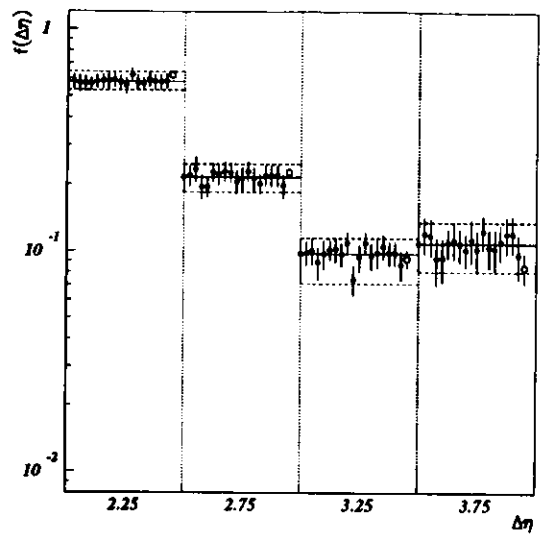

Figure 5.16: The gap-fraction computed in seventeen different ways (see text) is shown by the black dots and the white dots show the gap-fraction before the detector corrections for comparison.

the size of the uncertainty due to the mixing of LO direct processes with this systematic variation. It leads to no significant effect.

4. Correcting using the non-singlet PYTHIA sample.

   The non-singlet and mixed samples have different incremental gap bin-efficiencies and bin-purities as described in Sect. 5.2.1. This systematic variation shows that their uncertainty has only a small effect.

5. Changing the proton and photon parton distributions.

   In this systematic variation the photon parton distribution is changed to LAC1 [19] and the proton parton distribution is changed to GRV [78]. There is a noticeable effect on the cross sections but it cancels in the gap fraction.

6. Lowering the E_T^{jet} cut to 1.5 GeV.

7. Raising the η^{jet} forward cut to 3.

8. Changing the y_{JB} range to between 0.2 and 0.8.

   These three systematic variations allow for fluctuations of background into the sample from outside the kinematic range of interest. They yield about the same deviation in each bin of $\Delta\eta$ and largely cancel in the gap-fraction.

9. Changing the E_T^{island} threshold to 300 MeV.

10. Changing the E_T^{island} threshold to 200 MeV.

11. Changing the effective cone radius to 0.9.

12. Changing the effective cone radius to 1.1.

    These four systematics allow for migrations across the E_T^{island} and η^{island} cuts in events that do have a particle in or near the gap region and form the largest systematic uncertainty of the gap-fraction.

13. Lowering the calorimeter energy scale by 5 percent.

14. Suppressing "noisy" calorimeter cells in the data.

    The calorimeter energy scale is known to within 5% for hard photoproduction events [74]. These two systematics account for the extent to which we understand the calibration of the calorimeter, and the simulation of noise in it. They form the largest systematic uncertainty of the two cross sections but cancel in the gap-fraction.

15. Using an alternate "island" algorithm.

    The ISLAND algorithm clusters cells based on the relative E_T^{cell} of neighbouring cells. To investigate the systematic uncertainty due to this algorithm we have used an alternate clustering algorithm in which all cells which are within $r = \sqrt{\delta\eta_{cell}^2 + \delta\varphi_{cell}^2}$ of 0.2 of one another are joined. This obviously does not affect the inclusive cross section and the effect on the gap cross section and gap-fraction is small.

16. Raising the integrated luminosity by 3.3%.

17. Lowering the integrated luminosity by 3.3%.

    This small systematic uncertainty on the cross sections from the measurement of the integrated luminosity cancels of course in the gap fraction.

18. Unfolding for $\Delta\eta$ migrations using an algorithm based upon Bayes theorem.

    This is an important systematic given the reasonably large $\Delta\eta$ migrations as discussed in Sect. 5.2.1. The details of this unfolding method are presented in Appendix D. The unfolding procedure yields cross sections which are consistent with those obtained from the bin-by-bin correction method.

For comparison, the uncorrected data are shown in Figures 5.14, 5.15 and 5.16 as open circles. Thus one can see that both of the cross sections are significantly raised by the correction procedure, but the corrections do not significantly alter the gap-fraction.

The analysis has been repeated independently for some of the systematic variations. Figure 5.17 shows the comparison of the corrected cross sections and the gap-fraction for the two analyses. The black dots show the results from the first analysis and the open circles show the results from the second analysis. Shown here is the systematic variation 1, for correction using the non-singlet sample. The differences between the two analyses lie mainly in the event selection procedure. The second analysis used a different algorithm for finding the scattered e^+ candidate in the rejection of DIS background. The p beam gas rejection is also done differently. The second analysis made use of the ratio of the number of CTD tracks which point to the vertex to the number of CTD tracks which do not point to the vertex while the first analysis used the number of rear-pointing tracks. An excellent agreement between the two analyses is obtained.

The systematic checks 5 and 14 were actually performed by the second analysis. This means that the systematic check of correcting with the non-singlet sample is actually weighted by 3 with respect to the other systematic checks. This arose simply out of convenience but we feel that it is sensible

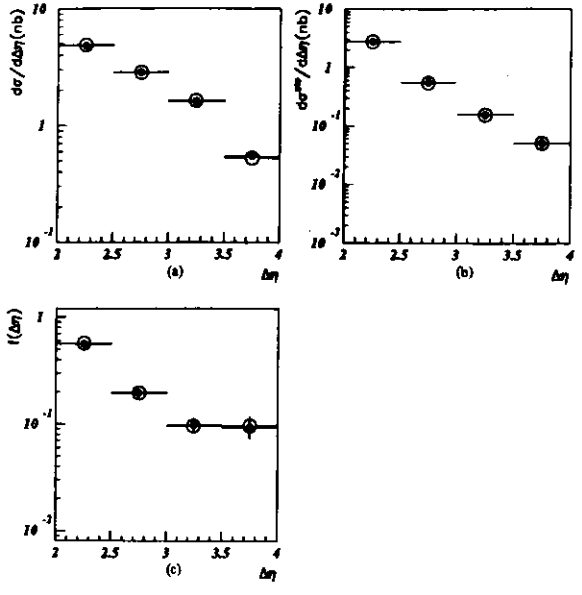

Figure 5.17: The corrected inclusive and gap cross sections and the corrected gap-fraction are shown in (a), (b) and (c) respectively. The non-singlet PYTHIA sample was used in obtaining the correction factors. The results from the first analysis are shown as black dots and the results from the second analysis are shown as open circles.

anyway to weight this systematic more heavily; although the mixed sample provides the best description of the data at large $\Delta\eta$, the non-singlet sample does describe the data better at intermediate $\Delta\eta$.

5.2.3 Summary of Corrected Results

The results after detector corrections are shown in Figure 5.18. The inner error bars show the statistical errors and the outer error bars show the systematic uncertainties, added in quadrature. (In some cases it is not possible to see the ends of the inner (statistical) error bar because it is within the black dot marker.) The cross section points are plotted at the centres of the bins. The gap-fraction points are plotted at the mean $\Delta\eta$ values of the inclusive cross section.

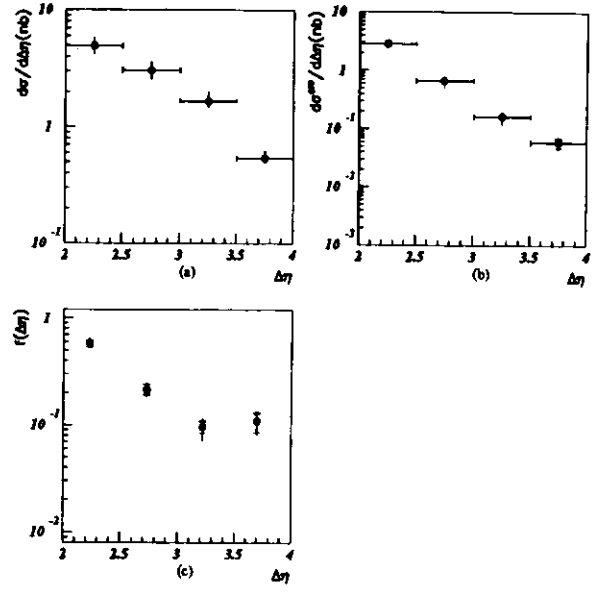

Figure 5.18: The cross section $d\sigma/d\Delta\eta$ is shown in (a). The gap cross section $d\sigma^{gap}/d\Delta\eta$ is shown in (b) and the gap-fraction, $f(\Delta\eta)$, is shown in (c). The corrected ZEUS data are shown as black dots. The inner error bars show the statistical errors (in some cases within the marker) and the outer error bars show the systematic uncertainties.

The corrected gap-fraction falls exponentially in the first three bins but the height of the fourth bin is consistent with the height of the third. The

height of the fourth bin is $0.11 \pm 0.02(stat.)^{+0.01}_{-0.02}(sys.)$, which is also consistent with the flat region at large $\Delta\eta$ seen in the uncorrected gap fraction.

Numerical values for the inclusive cross section, the gap cross section and the corrected gap-fraction are provided in Tables 5.1, 5.2 and 5.3 respectively.

$\Delta\eta$	$d\sigma/d\Delta\eta$ (nb)	Statistical Uncertainty (nb)	Systematic Uncertainty (nb)
2.25	4.93	0.24	$^{+0.83}_{-0.68}$
2.75	3.06	0.15	$^{+0.54}_{-0.52}$
3.25	1.67	0.07	$^{+0.31}_{-0.19}$
3.75	0.51	0.03	$^{+0.08}_{-0.03}$

Table 5.1: $d\sigma/d\Delta\eta$ for $ep \to e\gamma p \to eX$ in the kinematic range $0.2 < y < 0.8$, $P^2 < 4$ GeV^2 and where X contains two or more jets of $E_T^{jet} > 6$ GeV, $\eta^{jet} < 2.5$, $|\bar{\eta}| < 0.75$ and $\Delta\eta > 2$.

$\Delta\eta$	$d\sigma^{gap}/d\Delta\eta$ (nb)	Statistical Uncertainty (nb)	Systematic Uncertainty (nb)
2.25	2.85	0.17	$^{+0.45}_{-0.45}$
2.75	0.66	0.06	$^{+0.11}_{-0.13}$
3.25	0.16	0.02	$^{+0.03}_{-0.04}$
3.75	0.06	0.01	$^{+0.01}_{-0.01}$

Table 5.2: $d\sigma^{gap}/d\Delta\eta$ for $ep \to e\gamma p \to eX$ in the kinematic range $0.2 < y < 0.8$, $P^2 < 4$ GeV^2 and where X contains two or more jets of $E_T^{jet} > 6$ GeV, $\eta^{jet} < 2.5$, $|\bar{\eta}| < 0.75$ and $\Delta\eta > 2$ with *no* final state particles of $E_T^{had\ cm} > 300$ MeV between the jets.

$\Delta\eta$	$f(\Delta\eta)$	Statistical Uncertainty	Systematic Uncertainty
2.23	0.58	0.01	$^{+0.01}_{-0.02}$
2.73	0.22	0.02	$^{+0.02}_{-0.02}$
3.22	0.10	0.01	$^{+0.01}_{-0.02}$
3.70	0.11	0.02	$^{+0.01}_{-0.02}$

Table 5.3: The gap-fraction, $f(\Delta\eta)$, for $ep \to e\gamma p \to eX$ in the kinematic range $0.2 < y < 0.8$, $P^2 < 4$ GeV^2 and where X contains two or more jets of $E_T^{jet} > 6$ GeV, $\eta^{jet} < 2.5$, $|\bar{\eta}| < 0.75$ and $\Delta\eta > 2$.

Chapter 6

Interpretation

To estimate the significance of the excess of the gap-fraction over the expectation from multiplicity fluctuations in non-singlet exchange, two methods have been used. The first, described in Sect. 6.1, relies on a comparison of the corrected data to model predictions. The second, described in Sect. 6.2, is based on the definition that the non-diffractive contribution to the gap-fraction is exponentially suppressed. This second method is independent of model predictions.

6.1 Comparison to Model Predictions

The corrected data are shown in Figure 6.1 as black dots where the inner error bars show the propagated statistical error of the data and Monte Carlo samples and the outer error bars show the additional systematic error. The PYTHIA non-singlet sample cross sections and gap-fraction are shown as open circles. The overall normalization of PYTHIA agrees with the data within the errors. PYTHIA also describes the shape of the inclusive cross section. However it fails to describe the gap cross section, falling too steeply with $\Delta\eta$ and disagreeing significantly in the last bin. PYTHIA does not reproduce the plateau observed in the measured gap-fraction. The difference between the data and the PYTHIA non-singlet gap-fractions in the last bin

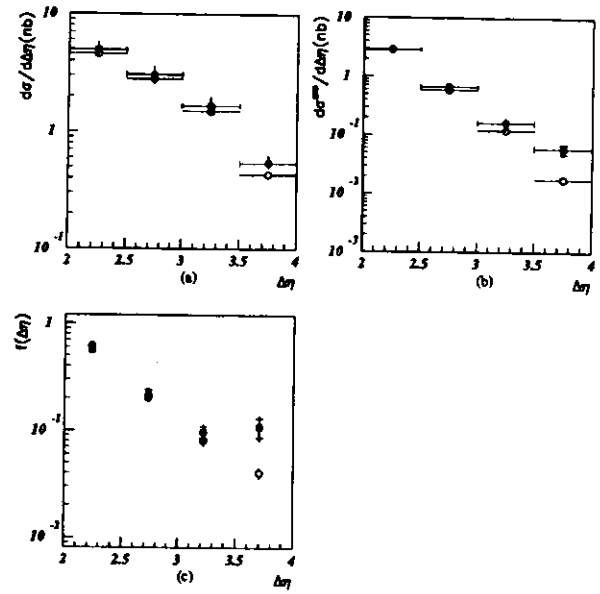

Figure 6.1: The data (corrected for detector effects) are shown as black dots where the inner error bar shows the statistical error and the outer error bar shows the systematic uncertainty added in quadrature. The predictions of the PYTHIA non-singlet sample for the hadron-level distributions are shown as open circles. The inclusive cross section is shown in (a). The gap cross section is shown in (b) and the gap-fraction is shown in (c).

is 0.07 ± 0.03. This may be interpreted as the excess in the gap-fraction over the expectation from multiplicity fluctuations in non-singlet exchange.

The excess determined in this way is inherently model-dependent. The predictions of several other PYTHIA models are shown in Figure 6.2. (The points are displayed at different $\Delta\eta$ values for clarity. The same binning is used in all cases.)

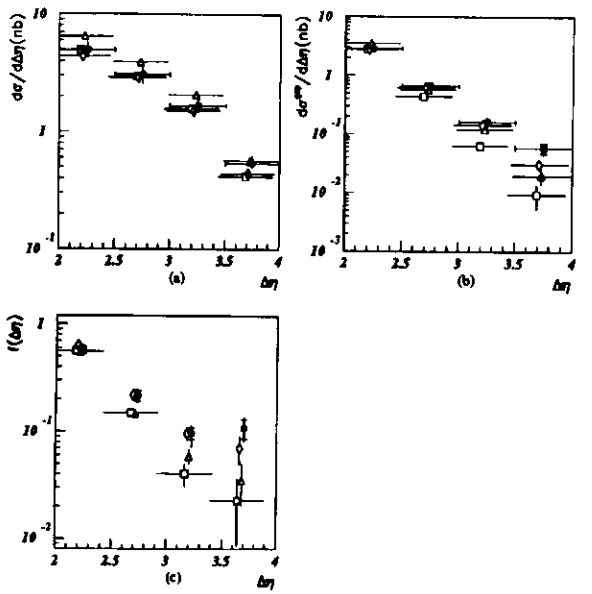

Figure 6.2: The data (corrected for detector effects) are shown as black dots where the inner error bar shows the statistical error and the outer error bar shows the systematic uncertainty added in quadrature. The PYTHIA predictions including multiple interactions are shown as triangles. The predictions using the Field-Feynman fragmentation function are shown as squares and the predictions from lowering σ_{p_T} are shown as diamonds.

The triangles in Figure 6.2 show PYTHIA non-singlet events with multiple interactions between the photon and proton simulated. The inclusive cross section is overestimated by this model although the gap cross section is of roughly the correct magnitude. The gap-fraction exhibits the behaviour that we expected. There are fewer gaps predicted when multiple interactions are simulated, than when they are not (mainly apparent in the two middle

$\Delta\eta$ bins). This model alone can not describe the data since it begins to underestimate the gap-fraction of the data already at $\Delta\eta \sim 2.5$. However we know that multiple interactions improve the description of the data in many distributions which are not differential in $\Delta\eta$ or multiplicity [71, 72]. Therefore some contribution from multiple interactions may be necessary in the model which is finally found to describe the data.

The squares in Figure 6.2 show PYTHIA non-singlet events with the Field-Feynman fragmentation function [79]. This fragmentation function produces even fewer gaps in the final state than the standard fragmentation function used in the PYTHIA simulations (the LUND symmetric fragmentation function [80]).

Diamonds show PYTHIA non-singlet events with the fragmentation parameter which sets the width of primary hadron p_T distribution with respect to the parent parton, σ_{p_T}, lowered from 0.36 to 0.25. The $\Delta\eta$ distributions from this model are similar to those of the non-singlet sample and of the data. In addition this model comes very close to describing the gap-fraction of the data. However this model has slightly narrower jet profiles than the non-singlet ones, and a lower jet pedestal. This is shown in Figure 6.3.

In Figure 6.3 the hadron-level jet profiles for the non-singlet sample are shown as the solid lines and for the low σ_{p_T} sample as the dashed lines. The profiles are shown on a log scale in order to highlight the difference between them. The discrepancy between these two models is best seen in the φ profiles. The low σ_{p_T} jets are somewhat more collimated than the standard jets and have a lower jet pedestal. We know that the standard jet profiles are already narrower than the data, and have a jet pedestal which is too low. Therefore we do not emphasize this model as the correct interpretation of our data.

HERWIG [81] is a Monte Carlo event generation program which uses a completely different fragmentation scheme from the LUND string model which is implemented in PYTHIA. The second analysis has obtained the

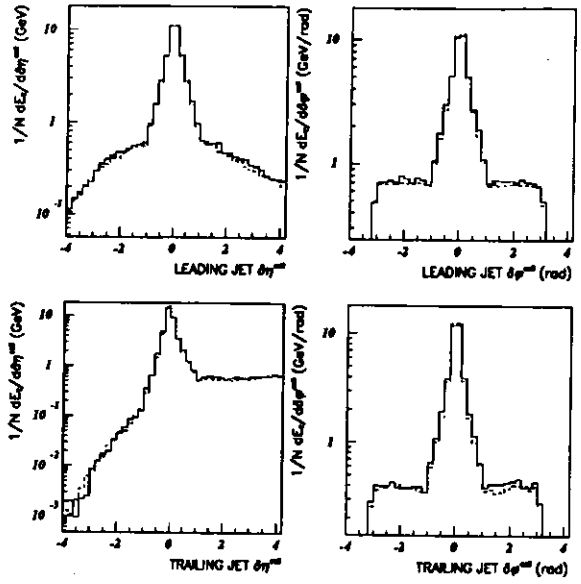

Figure 6.3: Hadron-level jet profiles are shown separately for the leading and trailing jets. The solid line shows the jet profiles of the non-singlet sample and the dashed line shows the jet profiles of the low σ_{p_T} sample.

cross sections and gap-fraction from the HERWIG simulation both with and without multiple interactions included. These predictions are compared with the data in Fig. 6.4. The data are shown as black dots. The HERWIG predictions including multiple interactions are shown as solid stars and the open crosses show the HERWIG predictions without including the simulation of multiple interactions. The cross sections have the correct shape but the overall normalization is too low. The HERWIG gap-fraction is consistent with the PYTHIA gap-fraction within the statistical errors. The HERWIG

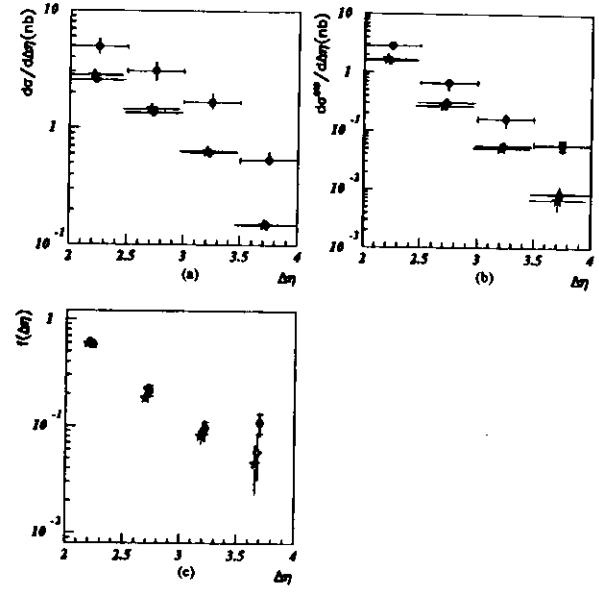

Figure 6.4: The data (corrected for detector effects) are shown as black dots where the inner error bar shows the statistical error and the outer error bar shows the systematic uncertainty added in quadrature. The HERWIG predictions including multiple interactions are shown as solid stars and the open crosses show the HERWIG predictions without multiple interactions.

simulation of multiple interactions shows the same effect as the PYTHIA simulation. The gap-fraction is lower at intermediate $\Delta\eta$ when multiple interactions are included.

6.2 Exponential Fit

Measuring the excess of the measured gap-fraction over the expected behaviour from non-singlet exchange by comparing the data to model predictions is clearly problematic as illustrated by the spread in the model predictions shown in the previous section. We wish to obtain a measure of the difference between the measured gap-fraction and the expected exponential behaviour using a model-independent method based on the data alone.

The corrected gap-fraction is redisplayed in Figure 6.5. The solid line shows the result of a χ^2 fit to,

$$f = C(\alpha,\beta)e^{\alpha\Delta\eta} + \beta \tag{6.1}$$

where $C(\alpha,\beta)$ constrains the fit to equal 1 at $\Delta\eta = 2$. The exponential and constant terms are shown as the dotted and dashed lines respectively. The fit is performed using the MINUIT program [82]. A χ^2 of 1.2 is obtained for

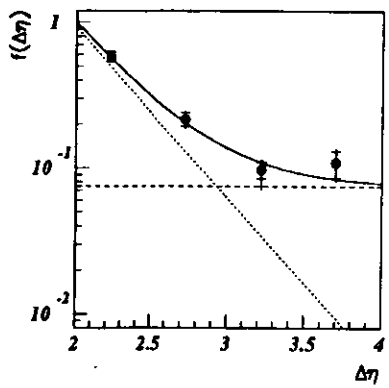

Figure 6.5: The gap-fraction, $f(\Delta\eta)$, with a fit to the expression, $f = C(\alpha,\beta)e^{\alpha\Delta\eta} + \beta$ shown as the solid line. The dotted line shows the exponential term and the dashed line shows the constant term.

the two degrees of freedom. This is superior to that of a fit to an exponential alone which yields $\chi^2 = 9$.

In order to obtain the statistical errors of the fit parameters the fit has been applied to the gap-fraction obtained using the central correction as described in Sect. 5.2.2 (including the statistical errors only.) The contour plot of the parameter deviations for this fit is shown in Figure 6.6. Contours for one through seven standard deviations of the parameters are shown. The solid lines intersect at the minimum of the χ^2 function and the dashed lines show the uncertainty of the parameters as determined by MINUIT. The fit

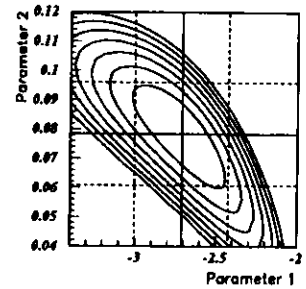

Figure 6.6: Contour plot of the χ^2 function showing the statistical errors of the central correction. The solid lines intersect at the minimum value of the χ^2 function and the dashed lines are one standard deviation from the fit parameter values.

parameters show a strong anticorrelation. This is easy to understand. To obtain a decent fit with a low plateau height one would need a shallow slope and conversely with a steep slope one would need a high plateau in order to fit the data. In any case the statistical errors of the fit parameters correspond to the extreme values of the one standard deviation contour. That is, they include the effect of the parameter correlation.

To estimate the systematic uncertainty of the fit parameters the χ^2 fit has then been performed separately for each of the sixteen systematic variations described in Sect. 5.2.2. The final fit parameters are the averages of these

seventeen results. Since the systematic deviations are consistent with being entirely due to statistical fluctuations the overall systematic uncertainty is simply taken from the largest deviation. The results are essentially equivalent if the systematic deviations are instead added in quadrature.

The results are,

$$\begin{aligned} \alpha &= -2.7 \pm 0.3(stat.) \pm 0.1(sys.) \\ \beta &= 0.07 \pm 0.02(stat.) \ {}^{+0.01}_{-0.02}(sys.). \end{aligned}$$

The parameter β corresponds to the excess of the measured gap-fraction over the gap-fraction from non-diffractive processes. As such, it estimates the fraction of colour singlet exchange processes in the data. This method uses the full information of the four measured data points and is not dependent on the details of the Monte Carlo fragmentation model.

6.3 Survival Probability

The excess in the gap-fraction over the expectation from non-singlet exchange may be interpreted as evidence for the exchange of a colour singlet object. In fact the fraction of events due to colour singlet exchange, $\hat{f}(\Delta\eta)$, may be even higher than the measured excess. As previously mentioned, secondary interactions of the photon and proton remnant jets could fill in the gap. A survival probability, $\mathcal{P}$, has been defined [35] which represents the probability that a secondary interaction does not occur. Then $f(\Delta\eta) = \hat{f}(\Delta\eta) \cdot \mathcal{P}$. Estimates of $\mathcal{P}$ for $p\bar{p}$ collisions at the Tevatron range from about 5% to 30% [35, 83, 84]. The survival probability at HERA could be considerably higher, due to the different colliding beam particles, the lower centre of mass energy, and in particular, due to the large fraction of the photon's momentum which participates in the hard interaction in these events.

x_γ^{OBS}, as defined in Sect. 1.3, is shown in Figure 6.7(a). The data are shown as black dots and the non-singlet and singlet PYTHIA samples as open circles and stars respectively. The data are peaked toward a very high

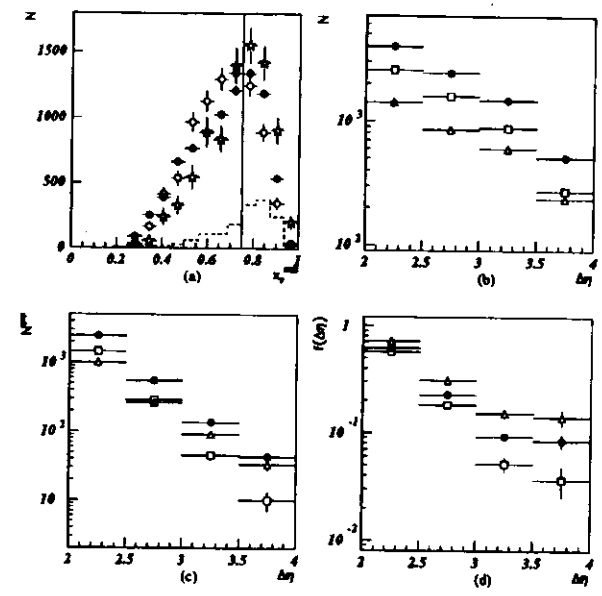

Figure 6.7: The dependence of the gap-fraction on x_γ^{OBS}. The distribution of x_γ^{OBS} is shown in (a). The data are shown as black dots. The PYTHIA sample containing no colour singlet exchange processes (the non-singlet sample) is shown as open circles. The subsample of the non-singlet sample which is due to LO direct processes is shown by the dashed line. The stars represent the PYTHIA sample which includes only colour singlet exchange processes (the singlet sample). The vertical line is drawn at $x_\gamma^{OBS} = 0.75$. The inclusive $\Delta\eta$ distribution, the $\Delta\eta$ distribution for gap events, and the gap-fraction are shown in (b), (c) and (d) respectively. (These distributions are uncorrected for detector effects and the errors shown are statistical only.) In (b), (c) and (d) only the measured data are shown (black dots). The triangles show the $x_\gamma^{OBS} \geq 0.75$ subsample and the squares show the $x_\gamma^{OBS} < 0.75$ subsample.

value, $x_\gamma^{OBS} \sim 0.8$, as compared to previous dijet studies. (See, for instance, Figure 1.5.) This is because the angular cuts $\Delta\eta > 2$, $\eta < 2.5$, and $|\bar{\eta}| < 0.75$ restrict to events which have either both jets in the central rapidity region,

or one jet in the rear rapidity region. Such configurations are rare unless a large fraction of the positron's energy participates in the hard interaction. Nevertheless the non-singlet sample is still largely composed of the LO resolved events. The dashed line in Figure 6.7(a) shows the contribution to the non-singlet sample from LO direct events.

The uncorrected $\Delta\eta$ distributions and the uncorrected gap-fraction are displayed in four bins in Figures 6.7(b), (c) and (d) (black dots) with statistical errors only. The data are then subdivided into two subsamples, $x_\gamma^{OBS} \geq 0.75$ events are shown as open triangles and $x_\gamma^{OBS} < 0.75$ as open squares. The $x_\gamma^{OBS} \geq 0.75$ subsample has the highest gap-fraction and the $x_\gamma^{OBS} < 0.75$ subsample has the lowest gap-fraction. This indicates that the survival probability does indeed increase with the parton momentum fraction. Therefore the ZEUS result of $0.07 \pm 0.02(stat.)^{+0.01}_{-0.02}(sys.)$ and the D0 and CDF results of $0.0107 \pm 0.0010(stat.)^{+0.0025}_{-0.0013}(sys.)$ and 0.0086 ± 0.0012 for the excess in the observable gap-fraction, $f(\Delta\eta)$, could all arise from the same excess in the underlying gap-fraction, $\hat{f}(\Delta\eta)$.

6.4 Summary and Conclusions

The results and their interpretation may be summarized as follows.

- The comparison of the uncorrected multiplicity distributions of the data with the multiplicity distributions of Monte Carlo samples which have been passed through a full detector simulation indicates that the data contain colour singlet exchange processes at a level of about 10%.

- The uncorrected gap-fraction exhibits the two component behaviour which is expected to indicate the presence of colour singlet exchange processes. This exponential fall at low $\Delta\eta$ and plateau at high $\Delta\eta$ can not arise as a detector effect on an original hadron-level exponential distribution.

- The gap-fraction corrected for detector effects confirms the two component behaviour of the uncorrected gap-fraction and allows for a quantitative evaluation of the height of the plateau, $0.11 \pm 0.02(stat.)^{+0.01}_{-0.02}(sys.)$.

- Two estimates of the excess of the gap-fraction over that expected from non-diffractive processes have been made. This excess may be interpreted as a lower limit on the fraction of events in the data due to colour singlet exchange.

  The first estimate of the excess is obtained from a comparison of the corrected data with the hadron-level prediction obtained from a Monte Carlo event generator. This method yields, 0.07 ± 0.03.

  The second estimate of the excess is obtained by fitting the data to the sum of an exponential and a constant gap-fraction. This method yields, $0.07 \pm 0.02(stat.)^{+0.01}_{-0.02}(sys.)$.

The magnitude of the squared four-momentum transfer across the rapidity gap as calculated from the jets is large ($|t| \geq (E_T^{jet})^2$). Thus the colour singlet exchange is unambiguously "hard".

The PYTHIA generator predicts that the ratio of the electroweak (σ^{EW}) to QCD (σ^{QCD}) exchange cross sections in this kinematic range is $\sigma^{EW}/\sigma^{QCD} < 7 \cdot 10^{-4}$ (compatible with the estimation $(\alpha/\alpha_s)^2$). Therefore quark quark scattering via γ/Z^0 and $W'^{\pm}$ exchange cannot explain the height of the flat region in the gap-fraction. On the other hand, using the simple two-gluon model for pomeron exchange gives $\hat{f}(\Delta\eta) \sim 0.1$ [35]. Thus pomeron exchange could account for the data.

In conclusion, dijet photoproduction events with $E_T^{jet} > 6$ GeV contain an excess of events with a rapidity gap between the two jets over the expectations of colour exchange processes. This excess is observed as a flat region in the gap-fraction at large rapidity separation ($\Delta\eta = 3.7$) at a level of $0.11 \pm 0.02(stat.)^{+0.01}_{-0.02}(sys.)$. It can be interpreted as evidence of hard diffractive scattering via a strongly interacting colour singlet object.

Appendix A

Kinematics

The kinematics of hard photoproduction at HERA are illustrated in this appendix using the hard diffractive scattering process as an example.

Fig. A.1(a) shows the diagram of a hard diffractive scattering process at HERA. The four vectors of the positron in the initial and final state are labelled by k and k' respectively. The invariant mass of the incoming photon is denoted with P^2 and the energy scale of the hard subprocess is denoted by Q^2. The momentum fractions of the partons which participate in the hard interaction are labelled with x_γ and x_p. In Fig. A.1(b) the centre of mass

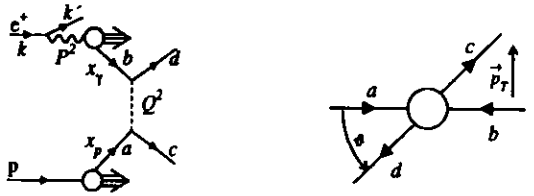

(a) (b)

Figure A.1: The hard diffractive scattering process. The full schematic diagram is shown in (a) and in (b) the centre-of-mass frame of the hard subprocess is shown.

view of the colliding partons is shown. The incoming partons are labelled a

and b and the outgoing partons are labelled c and d. The outgoing partons are scattered through an angle ϑ obtaining transverse momentum p_T with respect to the axis of the incoming partons.

A.1 Photon beam

The positron mass may be neglected. The positron momenta may then be written,

$$k = (E_e, 0, 0, -E_e) \quad (A.1)$$

$$k' = (E'_e, \vec{p}'_{Te}, E'_e \cos\vartheta'_e), \quad (A.2)$$

where E_e and E'_e are the energies of the incoming and outgoing positrons respectively and ϑ'_e is the angle of the outgoing positron with respect to the incoming proton direction. The photon invariant mass is then,

$$P^2 \equiv -(k - k')^2 \quad (A.3)$$

$$= 2k \cdot k' \quad (A.4)$$

$$= 2E_e E'_e (1 + \cos\vartheta'_e). \quad (A.5)$$

The antitag selection criteria described in Sect. 3.2 are very effective at rejecting DIS events with $P^2 > 1$ GeV^2. In fact the mean P^2 has been estimated to be 0.03 GeV^2 [26].

The dimensionless variable y is defined by,

$$y \equiv \frac{p_p \cdot p_\gamma}{p_p \cdot k}, \quad (A.6)$$

where p_p is the momentum of proton and p_γ is the γ momentum. This may be written,

$$y = \frac{E_p E_\gamma - \vec{p}_p \cdot \vec{p}_\gamma}{E_p E_e - \vec{p}_p \cdot \vec{p}_e}, \quad (A.7)$$

where E_p (E_γ) is the energy of the p (γ), and $\vec{p}_p$ ($\vec{p}_\gamma$) is the three-momentum of the p (γ). This reduces in the photoproduction regime, $P^2 \to 0$, and

neglecting the p mass, to

$$y = \frac{E_p E_\gamma (1 - \cos\vartheta_{p\gamma})}{E_p E_e (1 - \cos\vartheta_{pe})}, \tag{A.8}$$

where $\vartheta_{p\gamma}$ is the opening angle between the incoming p and γ and ϑ_{pe} is the opening angle between the incoming p and e^+. In the photoproduction regime the emitted γ is collinear with the incoming e^+. Therefore $\vartheta_{p\gamma} = \vartheta_{pe}$, and,

$$y = \frac{E_\gamma}{E_e}. \tag{A.9}$$

y may be estimated from the hadronic energy deposits in the calorimeter [62].

The γp centre-of-mass energy $W_{\gamma p}$ is clearly equal to $\sqrt{ys}$ where s is the e^+p centre-of-mass energy, 300 GeV. Thus $W_{\gamma p}$ may also be estimated from the hadronic energy deposits in the calorimeter. In this study, 131 GeV$< W_{\gamma p} <$ 277 GeV.

A.2 Parton momentum fractions

The momentum fractions x_p and x_γ are defined by

$$x_p \equiv \frac{p_\gamma \cdot a}{p_\gamma \cdot p_p} \tag{A.10}$$

$$x_\gamma \equiv \frac{p_p \cdot b}{p_p \cdot p_\gamma}. \tag{A.11}$$

In analogy with the reduction of y shown in Sect. A.1, the momentum fractions reduce to,

$$x_p \equiv E_a/E_p \tag{A.12}$$

$$x_\gamma \equiv E_b/E_\gamma, \tag{A.13}$$

where E_a and E_b are the energies of the partons from the p and γ side respectively.

The momentum fractions may be determined from the energies and angles of the outgoing partons according to,

$$x_p = \frac{\sum_{partons} E_T^{parton} e^{\eta^{parton}}}{2E_p} \tag{A.14}$$

$$x_\gamma = \frac{\sum_{partons} E_T^{parton} e^{-\eta^{parton}}}{2E_\gamma}. \tag{A.15}$$

These expressions may be understood by writing,

$$E_T^{parton} e^{-\eta^{parton}} = E_{parton} \sin\vartheta_{parton} \tan\frac{\vartheta_{parton}}{2} \tag{A.16}$$

$$= E_{parton} \sin\vartheta_{parton} \left(\frac{1 - \cos\vartheta_{parton}}{\sin\vartheta_{parton}}\right) \tag{A.17}$$

$$= E_{parton}(1 - \cos\vartheta_{parton}) \tag{A.18}$$

$$= E_{parton} - p_{z\,parton}, \tag{A.19}$$

and similarly,

$$E_T^{parton} e^{\eta^{parton}} = E_{parton} - p_{z\,parton}. \tag{A.20}$$

Then,

$$x_p = \frac{\sum_{partons} E^{parton} + p_z^{parton}}{2E_p} \tag{A.21}$$

$$x_\gamma = \frac{\sum_{partons} E^{parton} - p_z^{parton}}{2E_\gamma}. \tag{A.22}$$

However notice that (neglecting quark masses) $p_{za} = E_a$ and $p_{zb} = -E_b$. Therefore, invoking momentum conservation, equations A.21 and A.22 reduce to equations A.12 and A.13.

A.3 Energy scale

The energy scale of the hard subprocess, denoted Q^2, is equal to the magnitude of the invariant mass of the exchanged colour singlet object, as shown in Fig. A.1. This is the magnitude of the Mandelstam t variable defined by

$$t \equiv (a - c)^2. \tag{A.23}$$

t is a Lorentz invariant quantity. We determine it in the centre-of-mass frame of the hard subprocess wherein the parton momenta may be written,

$$a = (E,0,0,E) \quad (A.24)$$
$$b = (E,0,0,-E) \quad (A.25)$$
$$c = (E,\vec{p}_T,E\cos\vartheta) \quad (A.26)$$
$$d = (E,-\vec{p}_T,-E\cos\vartheta). \quad (A.27)$$

Then,

$$-t = \vec{p}_T{}^2 + E^2(1-\cos\vartheta)^2. \quad (A.28)$$

That is,

$$|t| \geq \vec{p}_T{}^2. \quad (A.29)$$

We use the final state jet transverse momenta in place of the parton transverse momenta in order to select a sample of hard scattering events. In this study, $(E_T^{jet})^2 \geq 36$ GeV^2.

Appendix B

Jet Finding

Because the quarks and gluons produced in a high energy interaction are confined, they can not be observed as free particles in the final state. However, thanks to local parton hadron duality (see Sect. 1.2) the distribution of the jets of hadrons which are produced in the hadronization process is similar to the distribution of the outgoing partons. Jet finding algorithms are used to cluster the hadrons into the objects which correspond to the outgoing partons. The additional criteria which must be satisfied by a jet finding algorithm are that the jets should be well defined experimentally, and also well defined theoretically to any order of perturbation theory. In 1990 at the Snowmass conference in Colorado a standard jet definition was proposed for hadron collisions involving the production of light quark and gluon jets [85].

B.1 The Snowmass Standard

According to the Snowmass recommendations a cone with centre $(\eta^{cone},\varphi^{cone})$ should be defined in (η,φ) space such that all hadrons with coordinates $(\eta^{hadron},\varphi^{hadron})$ within a radius $R \equiv \sqrt{(\eta^{cone}-\eta^{hadron})^2+(\varphi^{cone}-\varphi^{hadron})^2}$ $\leq R_0$ are included in the jet. The transverse energy of the jet, E_T^{jet} and the coordinates of the jet, $(\eta^{jet},\varphi^{jet})$ should then be determined from the hadrons

which lie inside the jet cone according to,

$$E_T^{jet} = \sum E_T^{hadron}, \tag{B.1}$$

$$\eta^{jet} = \frac{1}{E_T^{jet}} \sum \eta^{hadron} E_T^{hadron} \tag{B.2}$$

and

$$\varphi^{jet} = \frac{1}{E_T^{jet}} \sum \varphi^{hadron} E_T^{hadron}. \tag{B.3}$$

In addition it is recommended that the jet cone coordinates, $(\eta^{cone}, \varphi^{cone})$, be determined in an iterative fashion from initiating clusters. What is not specified by the Snowmass accord is how to obtain the initiating clusters, and how to deal with overlapping jet cones. For this reason a full description of the algorithm used to find jets in this analysis is provided in the following.

B.2 Main Jet Finding Algorithm

In this analysis, detector-level jets have been found by applying the jet finding algorithm to calorimeter cells (in the data and in the Monte Carlo samples). Hadron-level jets have been found by applying the jet finding algorithm to the final state hadrons in the Monte Carlo samples. The following description of the algorithm will refer to the hadron-level jets but the extension to detector-level jets is trivial.

A cone jet finding algorithm has been adopted with the cone size set to $R_0 = 1$. Other parameters used by the algorithm are the energy threshold of a seed cell or jet initiator, $E_{T0}^{seed} = 1.0$ GeV, and the energy threshold of a jet, $E_{T0}^{jet} = 6.0$ GeV (for the hadron-level case). The jet finding algorithm then proceeds via these steps.

Step 1 The final state hadrons are sorted into cells of approximate dimension 0.5×0.5 in (η, φ) space. (φ is measured in radians.)

Step 2 The transverse energy sum, E_T^{window}, is formed for each cell. E_T^{window} consists of the transverse energy contained in the associated cell plus the transverse energy contained in its eight surrounding neighbours (or its five surrounding neighbours if it is a cell at the edge of the acceptance in η).

Step 3 If a cell is found which has $E_T^{window} > E_{T0}^{seed}$ then it taken to be the initiator, or seed cell, of a jet. Thus η^{cone} and φ^{cone} correspond to the centre of this cell. (If no such cell is found then the event has no jets.)

Step 4 The transverse energy weighted centre of this jet is calculated according to formulae B.2 and B.3.

Step 5 The quantity ΔR^2 is formed, $\Delta R^2 = (\eta^{jet} - \eta^{cone})^2 + (\varphi^{jet} - \varphi^{cone})^2$.

Step 6 If $\Delta R^2 > 0.01\, R_0^2$ then the position of the jet centre is not considered to have converged and so the process is repeated by setting $\eta^{cone} = \eta^{jet}$ and $\varphi^{cone} = \varphi^{jet}$ and returning to Step 4. However if $\Delta R^2 \leq 0.01\, R_0^2$ then the position of the jet centre is considered to have converged.

Step 7 Steps 3 through 6 are repeated until a converged jet position has been searched for for all cells which have $E_T^{window} > E_{T0}^{seed}$. (The program will stop seeking convergence after a large number of iterations, or if the jet transverse energy calculated according to formula B.1 persists in being quite low with respect to E_{T0}^{jet}.)

Step 8 The converged jet of highest E_T^{jet} (according to formula B.1) is then saved, provided $E_T^{jet} \geq E_{T0}^{jet}$. The hadrons within the cone of this jet are removed from consideration and the jet finding program returns to Step 1 to find out if there are any jets associated with the remaining hadrons.

B.3 TLT Jet Finding Algorithm

We have also implemented a jet finding algorithm at the third level of triggering. In the environment of online data selection at ZEUS the execution speed of any algorithm must be made as high as possible. The TLT jet finding algorithm is therefore slightly less sophisticated. At the TLT, Step 3 is modified such that only the seed cell with the highest value of E_T^{window} is used as an initiator for a jet search. The jet position is still iterated in the same way, but once a suitable jet position is found for this seed the cells within the jet cone are immediately removed from consideration. The program returns to Step 1 to see if there are any more jet initiators (without first trying the other seed cells to see if they would yield a higher E_T^{jet} jet).

Appendix C

Three Jet events

The relative azimuth of the two highest E_T^{jet} jets is shown in Fig. C.1(a). The data are shown by the black dots. The non-singlet and singlet PYTHIA samples are shown by the open circles and the stars respectively. The data are strongly peaked toward a back to back configuration, however there is a tail to large values of relative azimuth which is not described by the non-singlet sample. Large values of $\Delta\varphi^{jet}$ occur in events where there are more than two jets in the final state. The singlet sample is even more strongly peaked toward $\Delta\varphi^{jet} = 180°$. This is consistent with the singlet sample having little energy deposited outside of the jets in general. A large decorrelation in $\Delta\varphi^{jet}$ has been suggested as a possible signature of higher order processes involving the hard emission of partons from the propagator [75, 76]. Thus we may expect that there are more events in the data with three or more jets, than are simulated in the Monte Carlo samples.

In Fig. C.1(b) one sees the subsample of events with $\Delta\eta > 3.5$. In these events the jets are more strongly peaked toward a back to back configuration and the description of $\Delta\varphi^{jet}$ by the Monte Carlo samples is better.

Fig. C.1(c) shows $\Delta\varphi^{jet}$ for the gap candidate events with $\Delta\eta > 3.5$. As these events can have very little energy outside of the jets it is not surprising that the events are very strongly peaked toward $\Delta\varphi^{jet} = 180°$ in all three samples.

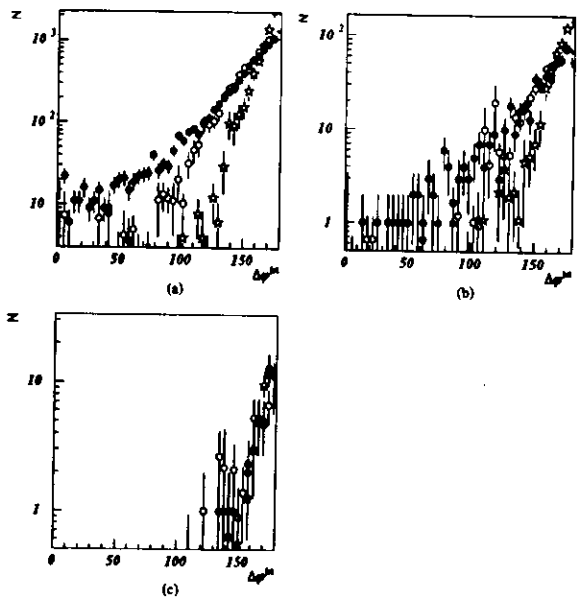

Figure C.1: Relative azimuth of the two highest E_T^{jet} jets for the inclusive sample is shown in (a). $\Delta\varphi^{jet}$ for the subsample with $\Delta\eta > 3.5$ is shown in (b) and (c) shows the gap candidate events with $\Delta\eta > 3.5$. The data are shown by the black dots. The open circles represent the PYTHIA sample which includes no colour singlet exchange processes (the non-singlet sample). The stars represent the PYTHIA sample which contains only electroweak quark quark scattering (the singlet sample).

In [37] a prediction for the gap-fraction is made at Tevatron energies. The calculational technique necessitates choosing the two jets at largest and least η^{jet} to evaluate the gap-fraction (rather than the two jets of highest E_T^{jet} which were used in this analysis). Clearly the results will only be different for the subsample of events which contains more than two jets. In Fig. C.2 the standard uncorrected $\Delta\eta$ distributions and the gap-fraction are shown as

black dots. The uncorrected $\Delta\eta$ distributions and the gap-fraction made by choosing the two jets at extreme η^{jet}, rather than the two highest E_T^{jet} jets, are shown for comparison as open circles.

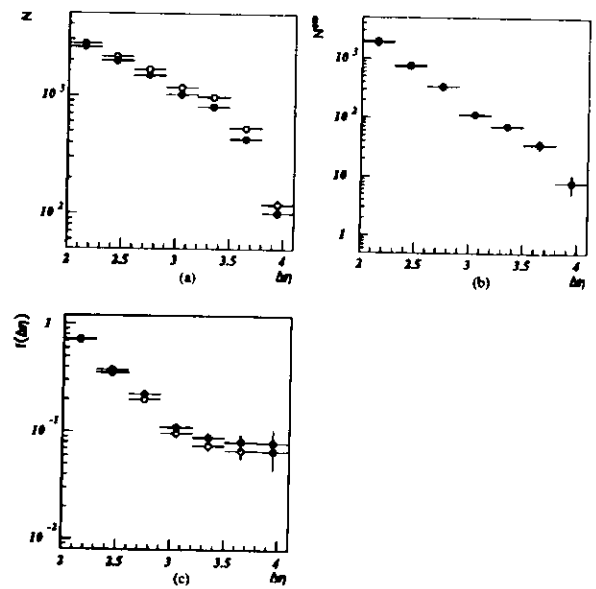

Figure C.2: The standard distributions calculated using the two jets of highest E_T^{jet} are shown as black dots. The inclusive $\Delta\eta$ distribution, the $\Delta\eta$ distribution for gap events and the gap-fraction are shown in (a), (b) and (c) respectively. The open circles show the corresponding distributions calculated using the jets at highest and lowest η^{jet} instead of the two highest E_T^{jet} jets.

Using the jets at highest and lowest η^{jet} will naturally yield more events overall since more events will satisfy the $\Delta\eta$ requirement of each $\Delta\eta$ bin. This effect is shown in Fig. C.2(a). However the N^{gap} distribution is almost identical for the two methods. This suggests that the gap events have exactly

two jets so that the two jets with highest E_T^{jet} are the same as the two jets at highest and lowest η^{jet}. As shown in Fig. C.2(c) the gap-fraction which results from using the jets ordered by η^{jet} is only about 1% lower than the standard gap-fraction. This result suggests that calculations such as those of [37] may be directly compared with the experimentally measured gap-fractions [10].

Appendix D

Bayesian Unfolding

We follow the notation and method of [77] with one addition. We define a generalized purity π_j which is analogous to the generalized efficiency ε_i. No discussion of the propagation of statistical errors in the unfolding procedure is provided here. A detailed discussion can be found in [77]. For this analysis the unfolding method was used as a systematic check. The statistical errors of the result are taken from the bin-by-bin correction method.

In the first subsection a short summary of the mathematical formalism is provided, and the unfolding algorithm is explained. In the second subsection the unfolding of the two cross sections $d\sigma/d\Delta\eta$ and $d\sigma^{gap}/d\Delta\eta$ is described.

D.1 Procedure

Let there be several independent causes C_i, $i = 1, 2, ..., n_C$, which can produce any one of several effects E_j, $j = 1, 2, ..., n_E$. Let $\mathcal{P}(C_i)$ be the initial probability distribution of the causes. We have,

$$\sum_{i=1}^{n_C} \mathcal{P}(C_i) = 1. \tag{D.1}$$

Let $\mathcal{P}(E_j|C_i)$ be the conditional probability of the i^{th} cause to produce the j^{th} effect. Then,

$$0 \leq \varepsilon_i \equiv \sum_{j=1}^{n_E} \mathcal{P}(E_j|C_i) \leq 1. \tag{D.2}$$

That is, there is no need for each cause to produce one of the effects taken into consideration. ε_i gives the efficiency of detecting the cause C_i in any of the known effects. Bayes theorem as implemented in [77] is then written,

$$\mathcal{P}(C_i|E_j) = \frac{\mathcal{P}(E_j|C_i) \cdot \mathcal{P}(C_i)}{\sum_{k=1}^{n_C} \mathcal{P}(E_j|C_k) \cdot \mathcal{P}(C_k)}. \tag{D.3}$$

In words, the probability of effect E_j having been due to cause C_i is proportional to the probability of the cause, times the probability of the cause to produce the effect. But note that in this way,

$$\sum_{i=1}^{n_C} \mathcal{P}(C_i|E_j) = 1. \tag{D.4}$$

That is, the background must be included among the causes. Instead we will allow for an unknown background distribution by defining a generalized purity π_j, thus,

$$0 \leq \pi_j \equiv \sum_{i=1}^{n_C} \mathcal{P}(C_i|E_j) \leq 1. \tag{D.5}$$

The generalized Bayes theorem then reads

$$\mathcal{P}(C_i|E_j) = \pi_j \cdot \frac{\mathcal{P}(E_j|C_i) \cdot \mathcal{P}(C_i)}{\sum_{k=1}^{n_C} \mathcal{P}(E_j|C_k) \cdot \mathcal{P}(C_k)}. \tag{D.6}$$

In words, the probability of effect E_j having been due to cause C_i is proportional to the probability of the cause, times the probability of the cause to produce the effect, times the probability that the effect is due to any of the considered causes C_i.

Fig. D.1 shows an example of the input to the unfolding procedure obtained, for instance, from a Monte Carlo study. The number of events per bin is shown by a box of proportional area. There are $n_E = 4$ measured

effects which can arise from one of $n_C = 4$ known causes. In addition, the $n_C + 1 = 5^{th}$ row represents the "unphysical" cause, or the background. The $n_E + 1 = 5^{th}$ column shows the inefficiency. These are events which can be attributed to one of the four causes but which give rise to no effect.

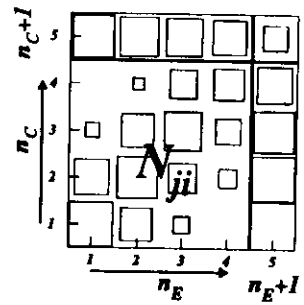

Figure D.1: Cause versus effect – Example of an unfolding problem.

The unfolding algorithm proceeds as follows:

1. Input the conditional probabilities $\mathcal{P}(E_j|C_i)$,

$$\mathcal{P}(E_j|C_i) = \frac{N_{ji}}{\sum_{k=1}^{n_E+1} N_{ki}}. \tag{D.7}$$

2. Input the generalized efficiencies ε_i,

$$\varepsilon_i = \frac{\sum_{j=1}^{n_E} N_{ji}}{\sum_{k=1}^{n_E+1} N_{jk}}. \tag{D.8}$$

3. Input the generalized purities π_j,

$$\pi_j = \frac{\sum_{i=1}^{n_C} N_{ji}}{\sum_{k=1}^{n_C+1} N_{jk}}. \tag{D.9}$$

These three inputs may come from a Monte Carlo study of the problem to be unfolded. They are not updated during the unfolding procedure.

Of course there will be a systematic uncertainty in the final solution associated with the uncertainty of the model used to obtain these input values.

1. Measure $n(E_j)$. This is the uncorrected distribution of the number of events associated with each effect.

5. Guess what the probability distribution of the causes, $\mathcal{P}(C_i)$, is. Of course, this is the quantity which we will determine through the unfolding procedure. However, a starting distribution must be input which could come from theoretical prejudice, or a flat initial probability distribution may be used.

6. Calculate the $\mathcal{P}(C_i|E_j)$ according to the generalized Bayes' theorem, equation D.6.

7. Calculate the corrected distribution of the number of events associated with each cause, $n(C_i)$ according to,

$$n(C_i) = \frac{1}{\varepsilon_i} \cdot \sum_{j=1}^{n_E} n(E_j) \cdot \mathcal{P}(C_i|E_j). \qquad \text{(D.10)}$$

8. If convergence of the distribution $n(C_i)$ has been achieved then iteration stops here. If not, then the probability distribution of the causes, $\mathcal{P}(C_i)$, is determined from $n(C_i)$, and steps 6 through 8 are repeated.

D.2 Application

For the case of the cross sections $d\sigma/d\Delta\eta$ and $d\sigma^{gap}/d\Delta\eta$ we wish to use the unfolding procedure to correct for detector effects, including migrations across the $\Delta\eta$ bins. Fig. D.2(a) shows the $\Delta\eta$ correlation for the inclusive events, as determined by the mixed Monte Carlo sample. (The areas of the boxes shown are actually proportional to the logarithms of the numbers of

events, since otherwise only the lowest $\Delta\eta$ bins would appear to be occupied.) Fig. D.2(b) shows the gap events.

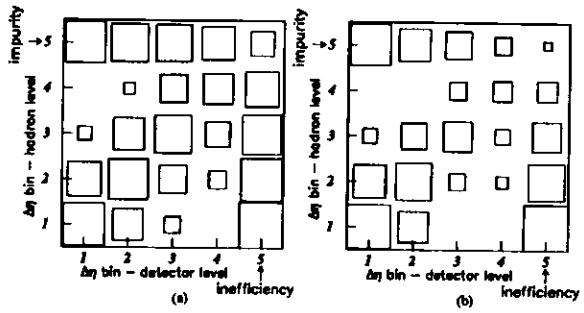

Figure D.2: Cause versus effect according to the mixed Monte Carlo sample. The correlation between the hadron-level and detector-level $\Delta\eta$ values is shown by the intersection of the first four rows and columns. The fifth column shows the hadron-level events which were not found as detector-level events. The fifth row shows the detector-level events which have not arisen from hadron-level events. The inclusive sample of events is shown in (a) and the subsample of events which are gap candidates is shown in (b).

We first apply the unfolding algorithm to the mixed Monte Carlo sample to check that convergence to the input hadron-level $\Delta\eta$ distributions is achieved. Fig.'s D.3(a) and (b) show the result for the inclusive and gap samples respectively.

The filled histogram shows the hadron-level $\Delta\eta$ distribution. The solid line shows the starting $n(C_i)$ distribution, chosen to be flat. (The Monte Carlo events are weighted according to cross-section therefore $n(C_i)$ here has units of nb.) The first, second and third iterations of $n(C_i)$ are shown as the dashed, dotted and dashed-dotted lines respectively. The procedure converges perfectly to the hadron-level distribution as shown by the solid dots. These show $n(C_i)$ after 31 iterations. (A short-coming of this procedure is that "convergence" is not clearly defined. One can evaluate a χ^2 function between successive iterations and stop the procedure once that falls below

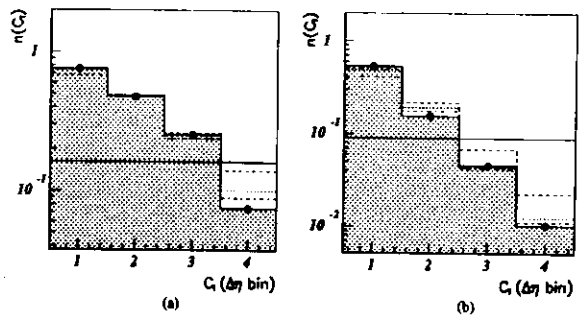

Figure D.3: Unfolding of the mixed Monte Carlo $\Delta\eta$ distributions using the mixed Monte Carlo sample inputs. The unfolding of the inclusive distribution is shown in (a) and (b) shows the unfolding of the distribution of the gap events. The filled histogram shows the hadron-level $\Delta\eta$ distributions. The solid line shows the starting distribution and the dashed, dotted and dashed-dotted lines show the first, second and third iterations of the unfolding procedure respectively. The final iteration of the unfolding procedure is represented by the black dots.

some cut-off value, but the cut-off value is arbitrary. We have found that for this particular measurement the $n(C_i)$ distributions are not changing significantly after 30 iterations so we stop there.)

The model dependence of the unfolding procedure has been checked by using the inputs from the mixed Monte Carlo sample to unfold the $\Delta\eta$ distributions of a pure resolved Monte Carlo sample. The results are shown in Fig.'s D.1(a) and (b) for the inclusive and gap events respectively.

Again, the solid line shows the starting $n(C_i)$ distribution and the dashed, dotted and dashed-dotted lines show the first, second and third iterations of $n(C_i)$ respectively and the black dots show $n(C_i)$ after the final iteration. The known hadron-level distributions are shown for comparison as open circles. The convergence is not perfect because the model is not a perfect description of the "data" (here the pure resolved sample). For example, the pure resolved sample contains more gluon jets in the final state than the mixed

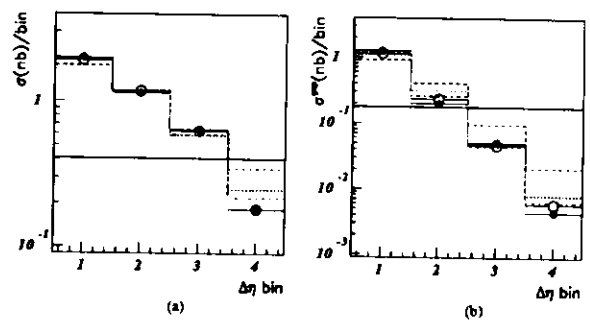

Figure D.1: Unfolding of the $\Delta\eta$ distributions of a pure resolved Monte Carlo sample using the mixed Monte Carlo sample inputs. The inclusive distribution is shown in (a) and the distribution of gap events is shown in (b). The solid line shows the starting distribution. The dashed, dotted and dashed-dotted lines show the first, second and third iterations respectively. The solid line shows the result of the final iteration. The open circles show the hadron-level distributions.

sample, which contains some direct photon events as well as some electroweak exchange events. These give rise to somewhat different (better) $\Delta\eta$ correlations than are given by the mixed sample. Nevertheless the procedure does converge to a result which is right within the statistical errors (about the size of the white dots).

Finally we show the result of the unfolding procedure applied to the data in Fig. D.5. The starting $n(C_i)$ distribution is shown by the solid line and the dashed, dotted and dashed-dotted lines show the first, second and third iterations of $n(C_i)$ respectively and the black dots show $n(C_i)$ after the final iteration, as previously. This time there is no hadron-level distribution to compare to the final $n(C_i)$ distribution. We have provided instead for comparison, the uncorrected distributions (the $n(E_j)$), as open circles.

The unfolding procedure yields corrected $\Delta\eta$ distributions which are not significantly different from the bin-by-bin corrected $\Delta\eta$ distributions. This can be seen in Fig.'s 5.14, 5.15 and 5.16. The difference is of the order of

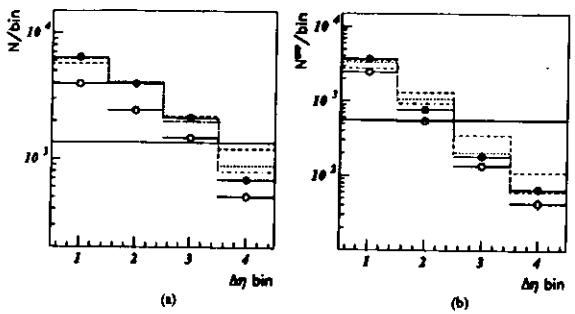

Figure D.5: Unfolding of the measured $\Delta\eta$ distributions of the data using the mixed Monte Carlo sample inputs. The starting distribution is represented by the solid line and the dashed, dotted and dashed dotted lines represent the first, second and third iterations respectively. The final iteration is shown by the black dots. The open circles show the uncorrected distributions.

the statistical error of the measurements, and does not constitute the largest systematic error in any bin of the measured distributions. The similarity between the two correction procedures increases our confidence that the detector effects are understood.

Appendix E

Glossary

Expression	Meaning	Page
BCAL	the barrel calorimeter	22
CTD	the central tracking detector	22
DESY	the Deutsches elektronen synchrotron	20
detector-level measurement (data)	a measurement which has not been corrected for detector effects	12
detector-level measurement (Monte Carlo sample)	a prediction made including the full detector simulation	12
diffractive hard process	a process leading to jets on only one side of a rapidity gap	12
diffractive process	a process leading to the formation of a rapidity gap	12
DIS	the class of e^+p collisions in which there is a large momentum transfer at the positron photon vertex	7

continued on next page

continued from previous page

Expression	Meaning	Page
FCAL	the forward calorimeter	22
FLT	the first level trigger	30
forward	in general refers to the p direction, or the direction of increasing rapidity	22
gap-fraction	the fraction of dijet events which contain a rapidity gap	17
hadron-level measurement (data)	a measurement which has been corrected for all detector effects	42
hadron-level measurement (Monte Carlo sample)	a prediction for the distribution of the final state hadrons	42
hard diffractive process	a process leading to jets on both sides of a rapidity gap	12
hard process	a process involving a large momentum transfer	6
HERA	the positron proton collider at DESY	20
island	a group of calorimeter cells which corresponds to one particle	37
leading jet (dijet events)	the jet at higher rapidity, or more forward jet	19
LO direct photoproduction	a photoproduction event in which all of the momentum of the γ contributes to the production of two hard partons in the final state	8

continued on next page

continued from previous page

Expression	Meaning	Page
LO resolved photoproduction	a photoproduction event in which a fraction of the momentum of the γ contributes to the production of two hard partons in the final state and the rest goes into a γ remnant jet	9
LUMI	the luminosity monitor	22
mixed sample	a sample of events generated by PYTHIA which contains a mixture of 90% standard hard photoproduction processes and 10% electroweak exchange processes	11
MOZART	the software program which simulates the ZEUS detector	12
non-singlet sample	a sample of events generated by PYTHIA which contains only standard QCD hard photoproduction processes	11
photoproduction	a class of e^+p events in which the scattered e^+ is essentially collinear with the incoming e^+	8
PYTHIA	a Monte Carlo event generator	11
QCD	quantum chromodynamics the theory of the strong interactions	2
rapidity gap	an interval of rapidity which contains no final state particles (possibly involving some energy threshold)	12

continued on next page

continued from previous page

Expression	Meaning	Page
RCAL	rear calorimeter	22
rear	in general refers to the e^+ direction, or the direction of decreasing rapidity	22
singlet sample	a sample of events generated by PYTHIA which contains only the LO resolved process of quark-quark scattering via γ/Z^0 or $W^{\pm}$ exchange	11
SLT	second level trigger	31
TLT	third level trigger	31
trailing jet (dijet events)	the jet at lower rapidity, or the jet more towards the rear	49
VXD	vertex detector	22

Table E.1: Glossary of commonly used expressions

Bibliography

[1] ZEUS Collab., M. Derrick et al., Phys. Rev. Lett. 75 (1995) 1006.

[2] ZEUS Collab., M. Derrick et al., DESY 95 182 (1995) to appear in Phys. Lett. B.

[3] Y. I. Azimov et al., Z. Phys. C27 (1985) 65.

[4] Y. L. Dokshitzer et al., Rev. Mod. Phys. 60 (1988) 373.

[5] V. N. Gribov and L. N. Lipatov, Sov. J. Nucl. Phys. 15 (1972) 438, 675.

[6] L. N. Lipatov, Sov. J. Nucl. Phys. 20 (1975) 94.

[7] G. Altarelli and G. Parisi, Nucl. Phys. B126 (1977) 298.

[8] ZEUS Collab., M. Derrick et al., Phys. Lett. B345 (1995) 576.

[9] NMC Collab., P. Amaudruz et al., Phys. Lett. B295 (1992) 159.

[10] NMC Collab., P. Amaudruz et al., CERN PPE/92 124 (1992).

[11] E. Witten, Nucl. Phys. B120 (1977) 289.

[12] J. F. Owens, Phys. Rev. D21 (1980) 54.

[13] T. Sjöstrand and M. van Zijl, Phys. Rev. D36 (1987) 2019.

[14] G. A. Schuler and T. Sjöstrand, Phys. Lett. B300 (1993) 169.

[15] G. A. Schuler and T. Sjöstrand, Nucl. Phys. B407 (1993) 539.

[16] J. M. Butterworth and J. R. Forshaw, J. Phys. G19 (1993) 1657.

[17] J. M. Butterworth et al., CERN TH 95 83 (1995).

[18] D. W. Duke and J. F. Owens, Phys. Rev. D30 (1984) 1447.

[19] H. Abramowicz et al., Phys. Lett. B269 (1991) 458.

[20] L. E. Gordon and J. K. Storrow, Z. Phys. C56 (1992) 307.

[21] M. Glück et al., Phys. Rev. D46 (1992) 1973.

[22] P. Aurenche et al., Z. Phys. C64 (1994) 621.

[23] M. Drees and R. M. Godbole, Phys. Rev. Lett. 61 (1988) 683.

[24] M. Drees and F. Halzen, Phys. Rev. Lett. 61 (1988) 275.

[25] M. Drees and R. M. Godbole, Phys. Rev. D39 (1989) 169.

[26] ZEUS Collab., M. Derrick et al., Phys. Lett. B348 (1995) 665.

[27] R. C. Feild, Ph.D. thesis, Pennsylvania State University (1995).

[28] J. D. Bjorken, in International Workshop on Deep Inelastic Scattering and Related Subjects, Eilat, Israel, ed. A. Levy (World Scientific, 1994) 151.

[29] ZEUS Collab., M. Derrick et al., Phys. Lett. B315 (1993) 481.

[30] ZEUS Collab., M. Derrick et al., DESY 95 093 (1995) to appear in Z. Phys.

[31] ZEUS Collab., M. Derrick et al., Phys. Lett. B356 (1995) 129.

[32] H1 Collab., I. Abt et al., Nucl. Phys. B429 (1994) 477.

[33] H1 Collab., I. Abt et al., Phys. Lett. B348 (1995) 681.

[34] Y. L. Dokshitzer et al., in Proceedings of the 6th International Conference on Physics in Collisions, Chicago, Illinois, ed. M. Derrick (World Scientific, 1987) 417.

[35] J. D. Bjorken, Phys. Rev. D47 (1992) 101.

[36] A. H. Mueller and W.-K. Tang, Phys. Lett. B284 (1992) 123.

[37] V. Del Duca and W.-K. Tang, Phys. Lett. B312 (1993) 225.

[38] H. J. Lu, AZPH TH/95 21 (1995).

[39] K. Goulianos, RU 95/E 06 (1995).

[40] V. Del Duca, DESY 95 116 (1995) Talk presented at the 10^{th} Topical Workshop on Proton Antiproton Collider Physics, Fermilab, Batavia, Illinois.

[41] A. H. Mueller and H. Navelet, Nucl. Phys. B282 (1987) 727.

[42] A. D. Martin, in International Workshop on Deep Inelastic Scattering and Related Subjects, Eilat, Israel, ed. A. Levy (World Scientific, 1994) 57.

[43] D0 Collab., S. Abachi et al., EPS 0505 (1995) Submitted to the International Europhysics Conference on High Energy Physics, Brussels, Belgium.

[44] H. N. Chehime and D. Zeppenfeld, MAD/PH/814 (1994).

[45] D0 Collab., S. Abachi et al., Phys. Rev. Lett. 72 (1994) 2332.

[46] D0 Collab., S. Abachi et al., FERMILAB PUB 95 302 E (1995).

[47] CDF Collab., F. Abe et al., Phys. Rev. Lett. 74 (1995) 885.

[48] J. Pumplin, Phys. Rev. D50 (1994) 6811.

[49] V. Barger et al., Phys. Lett. B346 (1995) 106.

[50] R. Brinkmann, DESY HERA 88 03 (1988).

[51] B. H. Wiik, in Physics at HERA, eds. W. Buchmüller and G. Ingelman (DESY, 1991) 1.

[52] G.-A. Voss and B. H. Wiik, Annu. Rev. Nucl. Part. Sci. 44 (1994) 413.

[53] ZEUS Collaboration, Status Report (1993).

[54] R. Wigmans, Annu. Rev. Nucl. Part. Sci. 41 (1991) 133.

[55] M. Derrick et al., Nucl. Inst. & Meth. A309 (1991) 77.

[56] A. Andersen et al., Nucl. Inst. & Meth. A309 (1991) 101.

[57] R. Yoshida, DESY 92 159 (1992) Talk presented at the III International Conference on Calorimetry in High Energy Physics, Corpus Christi.

[58] A. Bernstein et al., Nucl. Inst. & Meth. A336 (1993) 23.

[59] C. Alvisi et al., Nucl. Inst. & Meth. A305 (1991) 30.

[60] B. Foster et al., Nuc. Phys. B, Proc. Suppl. B32 (1993) 181.

[61] J. Andruszkow et al., DESY 92 066 (1992).

[62] F. Jacquet and A. Blondel, in Proceedings of the Study for an *ep* Facility for Europe, ed. U. Amaldi (DESY 79/48 1979) 377.

[63] ZEUS Collab., M. Derrick et al., Phys. Lett. B297 (1992) 404.

[64] L. L. Wai, Ph.D. thesis, Columbia University (1994).

[65] B. Andersson et al., Phys. Rev. 97 (1983) 31.

[66] G. Ingelman, DESY 88 014 (1987) Invited talk at the INFN workshop on Very High Energy Proton-Proton Physics, Erice, Italy.

[67] H.-U. Bengtsson and T. Sjöstrand, Comp. Phys. Comm. 46 (1987) 43.

[68] T. Sjöstrand, CERN TH.6488/92 (1992).

[69] A. Martin et al., Phys. Rev. D50 (1994) 6734.

[70] R. Brun et al., CERN DD/EE84 1 (1987).

[71] H1 Collab., I. Abt et al., Nucl. Phys. B445 (1995) 195.

[72] ZEUS Collab., M. Derrick et al., in Proceedings of the International Europhysics Conference on HEP, Brussels (1995).

[73] J. Pumplin, Nucl. Phys. B390 (1993) 379.

[74] ZEUS Collab., M. Derrick et al., Phys. Lett. B342 (1995) 417.

[75] V. Del Duca and C. R. Schmidt, Phys. Rev. D49 (1994) 4510.

[76] W. J. Stirling, Nucl. Phys. B423 (1994) 56.

[77] G. D'Agostini, Nucl. Inst. & Meth. A362 (1995) 487.

[78] M. Glück et al., Phys. Lett. B306 (1993) 391.

[79] R. D. Field and R. P. Feynman, Nucl. Phys. B136 (1978) 1.

[80] B. Andersson et al., Z. Phys. C20 (1983) 317.

[81] G. Marchesini et al., Comp. Phys. Comm. 67 (1992) 465.

[82] F. James and M. Roos, MINUIT Users Guide, Program Library Q100 (CERN 1991).

[83] E. Gotsman et al., Phys. Lett. B309 (1993) 199.

[84] R. S. Fletcher and T. Stelzer, Phys. Rev. D48 (1993) 5162.

[85] J. Huth et al., in Proceedings of the DPF 1990 Summer Study on High Energy Physics, Snowmass, Colorado, ed. E. L. Berger (World Scientific, 1992) 134.